# BRIDGING THE HIERARCHICAL STRUCTURES OF COLLAGEN BY ATOMIC FORCE MICROSCOPY: FROM NANOSCALE TO MESOSCALE

MING SUN
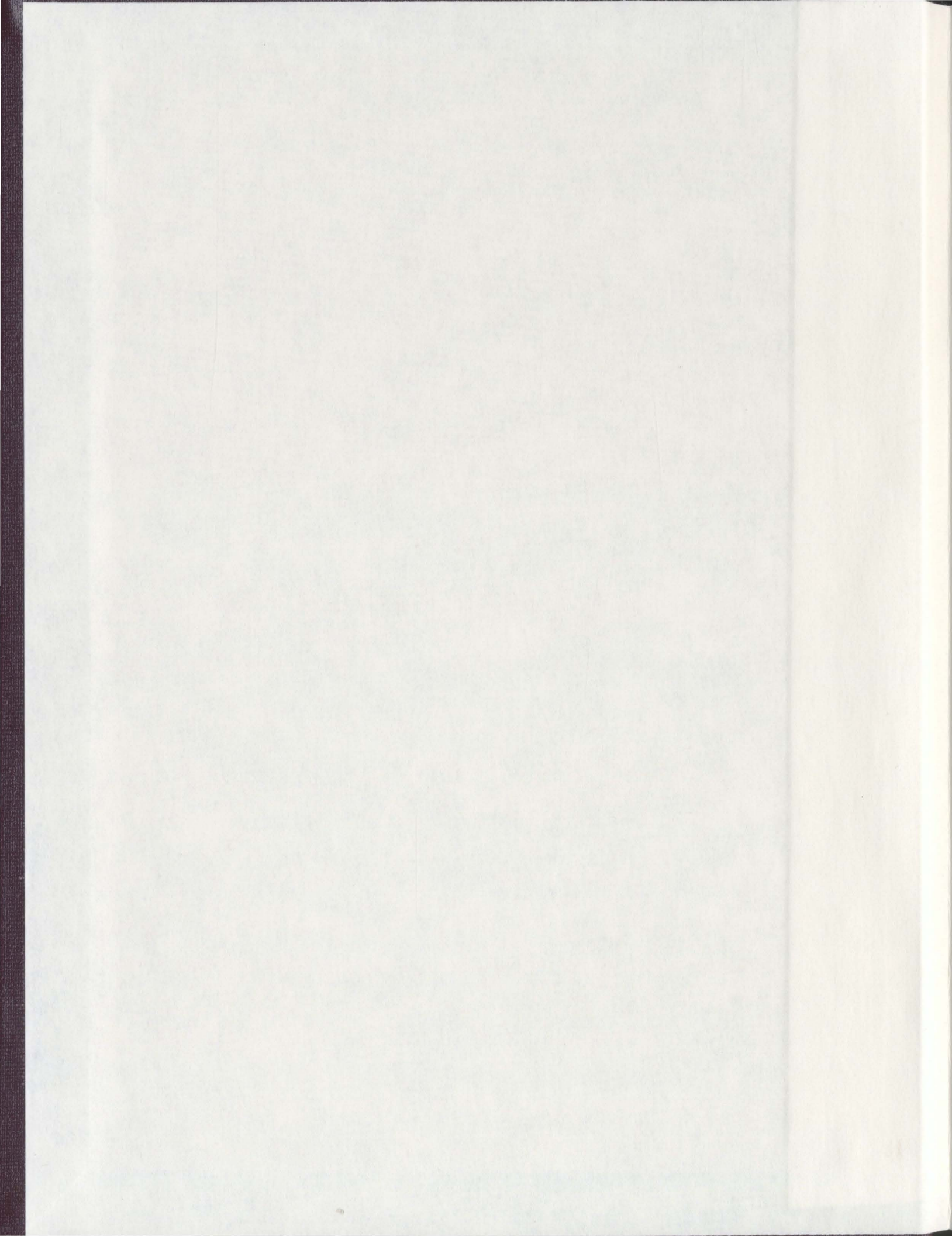
Bridging the hierarchical structures of collagen

by Atomic Force Microscopy:

from nanoscale to mesoscale

by

© Ming Sun

A thesis submitted to the School of Graduate Studies

in partial fulfilment of the requirements for the degree of

Master of Science

Department of Chemistry

Memorial University of Newfoundland

December, 2006

St. John's   Newfoundland

Table of Contents

ii

Abstract

The most abundant structural protein in mammalian tissues, Type I Collagen monomer, a long rope of 300 nm in length and 1.5 nm in diameter, can self-assemble into different three-dimensional structures with multiple functions as diverse as transparent cornea, tough tendon, and strong bone. Although the microscopic structure of the monomer and the macroscopic structures of some higher hierarchical assembled fibrils have been characterized during the past years, the formation of these higher hierarchical structures, and the emergence of their bioactivities on the nano-to-mesoscale, are still not so clear. In our work, AFM (atomic force microscopy) was applied *in vitro*, primarily as a imaging tool to investigate the self-assembled protofibril patterns (bottom-up method), and also as a 'molecular broom' to create monomer bundle patterns under appropriate force (top-down method). We believe those unique discoveries in our lab will definitely cast light on the understanding of the *in vivo* self-assembly and related structure-property relationships of collagen, and provide a functional surface coating method for tissue engineering and cell study.

Acknowledgments

First of all, I would like to thank my supervisor Dr. Erika Merschrod for her patient guidance over two and a half years. It was really a pleasure to work in such a free environment provided by Dr. Erika Merschrod. I really appreciate her timely help in my work and in my life.

I would also like to give my thanks to my lab fellows in the Merschrod group, and faculty and staff who have instructed me and helped me at Memorial.

I also want to thank all my friends in St. John's. I was really impressed by the beauty of this place and the kindness of the people here.

Finally, I want to thank my family for their unwavering support. Especially, I want to thank my wife for everything. Also my wife and I know that both our parents are always there for us although we are already independent, which will keep our hearts warm for ever.

List of Tables

List of Figures

Chapter 1
Introduction of collagen and Atomic Force Microscopy

1.1 *Collagen*

Collagens are the major constituents of the connective tissues of multicellular animals.[1-5] As the most important extracellular matrix (ECM) proteins found in a wide range of vertebrates and invertebrates, collagen fibrils act as both solid state regulators for cellular function and scaffolding of the tissue architecture, particularly in large vertebrates.[1-13]

Collagens are mostly synthesized by fibroblasts in the cell and then are secreted into the extracellular matrix (ECM) as procollagens, which are the precursors of tropocollagens. As shown in Fig.1.1, procollagens are synthesized as three polypeptide chains wound into a triple helical section in the middle and are converted into tropocollagens by the removal of the *N*-propeptides and *C*-propeptides by procollagen *N*-proteinase and procollagen *C*-proteinase respectively in the extracellular environment. It is assumed that the *C*-propeptides and *N*-propeptides on the ends of procollagen play an important role to regulate the formation of the triple helix in the cell. The obtained tropocollagens, which are also called collagen monomers, the molecular units of collagen fibrils, are probably the longest protein molecules known so far. Tropocollagen consists of three polypeptide chains coiled around each other and thus forms a triple helix throughout most of the rope-like structure. There are more than 20 types of different collagens in animal tissues, and most of the tropocollagens are long ropes of a diameter

1
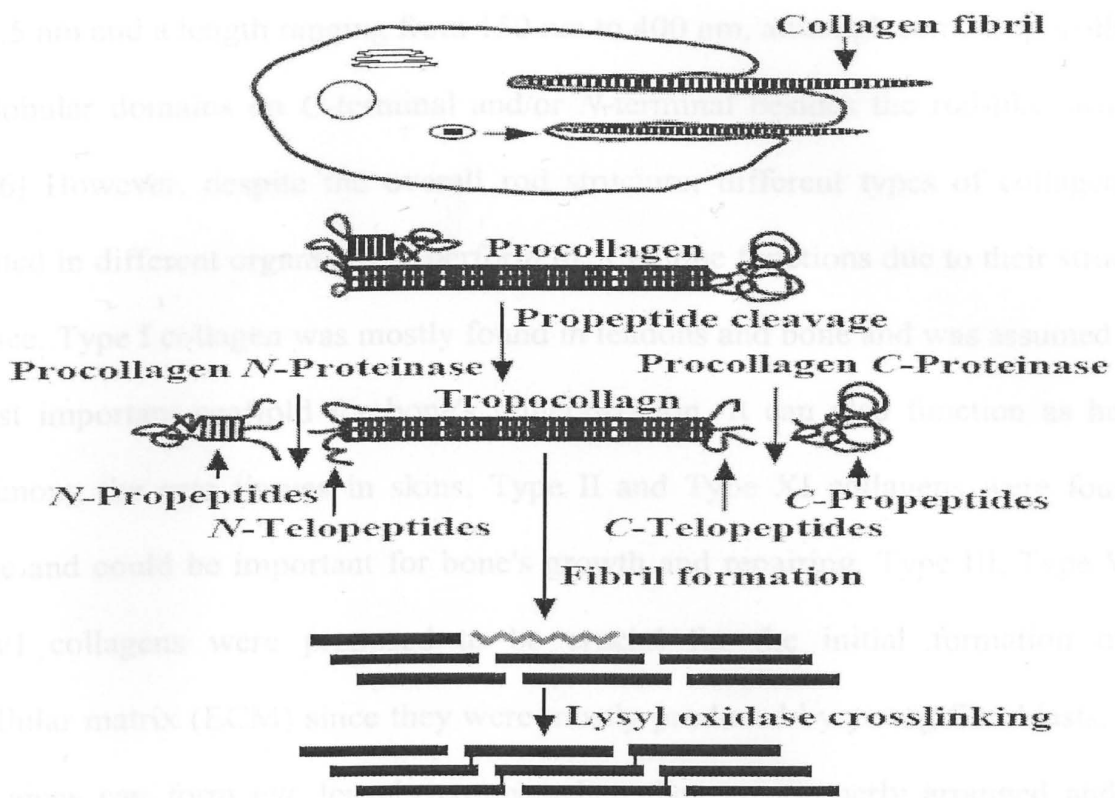
Figure 1.1   Extracellular events in the synthesis of fibrillar collagens. Procollagen consists of a 300 nm triple helix domain flanked by a trimeric globular C-propeptide domain (the right hand side of the diagram) and a trimeric N-propeptide domain (the left hand side of the diagram). Procollagen is secreted from cells and is converted into collagen by the removal of the N- and C-propeptides by procollagen N-proteinase and procollagen C-proteinase respectively. Collagen monomers generated in the reaction spontaneously self-assemble into D-banded fibrils that occur in the extracellular matrix of connective tissues. The fibrils are stabilized by covalent crosslinking that is initiated by oxidative deamination of specific lysine and hydroxylysine residues in collagen by lysyl oxidase.[1]

2

about 1.5 nm and a length ranging from 150 nm to 400 nm, although some tropocollagens have globular domains on *C*-terminal and/or *N*-terminal besides the rod-like structure. [1,14-26] However, despite the overall rod structure, different types of collagens are distributed in different organisms to perform their unique functions due to their structural difference. Type I collagen was mostly found in tendons and bone and was assumed to be the most important scaffold for bone's mineralization. It can also function as healing agent among the scar tissues in skins. Type II and Type XI collagens were found in cartilage and could be important for bone's growth and repairing. Type III, Type V and Type VI collagens were proposed to be crucial for the initial formation of the extracellular matrix (ECM) since they were mostly produced by young fibroblasts. Type IV collagens can form eye lens in cornea when they are properly arranged and thus achieve high optical transparency. Type X collagen was also assumed to be crucial for bone's formation by mineralizing cartilage.[13-26]

Among all of the collagens, Type I collagen is distinguished by its abundance in mammalian organisms.[27-31] Also, Type I Collagen is among several types of collagens that can self-assemble into fibrils of the 67 nm characteristic axial periodicity, or *D*-banding. As mentioned above, Type I procollagen is synthesized as three polypeptide chains in the cell, and each chain consists of around 1500 amino acid residues and is of a mass around 140 kDal. The three polypeptide chains are two identical $\alpha_1(I)$ chains and one $\alpha_2(I)$ chain. The $\alpha_1(I)$ and $\alpha_2(I)$ chains are very similar, but their primary structures are coded by separate genes. On the ends of one polypeptide chain of Type I procollagen, the *N*-propeptide of 150 amino residues and *C*-propeptide of 250 amino acid residues are of a

total mass around 45 kDal. The three *C*-propeptides and the three *N*-propeptides all adopt a globular conformation and are stabilized by intrachain and interchain disulfide bonds. It is assumed that the globular *C*-propeptides and *N*-propeptides play an important role in regulating the formation of the triple helical section. After the removal of the *N*-propeptides and *C*-propeptides in the extracellular matrix (ECM), the obtained Type I tropocollagen is a long rope of 300 nm in length and 1.5 nm in diameter, consists of three polypeptide chains coiled around each other, and thus forms a triple helix throughout 95% of its length. As a matter of fact, each polypeptide chain of Type I tropocollagen still has a molecular weight of approximately 95 kDal and a little more than 1000 amino acid residues. The three polypeptide chains by themselves are in a left-handed helical conformation, and wind around each other into a right-handed super triple helix with a periodic supercoil pitch around 8 nm.[1,14-32]

Like most proteins, the triple helix of Type I tropocollagen is stabilized by interchain hydrogen bonds and entropic forces under physiological conditions. Hydrogen donors in most of the hydrogen bonds are NH groups from glycine residues and hydrogen acceptors are the carboxyl groups from other residues on different chains.[14] In every single chain of the unique helical structure of Type I collagen, every three amino acid residues must be a glycine to adapt the final triple-helical structure.[1,14-32] As the smallest amino acid, glycine, is quite conserved in all collagen helices because other amino acid residues are too big to be accommodated, which is also the truth in the cytochrome *c* family.[33-35] Other than glycine, other abundantly existing residues are most likely to be *4*-hydroxyproline and *5*-hydroxylysine. It was reported that those

4

$$\text{prolyl residue} + O_2 + {}^-OOC\text{—}CH_2\text{—}CH_2\text{—}C(=O)\text{—}COO^- \;(\text{2-oxo glutarate})$$

prolyl residue   **2-oxo glutarate**
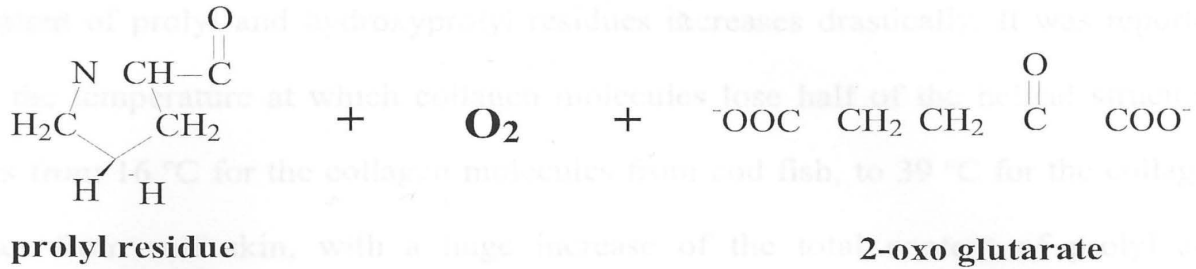
$$\xrightarrow[\text{vitamin C}]{\text{prolyl hydroxylase}}$$

$$\text{4-hydroxyprolyl residue} + CO_2 + {}^-OOC\text{—}CH_2\text{—}CH_2\text{—}COO^-$$

4-hydroxyprolyl residue   **succinic acid**
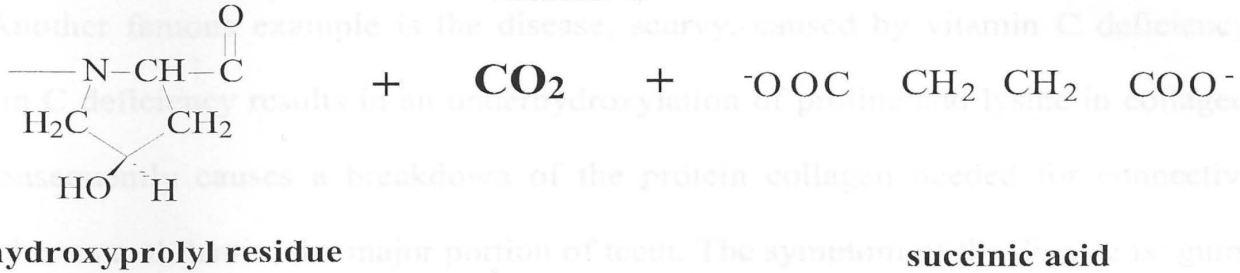
Figure 1.2   The mechanism of hydroxylation of prolyl residue into *4-hydroxyprolyl* by O_2, *2*-oxo glutarate catalyzed by prolyl hydroxylase with vitamin *C* as cofactor.[14,15,26]

hydroxy proteins can not be assimilated from outer environment, and that hydroxylation of the appropriate prolyl and lysyl residues to *4*-hydroxyprolyl, *3*-hydroxyprolyl, and *5*-hydroxylysyl residues is a modification required inside the cell to ensure proper folding and assembly of procollagen.[15,26] Many experiments proved that hydroxylation of the appropriate prolyl residues are especially important to stabilize the helical structure by extra hydrogen bonds between prolyl residues and hydroxyprolyl residues.[36,37] Fig.1.2 shows the hydroxylation process of prolyl residues by O_2, 2-oxo glutarate, which is catalyzed by prolyl hydroxylase with vitamin C, also called ascorbic acid, as a cofactor. During the evolution process from cold-blooded animals to warm-blooded animals, the

5

total content of prolyl and hydroxyprolyl residues increases drastically. It was reported that T_m, the temperature at which collagen molecules lose half of the helical structure, increases from 16 °C for the collagen molecules from cod fish, to 39 °C for the collagen molecules from calf skin, with a huge increase of the total content of prolyl and hydroxyprolyl residues from 155 residues/1000 residues to 232 residues/1000 residues. [38] Another famous example is the disease, scurvy, caused by vitamin C deficiency. Vitamin C deficiency results in an underhydroxylation of proline and lysine in collagen, and consequently causes a breakdown of the protein collagen needed for connective tissue, bones and dentin, the major portion of teeth. The symptom of the disease is: gums deteriorate and bleed, with loss of teeth; skin discolors; and wounds do not heal. This was notorious in the British Royal Navy, where sailors were deprived of fresh fruits and vegetables during long voyages. However, this disease can be effectively prevented by taking green vegetables or citrus fruit juices.[36] Other than the interchain hydrogen bonds among the collagen molecules, the tropocollagen helix is also stabilized by the entropy force (the spatial repulsion) of the pyrrole rings on prolyl and hydroxyprolyl residues.[14]

We discussed a lot about the main part, the triple helix, on Type I tropocollagen above. However, the 17 N-terminal residues and the 26 C-terminal residues (see Fig.1.1), which are called telopeptides and are assumed to provide self-assembly information into fibrils of 67 nm axial periodicity (D-period), do not have glycine as every third residue. [1,32,39-42] From electron micrograph analysis of fibrils reconstituted *in vitro* from tendon and skin Type I collagen, a model of the axial packing arrangement of triple-

6

H—N

H   C   (CH₂)₃   CH₂   NH₃⁺   ⁺H₃N—CH₂—(CH₂)₃—C—H

O   C   C=O

lysyl oxidase

H   N   O   O   N   H

H—C—(CH₂)₃—C   C   (CH₂)₃   C   H

O=C   H   H   C   O

aldol condensation

H   N   OH   N   H

H   C   (CH₂)₃   CH   CH   (CH₂)₂   C   H

O=C   C   C—O

O   H

histidine residue   *lysyl residue*

H   O

—HN—C—C—

CH₂

C   N

HC   CH

H   N   N   N   H

H—C—(CH₂)₃—CH—CH—(CH₂)₂—C—H

O=C   C   C   O

O   H

H—N   OH   N—H

H—C—(CH₂)₃—CH—CH—(CH₂)₂—C—H

O   C   C   C=O

N

(CH₂)₄

N   C   C

H   H   O
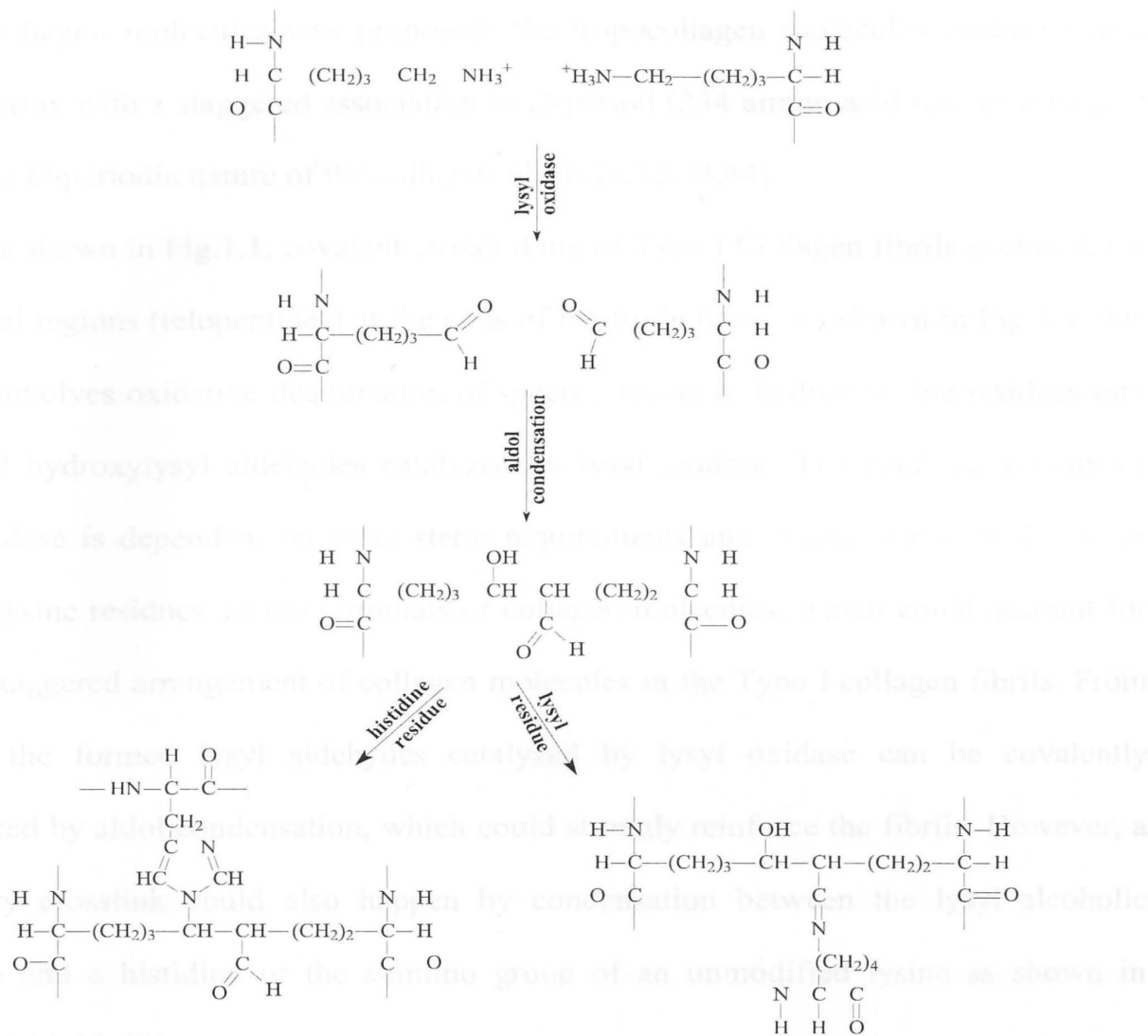
Figure 1.3   Mechanism of covalent crosslinking of Type I Collagen fibrils. This process involves oxidative deamination of lysyl residues into lysyl aldehydes catalyzed by lysyl oxidase. The formed lysyl aldehydes can be covalently crosslinked through aldol condensation, which could strongly reinforce the fibrils. A secondary crosslink could also happen by condensation between the lysyl alcoholic aldehyde and a histidine or the ε-amino group of an unmodified lysine.[14,45-49]

helical collagen molecules was proposed: the tropocollagen molecules assemble in a parallel array with a staggered association of D-period (234 amino acid residues) to give rise to the D-periodic nature of the collagen fibrils.[1,32,43,44]

As shown in Fig.1.1, covalent crosslinking of Type I Collagen fibrils occurs in the nonhelical regions (telopeptides) at the ends of the triple helix. As shown in Fig.1.3, this process involves oxidative deamination of specific lysine or hydroxylysine residues into lysyl and hydroxylysyl aldehydes catalyzed by lysyl oxidase. The catalytic activity of lysyl oxidase is dependent on strict steric requirements and usually modifies lysine or hydroxylysine residues on the terminals of collagen molecules, which could account for the the staggered arrangement of collagen molecules in the Type I collagen fibrils. From Fig.1.3, the formed lysyl aldehydes catalyzed by lysyl oxidase can be covalently crosslinked by aldol condensation, which could strongly reinforce the fibrils. However, a secondary crosslink could also happen by condensation between the lysyl alcoholic aldehyde and a histidine or the ε-amino group of an unmodified lysine as shown in Fig.1.3.[1,14,45-49]

Besides their abundance in animals' bodies, collagens are unique because they are multifunctional proteins. The size, shape, and arrangement of the fibrils are important to determine tissues' functions. The hierarchical structures of many different types of collagen fibrils have been studied for many years to illustrate the relationship between their inherent spatial arrangement and the mechanical and physical properties of related tissues. For instance, in the optically transparent cornea narrow fibrils around 20 nm in width are precisely arranged in orthogonal arrays, whereas in mature tendon of high

8

tensile strength, large fibrils around 500 nm in diameter are arranged in parallel bundles of a high density around 10^8 fibrils/mm^3 and such fibrils are also stabilized by the covalent crosslinking discussed above.[1,40,50,51] More examples about hierarchical arrangement of collagen fibrils came from the biomineralization in animals' bones and dentins. During the biomineralization process, parallel collagen fibril bundles of a high density are assumed to provide potential scaffolds for mineralization. It was reported that hydroxyapatite $\{Ca_{10}(PO_4)_6(OH)_2\}$ is first nucleated in specific sites of the *D*-banding fibrils, and then grows into mineral platelets within the collagen fibrils in a highly organized staggered manner.[52,53] Lots of experiments have been done to characterize the structures of tissues like tendons, bones of high hierarchy, and also to investigate the mechanisms to form those structures.[54-59]

As we discussed before, the microscopic structure of the many types of collagen monomers have been characterized by different methods, and even the genes to express those proteins have also been discovered one by one.[14-26,38,60-66] And nowadays, scientists also know a lot about the fine structures of the connective tissues such as tendons, bones, and dentins, with the progress in analytical instruments.[50,54-59,67-71] However, in the extracellular environment, how collagen monomers at a nanoscale self-assemble into higher hierarchical structures, like protofibrils, at a mesoscale, with the emergence of new bioactivities is still not so clear. Many experiments have been focused on the collagen fibrils reconstituted *in vitro* to illustrate the truth underneath the fine construction accomplished by nature *in vivo*. Based on all of those inspirations from the reconstitution experiments *in vitro*, we joined this procession and tried to dig things

9

deeper. We hope that our work will not bring more controversies to this already confusing area, but definitely cast some light on the understanding of the *in vivo* self-assembly and related structure-property relationships of collagen and provide potential applications.

1.2 *Atomic Force Microscopy (AFM)*

Scanning probe microscopes (SPM), representing the most advanced analytical instruments invented so far, since first developed by G. Binnig and coworkers in 1982 at IBM in Zurich, have been widely applied to image and manipulate materials at nanoscales.[72-83] In general, SPM images are obtained by scanning a sharp probe across a surface while monitoring and compiling the tip-sample interactions to provide an image. The three primary members of the SPM family are STM (Scanning Tunneling Microscopy), AFM (Atomic Force Microscopy), and SNOM (Scanning Near-Field Optical Microscopy).[72-74] Although scanning tunneling microscopy (STM) can image and measure material surface morphology with atomic resolution and can even manipulate single atoms, the application of STM absolutely depends on tunneling current between the STM tip and the sample and thus only good electrical conductors can be good samples for imaging.[72] However, as the most important member of the SPM family, atomic force microscopy (AFM), since first invented by G. Binnig, C. F. Quate, and Ch. Gerber in 1986, has been applied in much wider area compared to STM because AFM is also able to image atomic scale features on insulating surfaces including biological samples under physiological conditions.[74-77,80,81]

10

A simplified work mechanism of AFM is shown in Fig.1.4. The vertical direction is defined by the z-axis and the lateral plane is defined by the x axis and the y axis as shown. During an AFM imaging process, a small sharp tip of a radius of curvature less than 10 nm and a height around 15 μm is attached to one end of a cantilever of a length of around 200 μm. When the tip is brought into close proximity with a sample surface, the forces acting between the AFM tip and the sample will result in a bend of the cantilever. A laser beam is focused on the back of the cantilever and reflects into a four-quadrant photodetector. Vertical forces deflect the cantilever up or down, lateral forces twist the cantilever left and right. The vertical bend and the lateral twist of the cantilever are simultaneously and independently measured by monitoring the deflection of the reflected laser beam.

During the imaging process, the interaction between the AFM tip and the sample is always maintained constant by bringing the cantilever up or down while the tip is scanning the sample's surface line by line. The vertical position of the cantilever can be located and controlled by a z-axis piezoelectric actuator and the lateral position of the tip is on can also be located by a lateral controller that is usually also made of two piezoelectric actuators. Atomic and even sub-atomic accuracy in positioning is obtained if piezoelectric actuators are employed. Utilizing the inverse piezoelectric effect, a driving voltage applied to the electrodes of the piezoelectric actuator can be converted directly into elongations and contractions of the actuator. With a suitable arrangement of the piezoelectric actuators with the AFM sample and the AFM cantilever, a three dimensional position of the AFM cantilever can be achieved. During the imaging

11
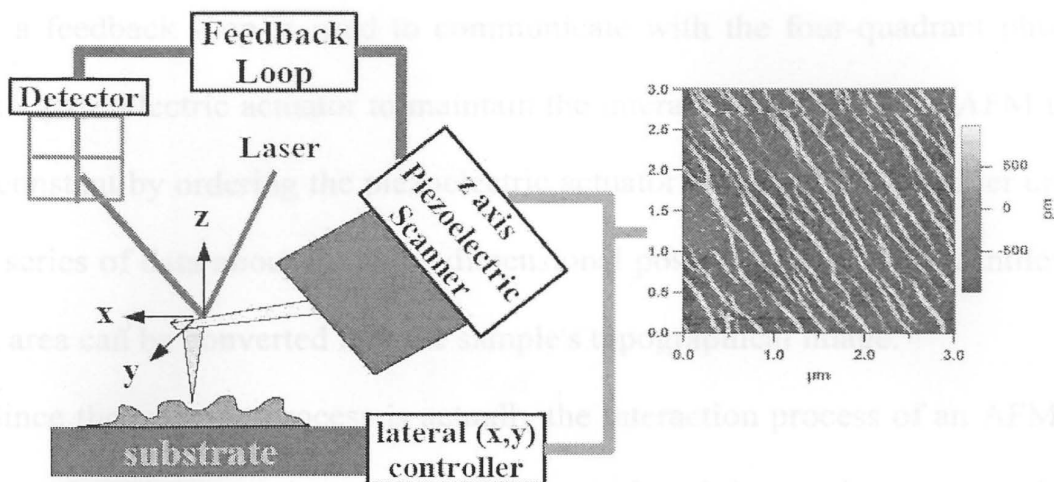
Figure 1.4   A simplified schematic of Atomic Force Microscopy (AFM). The laboratory coordinates are defined by x- and y-axis, and z-axis, the vertical direction. A small sharp tip is attached to one end of a long cantilever. When the tip is brought into close proximity with a sample surface, the forces acting between the AFM tip and the sample will result in a bend of the cantilever. A laser beam is focused on the back of the cantilever and reflects into a four-quadrant photodetector to detect the bend of the the cantilever. The vertical position of the cantilever can be located and controlled by a z-axis piezoelectric actuator and the lateral position of the sample the tip is on can also be located by a lateral controller. During the imaging process, a feedback loop is used to communicate with the four-quadrant photodetector and z-axis piezoelectric actuator to maintain the interaction between the AFM tip and the sample constant by ordering the piezoelectric actuator to bring the cantilever up or down while the tip is scanning the sample's surface line by line. Finally, series of data about the three dimensional position of the AFM cantilever on the scanned area can be converted into the sample's topographical image shown in the right.

process, a feedback loop is used to communicate with the four-quadrant photodetector and z-axis piezoelectric actuator to maintain the interaction between the AFM tip and the sample constant by ordering the piezoelectric actuator to bring the cantilever up or down. Finally, series of data about the three dimensional position of the AFM cantilever on the scanned area can be converted into the sample's topographical image.

Since the imaging process is actually the interaction process of an AFM tip and a sample's surface, it is very important to understand such interaction process. As a matter of fact, there are different force regimes in which forces can be measured with AFM. Fig.1.5 describes vertical forces typically experienced by the tip as the cantilever is brought toward a sample surface. Two force regimes can be distinguished, of which one is the 'attractive regime', where interaction forces such as van der Waals and electrostatic attract the tip to the sample but actual mechanical contact does not occur, and the other is the 'contact regime', where the tip is actually contacting the sample's surface and the outer electronic configuration of tip and sample atoms provide electrostatic and Pauli repulsive forces. While the cantilever is brought close to the sample from the 'attractive regime', the 'contact regime' is reached by a irreversible snap in where the attractive force gradient exceeds the spring constant of the cantilever. However, while the cantilever is brought away from the sample when the tip is touching the sample's surface, finally, the 'attractive regime' is returned by a irreversible snap out where the tensile load on the cantilever overcomes the adhesion between the AFM tip and the sample. In fact, the 'contact regime' is normally an AFM's work regime in which a stable imaging experiment could be conducted. In the 'contact regime', Hooke's Law has to be abided by: $F = -k \times x$, where F

13
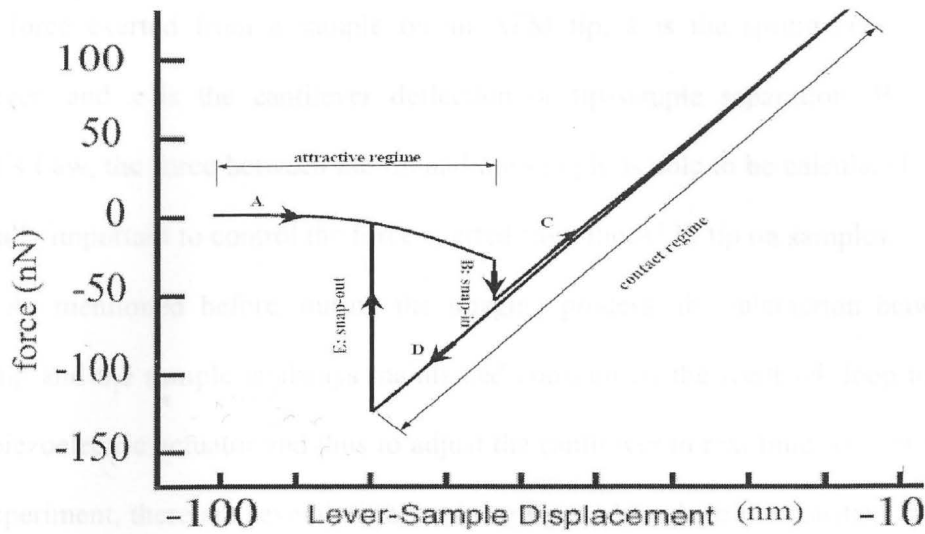
Figure 1.5   Vertical force experienced by the cantilever *vs* cantilever-sample displacement. This displacement is measured between the sample and the rigidly held rear end of the cantilever (opposite to the end with the tip). Of two regimes on the force curve one is the 'attractive regime' where the AFM tip has no actual mechanical contact with sample, and the other is the 'contact regime' where the tip is actually contacting the sample. A: the lever and sample are initially far apart and no forces act. While the lever is brought close to the sample, the tip senses attractive (negative) forces that cause the end of the lever to bend downward. B: the attractive force gradient exceeds the spring constant of the lever at this point, and causes the tip to snap into contact with the sample. C: the lever-sample displacement can continue to be reduced. The tip is in repulsive contact with the sample, the front end of the lever is pushed further upward by positive forces. D: the motion is reversed. Adhesion between the tip and sample maintains the contact although there is now a tensil (negative) load. E: finally the tensile load overcomes the adhesion and the tip snaps out of contact with the sample.[84]

14

is the force exerted from a sample on an AFM tip, k is the spring constant of the cantilever, and x is the cantilever deflection or tip-sample separation. By applying Hooke's Law, the force between the tip and the sample is able to be calculated, which is especially important to control the force exerted from the AFM tip on samples.

As mentioned before, during the imaging process, the interaction between the AFM tip and the sample is always maintained constant by the feedback loop to control the z-piezoelectric actuator and thus to adjust the cantilever in real time. However, in the real experiment, there are several different imaging modes where the constant interaction between the AFM tip and the sample is defined differently. As the very first AFM operation Mode, Contact Mode, also called Constant Force Mode, since performed by Binnig and coworkers in 1986, has become one of the most popular scanning probe modes.[74] In Contact Mode, AFM operates by rastering the tip across the sample and the tip is always in the 'contact regime' shown in Fig.1.5. A constant but extremely low force at a scale of nanonewtons, is maintained on the tip from the sample, and the feedback loop keeps the actual vertical cantilever deflection constant by suitably adapting the tip-sample separation continuously during scanning. And of course, the topographic image of the scanned area can be obtained finally. Moreover, besides the topographic image of the sample, in many AFM machines nowadays, the lateral force image can also be collected.[84-86] As we discussed before, the vertical bend and the lateral twist of the cantilever are simultaneously and independently measured by monitoring the deflection of the reflected laser beam. Features that are not necessarily topographically distinct can show contrast in the lateral force signal due to different friction characteristics. It is

15

obvious that AFM is a very convenient method to analyze friction at an atomic or a nanometer scale because at a constant vertical loading force experienced by the AFM tip, the lateral force could be varied on local areas with different chemical compositions. The lateral force image has been collected on a large variety of samples and has proven capable of providing important information about the friction coefficient of materials. [84-88]

Although imaging in Contact Mode has proven successful, it is not that good for biological samples, and even some soft polymers without any bioactivities. It is widely accepted that a force not exceeding 10^{-11} N might not disturb most of the biological surfaces.[89,90] The constant downward force on the tip often damages (or at least changes) many softer surfaces. In contact mode, biological samples like collagens, DNA, and cells, are often destroyed or at least pushed out of the field of view by the rastering tip. This problem has been well resolved by the development of AC Mode AFM[91-93], which could also appear in literatures as intermittent contact mode AFM, or Tapping Mode AFM[84]. In AC Mode, the cantilever is driven by the z-piezoelectric actuator to oscillate at a frequency close to its main resonant frequency with a certain amplitude and exhibiting a certain phase shift with respect to the driving signal applied to the piezoelectric actuator. However, while the AFM tip is intermittently tapping the sample's surface, the repulsive forces on the tip during intermittent contact lower the oscillation amplitude and change the phase shift.

In AC Mode, the interaction between the AFM tip and the sample is quantified by the oscillation amplitude of the cantilever. So, during the imaging process, the AFM tip-

16

cantilever assembly oscillates and the tip lightly taps the sample surface while the oscillation amplitude is always maintained constant, and finally the topographic image of the sample can be obtained. In AC Mode, the AFM tip only touches the sample at the bottom of each oscillation, and even during the intermittent contact, the energy transferred from the oscillating probe to the sample surface is very much lower than that in Contact Mode. One can find that imaging in AC Mode is especially suitable for the analysis of delicate samples, prevents damage to soft specimens, and avoids the pushing of specimens around on the substrate. Similar to the lateral force image in Contact Mode, in AC Mode, we can obtain the phase image. During the AC Mode imaging, the phase shift of the cantilever with respect to the driving signal applied to the piezoelectric actuator is also collected simultaneously and independently. Materials with different chemical compositions could be of different elasticities, which can definitely cause a different phase shift of the cantilever. Like in the lateral force image, features that are not necessarily topographically distinct could show huge contrast in the phase image due to different chemical compositions.[94-95]

It must be pointed out that when the tip is in the 'contact regime' with a sample, for a typical tip radius, a normal load, and a reasonable elastic constant, the contact area of the tip is not just a single atom. For example, it is reported a 20 nm radius silicon nitride tip experiencing a 1 nN load on a mica sample produces a contact area involving nearly 15 mica unit cells.[84] If adhesion between the AFM tip and sample is taken into account, the contact area is even larger and can ensure a substantial contact area even at the lowest possible applied loads. Since the AFM imaging process is a result of the

17
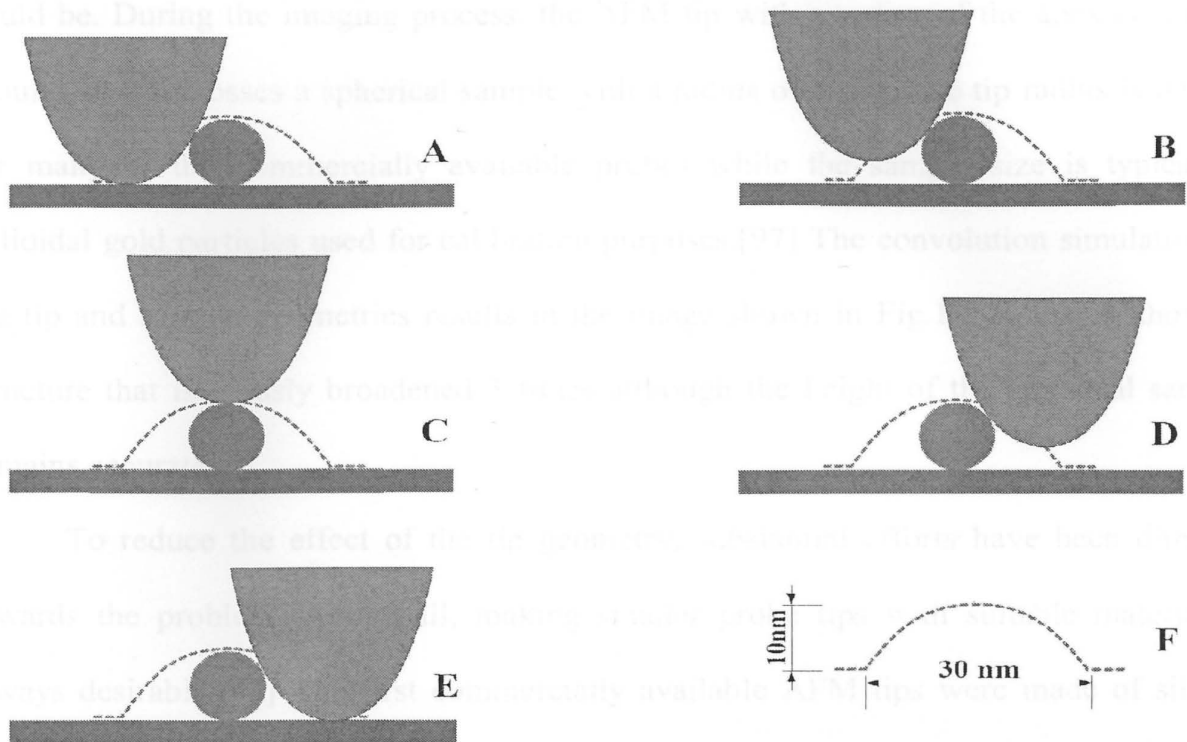
Figure 1.6   An illustration of the AFM imaging process for a spherical sample on a flat surface with a parabolic tip. The AFM tip with a radius of the apex curvature around 10 nm crosses a spherical sample with a radius of 5 nm from A to E. The convolution simulation of the tip and sample geometries results in the image shown in F, which shows a structure that is grossly broadened three times although the height of the spherical sample remains.

interaction between tip and sample, the image obtained is a convolution of the tip and sample geometries.[96-99] The term, convolution, is used to describe the distortions caused by the finite size of the AFM tip, and is of the same meaning as other terms like tip artifact or sample broadening, for the same distortion symptom of AFM images. Fig.1.6 shows a simulated example of what convolution is and what a convoluted image

could be. During the imaging process, the AFM tip with a radius of the apex curvature around 10 nm crosses a spherical sample with a radius of 5 nm. The tip radius is typical for many of the commercially available probes while the sample size is typical of colloidal gold particles used for calibration purposes.[97] The convolution simulation of the tip and sample geometries results in the image shown in Fig.1.6 F, which shows a structure that is grossly broadened 3 times although the height of the spherical sample remains accurate.

To reduce the effect of the tip geometry, substantial efforts have been directed towards the problem. Above all, making smaller probe tips with suitable material is always desirable.[97] The first commercially available AFM tips were made of silicon nitride and were square pyramidal in shape with typical radius at the tip apex of approximately 30 nm.[97,100] Nowadays, novel manufacturing techniques such as electron beam deposition, crystal growth, ion beam etching, and field-emission induced growth, have produced tips with higher aspect ratio, and the small radii up to 1-2 nm. [94,95,101-114] Moreover, many simple algorithms have been applied to separate out the tip and sample in the obtained raw AFM images, which is usually called a deconvolution process. Based on the actual tip geometry characterized by scanning electron micrographs (SEM), the new algorithms can be used to reinterpret the previously obtained images of structures.[96,97]

So far, we discussed some general features of AFM. One thing must be kept in mind is that AFM is not just a imaging tool, but also a surface shaping machine at a molecular scale. AFM tips can act as a molecular brooms to pile proteins up on substrates

19

[115,116] and AFM based techniques like dip-pen nanolithography[117] and scanning probe lithography[118,119] have been used successfully in the preparation of structures on the on the nano-to-mesoscale scales.

1.3 *Bibliography and References*

[1]   K. E. Kadler, D. F. Holmes, J. A. Trotter, J. A. Chapman, *Biochem. J.*, 1996, **316**, 1-11.

[2]   E. Hohenester, J. Engel, *Matrix Biol.*, 2002, **21**, 115-128.

[3]   S. K. Akiyama, K. Nagata, , K. M. Yamada, *Biochim. Biophys. Acta*, 1990, **1031**, 91-110.

[4]   F. Grinnell, *Trends Cell Biol.*, 2003, **13**, 26426-26429.

[5]   F. Jiang, H. Horber, J. Howard, D. J. Muller, *J. Struct. Biol.*, 2004, **148**, 268-278.

[6]   H. A. Goldberg, K. J. Warner, M. C. Li, G. K. Hunter, *Connect Tissue Res.*, 2001, **42**, 25-37.

[7]   R. Fleischmajer, E. D. MacDonald, J. S. Perlish, R. E. Burgeson, L. W. Fisher, *J. Struct. Biol.*, 1990, **105**, 162-169.

[8]   K. Salchert, U. Streller, T. Pompe, N. Herold, M. Grimmer, C. Werner, *Biomacromolecules*, 2004, **5**, 1340-1350.

[9]   P. B. van Wachem, J. A. Plantinga, M. J. B. Wissink, R. Beernink, A. A. Poot, G. H. M. Engbers, T. Beugeling, W. G. van Aken, J. Feijen, M. J. A. van Luyn, *J. Biomed. Mater. Res.*, 2001, **55**, 368-378.

[10]   S. N. Park, H. J. Lee, H. L. Kwang, H. Suh, *Biomaterials*, 2003, **24**, 1631-1641.

[11]   G. A. Di Lullo, S. M. Sweeney, J. Korkko, L. Ala-Kokko, J. D. San Antonio, *J. Biol. Chem.*, 2002, **277**, 4223-4231.

[12]   M. Kuberka, I. Heschel, B. Glasmacher, G. Rau, *Biomed. Technol.*, 2002, **47**,

485-487.

[13]   G. He, A. George, *J. Biol. Chem.*, 2004, **279**, 11649-11656.

[14]   J. M. Berg, J. L. Tymoczko, L. Stryer, *Biochemistry*, (5th ed.), **2002**, W. H. Freeman and Co.: NY.

[15]   S. R. Lamande, J. F. Bateman, *Semin. Cell Dev. Biol.*, 1999, **10**, 455-464.

[16]   A. Rich, F. H. C. Crick, *J. Mol. Biol.*, 1961, **3**, 483-506.

[17]   R. Ross, P. Bornstein, *Sci. Amer.*, 1971, **224**, 44-52.

[18]   M. L. Tanzer, *science*, 1973, **180**, 561-566.

[19]   L. I. Fessler, N. P. Morris, J. H. Fessler, *Proc. Natl. Acad. Sci. USA*, 1975, **72**, 4905-4909.

[20]   J. H. Fessler, L. I. Fessler, *Ann. Rev. Biochem.*, 1978, **47**, 129-162.

[21]   R. R. Bruns, D. J. S. Hulmes, S. F. Therrien, J. Gross, *Proc. Natl. Acad. Sci. USA*, 1979, **76**, 313-317.

[22]   D. R. Eyre, *Science*, 1980, **207**, 1315-1322.

[23]   J. Bella, M. Eaton, B. Brodsky, H. M. Berman, *Science*, 1994, **266**, 75-81.

[24]   B. Brodsky, J. A. M. Ramshaw, *Matrix Biol.*, 1997, **15**, 545-554.

[25]   J. Baum, B. Brodsky, *Curr. Opin. Struct. Biol.*, 1999, **9**, 122-128.

[26]   D. J. Prockop, K. I. Kivirikko, *Annu. Rev. Biochem.*, 1995, **64**, 403-434.

[27]   J. K. Rainey, M. C. Goh, *Bioinformatics*, 2004, **20**, 2458-2459.

[28]   J. K. Rainey, M. C. Goh, *Protein Science*, 2002, **11**, 2748-2754.

[29]   K. E. Kadler, *Protein Profile*, 1995, **2**, 491-619.

[30]   M. F. Paige, J. K. Rainey, M. C. Goh, *Biophys. J.*, 1998, **74**, 3211-3216.

[31]   J. H. Bradt, M. Mertig, A. Teresiak, W. Pompe, *Chem. Mater.*, 1999, **11**, 2694-2701.

[32]   A. Chapman, M. Tzaphlidou, K. M. Meek, K. E. Kadler, *Electron Microsc. Rev.*, 1990, **3**, 143-182.

[33]   D. Xia, C. A. Yu, H. Kim, J. Z. Xia, A. M. Kachurin, Zhang L, L. Yu, J. Deisenhofer, *Science*, 1997, **277**, 60-66.

[34]   K. Ozawa, Y. Takayama, F. Yasukawa, T. Ohmura, M. A. Cusanovich, Y. Tomimoto, H. Ogata, Y. Higuchi, H. Akutsu, *Biophys. J.*, 2003, **85**, 3367-3374.

[35]   A. Dikiy, W. Carpentier, I. Vandenberghe, M. Borsari, N. Safarov, E. Dikaya, J. Van Beeumen, S. Ciurli, *Biochemistry*, 2002, **17**, 14689-14699.

[36]   M. Nishikimi, S. Udenfriend, *Trends Biochem. Sci.*, 1977, **2**, 111-112.

[37]   J. A. Vranka, L. Y. Sakai, H. P. Bächinger, *J. Biol. Chem.*, 2004, **279**, 23615-23621.

[38]   R.A. Berg, D. J. Prockop, *Biochem. Biophys. Res. Comm.*, 1973, **52**, 115-120.

[39]   K. E. Kadler, Y. Hojima, D. J. Prockop, *J. Biol. Chem.*, 1988, **263**, 10517-10523.

[40]   D. E. Birk, R. L. Trelstad, *J. Cell Biol.*, 1986, **103**, 231-240.

[41]   R. Z. Wang, F. Z. Cui, H. B. Lu, H. B. Wen, C. L. Ma, H. D. Li, *J. Mater. Sci. Lett.*, 1995, **14**, 490-492.

[42]   S. A. Jimenez, R. I. Bashey, M. Benditt, R. Yankowski, *Biochem. Biophys. Res. Commun.*, 1977, **78**, 1354-1361.

[43]   J. C. Hadley, K. M. Meek, N. S. Malik, *Glycoconjugate Journal*, 1998, **15**, 835-840.

[44] D. F. Holmes, C. J. Gilpin, C. Baldock, U. Ziese, A. J. Koster, K. E. Kadler, *Proc. Natl. Acad. Sci. USA*, 2001, **98**, 7307-7312.

[45] N. A. Guzman (ed.) *Prolyl Hydroxylase, Protein Disulfide Isomerase, and Other Structurally Related Proteins*, **1997**, Marcel Decker, Inc., New York, USA.

[46] S. Seifter, E. Harper, the collagenases, in P. D. Boyer (ed.), *The Enzymes* (3rd ed.), **1971**, vol. 3, pp. 649-697, Academic Press.

[47] R. Kuypers, M. Tyler, L. B. Kurth, I. D. Jenkins, D. J. Horgan, *Biochem. J.*, 1992, **283**, 129-136.

[48] P. Bornstein, A. H. Kang, K. A. Piez, *Proc. Natl. Acad. Sci. USA*, 1966, **55**, 417-424.

[49] A. Pirskanen, A. M. Kaimio, R. Myllylä, K. I. Kivirikko, *J. Biol. Chem.*, 1996, **271**, 9398-9402.

[50] A. L. Boskey, R. Mendelsohn, *Vib. Spectrosc.*, 2005, **38**, 107-114.

[51] P. J. Knight, N. S. Fortune, M. A. Geeves, *Biophys. J.*, 1993, **65**, 814-822.

[52] W. Traub, T. Arad, S. Weiner, *Matrix*, 1992, **12**, 251-255.

[53] I. Jager, P. Fratzl, *Biophys. J.*, 2000, **79**, 1737-1746.

[54] D. D. Wallis, E. A. Putnam, J. S. Cretoiu, S. G. Carmical, S. N. Cao, G. Thomas, D. M. Milewicz, *J. Cell Biochem.*, 2003, **90**, 641-652.

[55] V. I. Shestopalov, S. Bassnett, *J. Cell Sci.*, 2003, **116**, 4191-4199.

[56] A. V. Persikov, B. Brodsky, *Proc. Natl. Acad. Sci. USA*, 2002, **99**, 1101-1103.

[57] A. A. Day, C. I. Ramis, L. W. Fisher, P. Gehron-Robey, J. D. Termine, M. F. Young, *Nucleic Acids Res.*, 1986, **14**, 9861-9876.

[58] P. Stoller, K. M. Reiser, P. M. Celliers, A. M. Rubenchik, *Biophys. J.*, 2002, **82**, 3330-3342.

[59] M. J. Seibel, *Clin. Biochem Rev.*, 2005, **26**, 97-122.

[60] A. S. Narayanan, R. C. Page, J. Swanson, *Biochem. J.*, 1989, **260**, 463-469.

[61] H. Ohkubo, G. Vogeli, M. Mudryj, V. E. Avvedimento, M. Sullivan, I. Pastan, B. de Crombrugghe, *Proc. Natl. Acad. Sci. USA*, 1980, **77**, 7059-7063.

[62] F. O. Sangiorgi, V. Benson-Chanda, W. J. de Wet, M. E. Sobel, F. Ramirez, *Nucleic Acids Res.*, 1985, **13**, 2815-2826.

[63] M. C. Ryan, L. J. Sandell, *J. Biol. Chem.*, 1990, **265**, 10334-10339.

[64] R. E. Burgeson, P. A. Hebda, N. P. Morris, D. W. Hollister, *J. Biol. Chem.*, 1982, **257**, 7852-7856.

[65] V. A. Luckow, M. D. Summers, *Biotechnology*, 1988, **6**, 47-55.

[66] I. M. Kidd, V. C. Emery, *Appl. Biochem. Biotechnol.*, 1993, **42**, 137-159.

[67] M. T. DiMuzio, M. Bhown, W. T. Butler, *Biochem. J.*, 1983, **216**, 249-257.

[68] S. Gronthos, M. Mankani, J. Brahim, P. G. Robey, S. Shi, *Proc. Natl. Acad. Sci. USA*, 2000, **97**, 13625-13630.

[69] L. J. Schreiner, I. G. Cameron, N. Funduk, L. Miljković, M. M. Pintar, D. N. Kydon, *Biophys. J.*, 1991, **59**, 629-639.

[70] F. P. Ross, A. M. Christiano, *J. Clin. Invest.*, 2006, **116**, 1140-1149.

[71] L. Silverman, A. L. Boskey, *Calcif. Tissue Int.*, 2004, **75**, 494-501.

[72] G. Binnig, H. Rohrer, Ch. Gerber, E. Weibel, *Phys. Rev. Lett.*, 1982, **49**, 57-61.

[73] D. W. Pohl, W. Denk, M. Lanz, *Appl. Phys. Lett.*, 1984, **44**, 651-653.

25

[74]   G. Binnig, C. F. Quate, Ch. Gerber, *Phys. Rev. Lett.*, 1986, **56**, 930-933.

[75]   K. K. Berggren, A. Bard, J. L. Wilbur, J. D. Gillaspy, A. G. Helg, J. J. McClelland, S. L. Rolston, W. D. Phillips, M. Prentiss, G. M. Whitesides, *Science*, 2000, **260**, 1255-1257.

[76]   R. D. Piner, J. Zhu, F. Xu, S. Hong, C. A. Mirkin, *Science*, 1999, **283**, 661-663.

[77]   S. Hong, C. A. Mirkin, *Science*, 2000, **288**, 1808-1811.

[78]   U. Kleineberg, A. Brechling, M. Sundermann, U. Heinzmann, *Adv. Funct. Mater.*, 2001, **11**, 208-212.

[79]   Q. J. Chi, O. Farver, J. Ulstrup, *Proc. Natl. Acad. Sci. USA*, 2005, **102**, 16203-16208.

[80]   J. D. Gerding, D. M. Willard, A. Van Orden, *J. Am. Chem. Soc.*, 2005, **127**, 1106-1107.

[81]   F. Cattaruzza, A. Cricenti, A. Flamini, M. Girasole, G. Longo, T. Prosperi, G. Andreano , L. Cellai, E. Chirivino, *Nucleic Acids Res.*, 2006, **34**, e32.

[82]   F. L. Brown, D. M. Leitner, J. A. McCammon, K. R. Wilson, *Biophys. J.*, 2000, **78**, 2257-2269.

[83]   A. Cricenti, R. Generosi, M. Luce, P. Perfetti, G. Margaritondo, D. Talley, J. S. Sanghera, I. D. Aggarwal, N. H. Tolk, A. Congiu-Castellano, M. A. Rizzo, D. W. Piston, *Biophys. J.*, 2003, **85**, 2705-2710.

[84]   R. W. Carpick, M. Salmeron, *Chem. Rev.*, 1997, **97**, 1163-1194.

[85]   U. Landman, W. D. Luedtke, A. Nitzan, *Surf. Sci.*, 1989, **210**, L177-L184.

[86]   U. Landman, W. D. Luedtke, M. W. Ribarsky, *J. Vac. Sci. Technol. A*, 1989, **7**,

2829-2839.

[87]   J. Krim, *Comments Condens. Matter. Phys.*, 1995, **17**, 263-265.

[88]   E. Meyer, R. Overney, D. Brodbeck, L. Howald, R. Lüthi, J. Frommer, H.-J. Güntherodt, *Phys. Rev. Lett.*, 1992, **69**, 1777-1780.

[89]   O. M. Leung, M. C. Goh, *Science*, 1994, **255**, 64-66.

[90]   A. L. Weisenhorn, P. K. Hansma, T. R. Albrecht, C. F. Quate, *Appl. Phys. Lett.*, 1989, **54**, 2651-2653.

[91]   D. R. Bérard, P. Attard, G. N. Patey, *J. Chem. Phys.*, 1993, **98**, 7236-7239.

[92]   P. K. Hansma, J. P. Cleveland, M. Radmacher, D. A. Walters, P. E. Hillner, M. Bezanilla, M. Fritz, D. Vie, H. G. Hansma, C. B. Prater, J. Massie, L. Fukunage, J. Gurley, V. Elings, *Appl. Phys. Lett.*, 1994, **64**, 1738-1740.

[93]   N. Ishida, T. Inoue, M. Miyahara, K. Higashitani, *Langmuir*, 2000, **16**, 6377-6380.

[94]   D. Raghavan, M. VanLandingham, X. Gu, and T. Nguyen, *Langmuir*, 2000, **16**, 9448-9459.

[95]   D. Raghavan, X. Gu, T. Nguyen, M. VanLandingham, A. Karim, *Macromolecules*, 2000, **33**, 2573-2583.

[96]   P. Markiewicz, M. C. Goh, *Langmuir*, 1994, **10**, 5-7.

[97]   P. Markiewicz, M. C. Goh, *J. Vac. Sci. Technol. B*, 1995, **13**, 1115-1118.

[98]   S. S. Sheiko, M. Moller, A. M. C. Reuvekamp, H. W. Zandbergen, *Phys. Rev. B*, 1993, **48**, 5675-5678.

[99]   P. Grutter, W. Zimmermann-Edling, D. Brodbeck, *Appl. Phys. Lett.*, 1992, **60**,

2741-2744.

[100]   T. R. Albrecht, S. Akamine, T. E. Carver, C. F. Quate, *J. Vac. Sci. Technol. A*, 1990, **8**, 3386-3396.

[101]   M. Yamaki, T. Miwa, H. Yoshimura, K. Nagayama, *J. Vac. Sci. Technol. B*, 1992, **10**, 2447-2250.

[102]   H. G. Hansma, K. A. Browne, M. Bezanilla, T. C. Bruice, *Biochemistry*, 1994, **33**, 8436-8441.

[103]   S. S. Wong, J. D. Harper, P. T. Lansbury, Jr., C. M. Lieber, *J. Am. Chem. Soc.*, 1998, **120**, 603-604.

[104]   J. H. Hafner, C. L. Cheung, C. M. Lieber, *Nature*, 1999, **398**, 761-762.

[105]   C. V. Nguyen, K. J. Chao, R. M. D. Stevens, L. Delzeit, A. Cassell, J. Han, M. Meyyappan, *Nanotechnology*, 2001, **12**, 363-367.

[106]   R. M. D. Stevens, C. Nguyen, A. Cassell, L. Delzeit, M. Meyyappan, J. Han, *Appl. Phys. Lett.*, 2000, **77**, 3453-3457.

[107]   E. S. Snow, P. M. Campbell, J. P. Novak, *Appl. Phys. Lett.*, 2002, **80**, 2002-2004.

[108]   C. V. Nguyen, R. M. D. Stevens, J. Barber, J. Han, M. I. Sanchez, C. Larson, W. D. Hinsberg, *Appl. Phys. Lett.*, 2002, **81**, 901-903.

[109]   T. Larsen, K. Moloni, F. Flack, M. A. Eriksson, M. G. Lagally, C. T. Black, *Appl. Phys. Lett.*, 2002, **80**, 1996-1998 .

[110]   N. de Jonge, Y. Lamy, M. Kaiser, *Nano Lett.*, 2003, **3**, 1621-1624.

[111]   C. L. Cheung, J. H. Hafner, T. W. Odom, K. Kim, C. M. Lieber, *Appl. Phys.*

28

Lett., 2000, **76**, 3136-3138 .

[112] Q. M. Hudspeth, K. P. Nagle, Y.-P. Zhao, T. Karabacak, C. V. Nguyen, M. Meyyappan, G.-C. Wang, T.-M. Lu, *Surf. Sci.*, 2002, **515**, 453-461.

[113] C. H. Oon, J. T. L. Thong, Y. Lei, W. K. Chim, *Appl. Phys. Lett.*, 2002, **81**, 3037-3039 .

[114] A. B. H. Tay, J. T. L. Thong, *Appl. Phys. Lett.*, 2004, **84**, 5207-5209.

[115] A. S. Lea, A. Pungor, V. Hlady, J. D. Andrade, J. N. Herron, E. W. Voss Jr, *Langmuir*, 1992, **8**, 68-13.

[116] F. Jiang, K. Khairy, K. Poole, J. Howard, D. J. Muller, *Microsc. Res. Tech.*, 2004, **64**, 435-440.

[117] D. L. Wilson, R. Martin, S. Hong, M. Cronin-Golomb, C. A. Mirkin, D. L. Kaplan, *Proc. Natl. Acad. Sci. USA*, 2001, **98**, 13660-13664.

[118] L. M. Demers, D.S. Ginger, S. J. Park, Z. Li, S. W. Chung, C.A. Mirkin, *Science*, 2002, **296**, 1836-1838.

[119] K. B. Lee, S. J. Park, C. A. Mirkin, J. C. Smith, M. Mrksich, *Science*, 2002, **295**, 1702-1705.

Chapter 2

Imaging Type I collagen monomers in air
by Atomic Force Microscopy

2.1 *Introduction*

Although electron microscopy [1-3] and X-ray diffraction [4,5] have been the main resources in exploring the structure of collagen fibrils and their mineralization process over decades, other techniques such as AFM (atomic force microscopy) [6,7], FTIR(Fourier Transform Infrared) spectroscopy [8], and optical tweezers [9] can also provide important information from different aspects of the properties of collagen and the biomineralization process.

Among all of the techniques mentioned above, AFM has been widely applied more recently to solve some biological puzzles due to its advantages [10]: AFM has a really high resolution (angstroms), it can be operated under physiological conditions, which means no need to pretreat samples before imaging, and of course only small amounts of samples are required.

As the molecular unit of collagen fibrils, each collagen monomer consists of three polypeptide chains coiled around each other and thus forms a triple helix. In every single chain of a collagen monomer helix, every three amino acid residues there must be a glycine to adapt the final triple-helical structure and others present abundantly are most likely to be proline and hydroxyproline. Among more than 20 types of monomers, Type I collagen is the most abundant one found in animals and is also one of the species which

can self assembly into fibrils of 67 nm axial periodicity (*D*-banding). [2]

Early collagen studies involving AFM and collagen were carried out under dry conditions [6,11], and even recently, drying samples before imaging is also necessary for monomer imaging [12]. Actually, another approach to study monomers was carried out by binding monomers covalently to substrate. [13] However, this work requires chemical modification of collagen monomers and was difficult to get done. As we know, when collagen monomer solution drops on a substrate, monomers are not so easy to bind the surface of the substrate: first, the ionic screen created by buffer solution can prevent such binding to some extent; secondly, the equilibrium of dissolution and precipitation of collagen monomers and the equilibrium of adsorption and desorption of collagen monomers can also cause drastic local disturbance; moreover the interaction between monomers and the surface of the substrate (normally van der Waals force) is really weak, the force applied to monomers by the AFM tip can easily drag the molecules away. When all of the aspects are taken into account, it seems that imaging collagen monomers in buffer solution is impossible. Actually, so far, no such reports about imaging monomers with AFM under physiological condition are available.

Another concern for collagen monomer imaging is that collagen molecules can easily self assembly into fibrils at low concentration, appropriate pH and temperature.[1] So, in order to image collagen monomers, a low concentration of collagen monomer solution is necessary to get a low coverage on the substrate surface and thus to single out individual monomers. It is reported that Tris-HCl, glucose, and arginine can interfere with the collagen fibrillogenesis process.[14,15] So, we chose Tris-HCl as the buffer for

31

sample preparation.

2.2 *Experimental procedures*

Preparation of collagen monomers on mica surface

All the chemical reagents used were of analytical grade and prepared with ultrapure water (18 MΩ Barnsted Nanopure). 3.0 mg/ml VITROGEN (purified) collagen for cell culture and biochemistry (pH 2.0, dissolved in 0.012 M HCl) was purchased from Cohesion (California, USA) and stored at 4 ˚C. VITROGEN (purified) collagen is 99.9 % pure collagen which is 95-98 % Type I collagen with the remainder being comprised of type III collagen. For preparation, the collagen was first diluted in a buffer (pH 7.5) of 50 mM Tris-HCl and 200 mM KCl to get a solution of a concentration of 30 μg/ml. Then 0.3 μg/ml collagen solution was obtained by diluting the 30 μg/ml collagen solution into the same buffer. As substrates, freshly cleaved square-shape mica pieces (9.0 mm × 9.0 mm) were used. After being freshly cleaved, a mica surface was flushed with a collagen solution. Then, the sample was gently rinsed firstly by the same Tris-HCl buffer to remove molecules only loosely bound to the surface and secondly by ultrapure water to avoid any salt crystal formation. Finally, the sample was dried using a gentle stream of dry air. All the samples were prepared at room temperature.

Imaging collagen monomers by AFM

The AFM imaging experiment were carried out by the Molecular Force Puller, MFP 3D (Asylum Research, Santa Barbara, CA, USA). Silicon cantilevers having a typical force constant of 4.5 N/m (NSC35/AIBS) were purchased from MicroMasch

(Estonia). Images were obtained with AC Mode at a RMS amplitude of around 75 nm and a drive frequency of 192 kHz close to the resonance frequency of the cantilever in air. All the samples were imaged in air at room temperature.

2.3 *Results and discussion*

As mentioned before, since imaging monomers under physiological condition is not likely so far, we carried out experiments just with dry samples on mica surface. We also used Tris-HCl buffer to prepared samples since it was reported Tris-HCl could prevent collagen fibrillogenesis to some extent. And considering that collagen concentration is also a main issue, we prepared two groups of samples: one is of a concentration of 30 μg/ml collagen and the other 0.3 μg/ml.

First, the sample made by 30 μg/ml collagen was mounted for scanning. The AFM topographic image (Fig.2.1 A) shows the monomers (or protofibrils) on the mica surface. From the image, we can see collagen monomers (or protofibrils) are distributed randomly on the mica surface. After analyzing the data, we found that: the average height of the monomers (or protofibrils) is around 0.8 nm; the average length is around 200 nm but not so accurate since collagen monomers are densely entangled with each other; and the overall distribution of collagen monomers on an area of 3.0 μm $\times$ 3.0 μm is really even. As we know, the characteristics of Type I collagen monomer are: a collagen triple helix, 300 nm in length and 1.5 nm in diameter. But in our study, 30 μg/ml collagen might be too concentrated and the monomers were entangled together, which means the contour length of a single monomer may be around 300 nm. Since the sample was also dried for

33
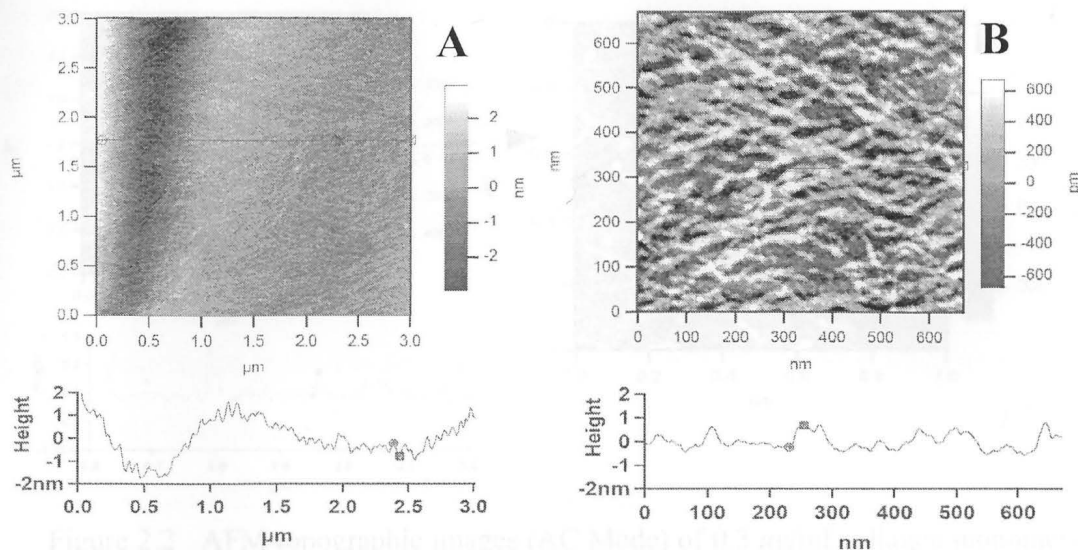
Figure 2.1   AFM topographic images (AC Mode) of 30 μg/ml collagen monomers in Tris-HCl buffer on mica with the line-scan height spectra shown below. A, a scan area of 3.0 μm × 3.0 μm; B, a scan area of 650 nm × 650 nm.

imaging, molecules are easily collapsed on the mica surface by both the binding force between the collagen monomers and the substrate (van der Waals force) and the force loaded by the AFM tip.[12] A zoom-in scan in a small area (see Fig.2.1 B) is consistent with Fig.2.1 A, but gives a better resolution. In sum, the sample made by 30 μg/ml collagen solution did not give good monomer images (actually we can hardly tell if they are monomers or protofibrils) and a lower concentration may be better for sample preparation.

Now, we can take a look at the sample made by 0.3 μg/ml collagen solution. From Fig.2.2A we can see collagen monomers are also randomly but very loosely distributed on the mica surface and single monomers can be easily distinguished. The average
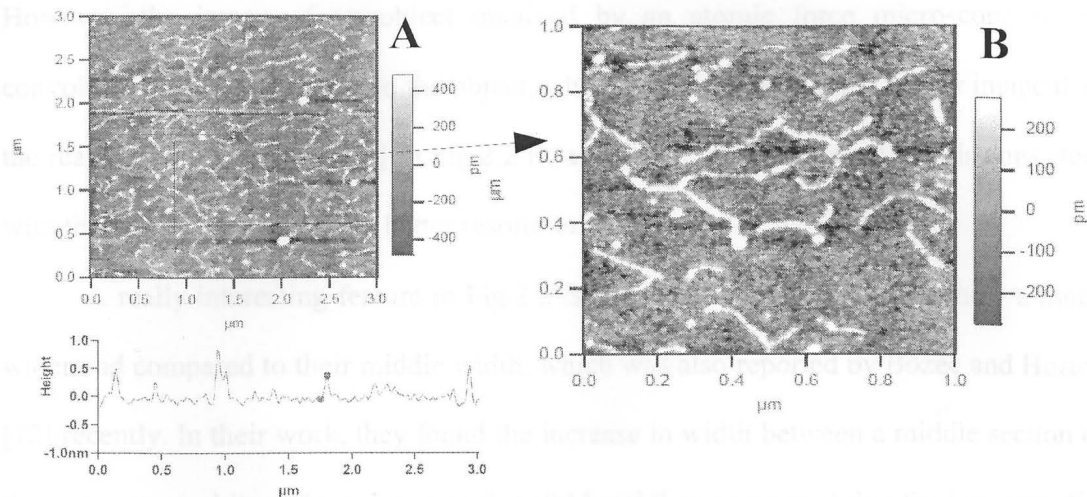
Figure 2.2   AFM topographic images (AC Mode) of 0.3 μg/ml collagen monomers in Tris-HCl buffer on mica: A, a scan area of 3.0 μm × 3.0 μm with the line-scan height spectrum shown below the image; B, a zoom-in scan on an area of 1.0 μm × 1.0 μm. Monomers appear to have the expected length of 290 nm although the heights are lower than expected.

contour length of monomers on an area of 3.0 μm × 3.0 μm is around 290 nm, which is really close to the classic value of 300 nm, but the average height of collagen monomers is only around 0.4 nm. Although the results are not the same as we expected, it confirmed our hypothesis: a collagen monomer is easily collapsed on the mica surface by both the binding force between the collagen monomer and the substrate (van der Waals force) and the force loaded by the AFM tip, which results in a flat but thin strip of around 300 nm in length. This time, we also measured the width of the monomers since no entanglement occurred on the mica surface and we found that the average width of monomers is around 40 nm, which is much bigger than classic diameter of Type I collagen monomers.

35

However, the image of an object obtained by an atomic force microscope is the convolution of the AFM tip and the object, which probably results in a bigger image than the real size of the object. [16] In Fig.2.2 B, a zoom-in scan in a small area is consistent with the Fig.2.2 A, but gives a better resolution.

A really interesting feature in Fig.2.2 is that most of the monomers show a much wider end compared to their middle width, which was also reported by Bozec and Horton [12] recently. In their work, they found the increase in width between a middle section of the monomer and its end can be up to threefold and they accounted that for two potential reasons: one is that the characteristics of tropocollagen (originated from procollagen by cleaving both the amino and the carboxylic termini) can result in fray on the ends of a monomer; the other is a hairpin conformation with the *C*-terminus folded back onto the triple helix. However, in their experiments, it seems they just ignored many bigger objects discretely distributed around. In our experiment, we found such ends are much bigger (the average height is around 1.6 nm, and the average width is around 100 nm) than the monomers around (0.4 nm in height and 10 nm in width) and also lots of round things discretely distributed around. If such ends are caused by fraying, the height and width of the residue left could not be bigger than normal monomers. For the other reason, even if a hairpin structure was formed, it is not possible to cause such a drastic change in the ends. It is true that *N*-propeptides of the Type I procollagen can form a bent-back conformation on the *N*-terminus [17-20], but in our cases tropocollagens (after cleaving both the *C*-propeptides and the *N*-propeptides on procollagens) were used instead. Actually the *N*-telopeptide of Type I collagen monomers can also form a hairpin loop on

36

the N-terminus but instead of on the axial helix [21], which can probably be overlooked (only at most 3 nm in diameter) while compared to the whole monomer. Another possible reason is that while the sample was drying before imaging, monomers were also experienced the denaturation process; for denatured monomers strongly bound to mica surface, the general shape was maintained, but for monomers loosely bound, they could retract from the free end to form balls caused by entropy force driven by water, or rupture first and then retract to form smaller balls.

It was also noticed by Bozec and Horton [12] that there was a repetitive pattern (around 8 nm) observable along the length of the collagen monomers and they accounted
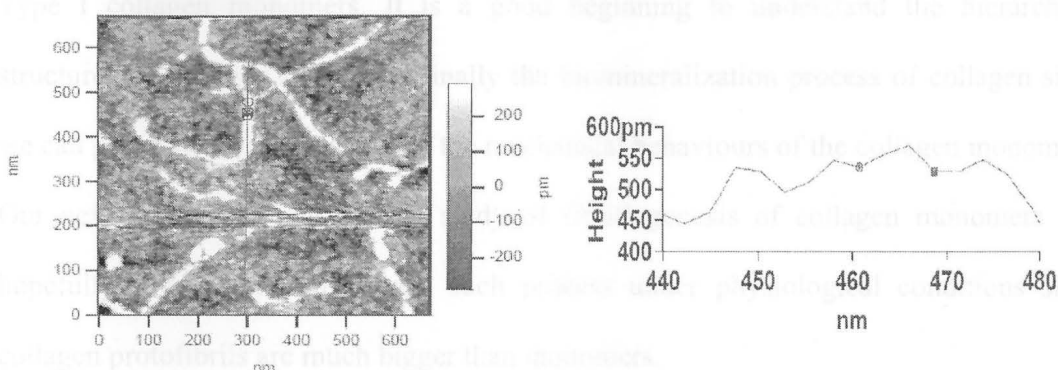
Figure 2.3   AFM topographic image (AC Mode) of 0.3 μg/ml collagen monomers in Tris-HCl buffer on mica with a scan area of 650 nm × 650 nm; and the line-scan height spectrum longitudinally aligned on a monomer is showed on the right of the image. Although the section does show features of around 8 nm periodicity as reported in [12], this may be an image artifact.

for that with the coil-pitch of the collagen monomer. In our experiment, we also found such pattern which can be seen in Fig.2.3, but it is not so convincing since the end of the

AFM tip has the similar dimensions as those of the pattern and thus could create a false image. This may also be the case in Bozec and Horton's work. Moreover, although the main part of collagen monomers is a right-handed super triple helix with a periodic supercoil pitch around 8 nm, the three composite chains by themselves are in a left-handed helical conformation of a periodic coil-pitch around 1 nm, which could be more dominant for the apparent spatial periodicity than the superhelix of the whole molecules.

2.4 *Conclusion*

Summarily, in our work we successfully imaged the topographic properties of Type I collagen monomers. It is a good beginning to understand the hierarchical structures of collagen fibrils and finally the biomineralization process of collagen since we can get some direct evidence of the mechanical behaviours of the collagen monomers. Our next step will focus on the study of fibrillogenesis of collagen monomers and hopefully, we can directly image such process under physiological conditions since collagen protofibrils are much bigger than monomers.

2.5 *Bibliography and References*

[1]   R. L. Trelstad, K. Hayashi, J. Gross, *Proc. Natl. Acad. Sci., USA*, 1976, **73**, 4027-4031.

[2]   K. E. Kadler, D. F. Holmes, J. A. Trotter, J. A. Chapman, *Biochem. J.*, 1996, **316**, 1-11.

[3]   A. J. Hodge, J. A. Petruska, *Recent studies with the electron microscope on ordered aggregates of the tropocollagen molecule*, in G. N. Ramachandran, (Ed.), *Aspects of Protein Chemistry*, **1963**, pp. 289-300, Academic Press, London.

[4]   D. J. S. Hulmes, A. Miller, S. W. White, B. Brodsky-Doyle, *J. Mol. Biol.*, 1977, **110**, 643-666.

[5]   J. Bradt, M. Mertig, A. Teresiak, W. Pompe, *Chem. Mater.*, 1999, **11**, 2694-2701.

[6]   D. Baselt, J. Revel, J. Baldeschwieler, *Biophys. J.*, 1993, **65**, 2644-2655.

[7]   J. K. Rainey, C. K. Wen, M. C. Goh, *Matrix Biol.*, 2002, **21**, 647-660.

[8]   E. P. Paschalis, O. Jacenko, B. Olsen, R. Mendelsohn, L. Boskey, *Bone*, 1996, **19**, 151-156.

[9]   Y. Sun, Z. Luo, A. Fertala, K. An, *Biochem. Biophys. Res. Commun.*, 2002, **295**, 382-386.

[10]   D. Czajkowsky, H. Iwamoto, Z. F. Shao, *J. Electron Microsc.*, 2000, **49**, 395-406.

[11]   M. Gale, M. S. Pollanen, P. Markiewicz, M. C. Goh, *Biophys. J.*, 1995, **68**, 2124-2128.

[12]   L. Bozec, M. Horton, *Biophys. J.*, 2005, **88**, 4223-4231.

[13]   R. Rounsevell, J. R. Forman, J. Clarke, *Methods*, 2004, **34**, 100-111.

[14]   J. Gross, D. Kirk, *J. Bio. Chem.*, 1958, **233**, 355-360.

[15]   T. Hayashi, Y. Nagai, *J. Biochem.*, 1972, **72**, 749-758.

[16]   P. Markiewicz, M. C. Goh, *J. Vac. Sci. Technol. B*, 1995, **13**,1115-1118.

[17]   A. P. Mould, D. J. S. Hulmes, D. F. Holmes, C. Cummings, C. H. Sear, J. A. Chapman, *J. Mol. Biol.*, 1990, **211**, 581-594.

[18]   D. F. Holmes, A. P. Mould, J. A. Chapman, *J. Mol. Biol.*, 1991, **220**, 111-123.

[19]   R. B. Watson, G. A. Wallis, D. F. Holmes, D. Viljoen, P. H. Byers, K. E. Kadler, *J. Biol. Chem.*, 1992, **267**, 9093-9100.

[20]   D. F. Holmes, R. B. Watson, B. Steinmann, K. E. Kadler, *J. Biol. Chem.*, 1993 **268**, 15758-15765.

[21]   D. L. Helseth, J. H. Lechner, A. Veis, *Biopolymers*, 1979, **18**, 3005-3014.

40

Chapter 3

Patterned two dimensional collagen protofibrils created by a Bottom-up method
-----the quasiepitaxial growth of collagen fibrils on substrates

3.1 *Introduction*

Although epitaxy might not be a term familiar to many biochemists, it is a thoroughly investigated topic by chemists and physicists. Epitaxy, as in the case of inorganic materials, refers to the growth of the crystals of one mineral on the crystal face of another mineral so that both minerals have the same crystalline structural orientation at the interface, or in a more technical way, refers to systems where there is a one-to-one commensurate relationship between the molecular positions in the deposited layer and the substrate.[1] For over half a century, with the growing interest in molecular organic materials for creating optoelectronic devices, controlling the structure and growth dynamics of organic molecular thin films and organic molecular crystals on inorganic substrates has been stimulating many systematical theoretical and experimental approaches in this promising area.[1-8] Such materials combine the promise of the widely tunable properties of organic molecules brought by organic synthetic chemistry, a high degree of microscopic structural control by choosing a wide range of substrates, and the ultrahigh vacuum technique of organic molecular beam deposition, and have desirable functions such as exciton confinement in grown multiple quantum well structures.[8]

41

The most common means for the organic molecular beam deposition growth is to use an ultrahigh vacuum apparatus as a background in which a highly purified powder of the organic source material from a temperature-controlled oven gives off its evaporant, passes a series of collimated orifices, and is finally deposited on a substrate held perpendicular to the beam approximately 10-20 cm from the source.[1] It has been proven that the epitaxial growth of organic molecular thin films or organic molecular crystals on substrates are dominated by two factors, of which one is the bond energy between organic molecules and the substrate, and the other is the crystal lattice matching between organic molecular crystals and the substrate.[1] For conventional epitaxy, the bond energy between absorbed layer and the substrate is huge because the molecules are chemisorbed onto the substrate surface while mismatches between the substrate and absorbed layer's lattices are really slight.[1]

However, for many organic molecules, only electrostatic forces and van der Waals forces dominate the weak physisorption between the molecules and the substrate. A surface organic molecule could translationally move on the substrate lattices without a significant change in energy. Moreover, the inorganic substrate and organic film are incommensurate over any meaningful lattice length scale. From this view, for most organic molecules, the absorbed films on substrates are actually some quasiepitaxial structures.[1] Since the substrate and the absorbed organic molecular film's lattices do not match that well, the organic molecular film is distorted from its bulk lattice structure and strain develops in the film if the absorbed film has to conform to the substrate lattice.

On the other hand, for such quasiepitaxial growth process, the intralayer

42

interaction between organic molecules, which is largely responsible for determining the undistorted organic crystals, is even stronger than the interaction between the absorbed layer and the substrate in many cases. It was assumed that in those cases, one or two strained "wetting" layers electrostatically attracted on the substrate might grow first. If molecular beam deposition continues, due to the strong intralayer interaction between organic molecules, crystallites could be nucleated at the substrate-film interface, the lattice structure almost immediately relaxes into its bulk crystals, resulting in numerous small crystallite domains without significant strain. However, in order for such small crystallite domains to achieve the the minimum energy, a second order strain exerting on the crystallite domains requires the largest number of organic lattice sites to be commensurate with substrate lattice sites, and thus to form structures with a optimal shape and of course a well defined orientation relationship between the organic crystal lattices and substrate lattices. It was reported that in some cases, the newly formed small crystallites could slide on the wetting layer in a specific direction and act as nucleation centers to form highly ordered chains with uniform orientation.[1,9-15]

Interestingly, in a biological environment, inorganic crystalline materials reversely emerge from inside of organic matrices under normal and pathological conditions.[16-18] A well-known but very complicated process is biomineralization, a biological process during which regulated inorganic crystals are formed naturally by organisms to fulfill functional purposes. Common functions of mineralized biological materials include skeletal support, such as in the bones of vertebrates and the spicules of marine organisms, protection of soft tissues, such as in the shells of mollusks and eggs or the carapaces of

43

crustaceans, and food grinding, such as in the teeth of many vertebrates and invertebrates. [18-23] Natural biomineralization process is complicated and sophisticated because it occurs in the extracellular matrix (ECM) with lots of macromolecules involved including proteins, glycoproteins, proteoglycans, lipid assemblies and polysaccharides.[18,24-28] But the primary regulation of the mineral crystals comes from proteins like collagens and bound noncollagenous proteins (NCPs).[29-31] Inorganic mineral crystals and proteins might recognize each other by multiple cooperative interactions since both of them are of intrinsically repetitive structured surfaces: inorganic crystals have the basic building lattices while proteins have the linear sequence of amino acid residues in the polypeptide chain. At a high level of recognition, the regularly repeating inorganic crystal lattice might be matched by the repeating sequence along the protein backbone while the charged protein side-chain groups spaced at the correct distance along the backbone are complementary to the reversely charged lattice positions on one crystal surface.[18,32-34]

Proteins involved in biomineralization are assumed to have dual functions based on the mineral crystal-protein recognition. The presence of proteins adsorbed on specific surfaces can slow down the growth of mineral crystals in the directions perpendicular to the adsorbing surface, which can definitely result in anisotropic growth of mineral crystals and the final regulated macroscopic crystal morphologies.[18,35-40] On the other hand, it has been shown that recognition between protein and mineral crystal surfaces on a certain crystal plane may also result in oriented crystal nucleation since such proteins in the extracellular matrix (ECM) might stabilize crystal nuclei on the specific recognized

44

surfaces and could facilitate their transition to stable crystals.[18,41-50] From this perspective, the same protein could act as both a specific growth inhibitor and a nucleation template based on the mineral crystal-protein recognition during the biomineralization process.

However, in this chapter, our main concern is neither molecular organic materials epitaxially growing on substrates by ultrahigh vacuum process of organic molecular beam deposition, nor the biomineralization processes. Our top priority here is the quasiepitaxial growth of ordered protein arrays on inorganic substrates under physiological conditions.

From the discussion about organic molecular quasiepitaxial growth above, we understand there are two dominant factors for this process: the bond energy between organic molecules and the substrate, and the crystal lattice matching between organic molecular crystals and the substrate. Different from the biomineralization process, where proteins, the big organic molecules, must have strong bond energy with specific sites of inorganic substrates, however, the quasiepitaxial growth process of proteins on inorganic substrates is not working that way, which means it is unnecessary, or even unreasonable, for a protein to have such strong and specific interactions with a substrate.[1,18] And thus it might not be that hard to find substrates with appropriate binding energy. As we mentioned, during a quasiepitaxial growth process, a surface organic molecule could translationally move on the substrate lattices without a significant change in energy. And in fact, during organic molecular beam deposition in ultrahigh vacuum, the incident molecules have sufficient thermal energy after deposition to arrange themselves into their minimum energy configuration.[1] For a protein absorbed on a substrate under

45

physiological conditions, if the protein has an intermediate binding energy with a substrate, which means although the protein is not immobilized on the substrate by specific recognition with sites on the substrate, it does align with the substrate lattices and will not go back into solution around, the entropic forces driven by solvent molecules will translationally move the protein on the substrate lattices and temporarily arrange it into one of its minimum energy configurations.

For the other factor, the crystal lattice matching between protein crystals and the substrate, normally the lattice constants of protein crystals and inorganic substrates are not quite in the same length scale, which makes such quasiepitaxial growth of protein crystals very rare. Nevertheless, researchers did use epitaxial growth of proteins on different mineral substrates to purify proteins, control their morphologies, and obtain preferential crystal-growth orientation.[51-63] Moreover, in 2004, Muller and coworkers found that *in vitro* Type I collagen monomers self-assembled into ultrathin but highly anisotropic microribbons (protofibrils) with uniform orientation coating the entire mica surface under physiological conditions.[64] Unfortunately, from then, they have been claiming that when they used protein solution to flush the mica substrate, a so called 'hydrodynamic flow' was created and introduced protein monomers to align with the flow direction and thus form such ultrathin microribbons with uniform orientation on the mica surface.[64-67] Based on our subsequent work, we propose that in Muller's work the patterned ultrathin collagen microribbons on the mica surface were probably a classic example of the quasiepitaxial growth of proteins on inorganic crystal surface. So, we strongly believe that quasiepitaxial growth of proteins on suitable inorganic substrates

could happen, and that in the future the quasiepitaxial growth of proteins on inorganic substrates could be definitely explained by some theoretical models that were applied to the quasiepitaxial growth of organic molecular crystals process by ultrahigh vacuum process of organic molecular beam deposition. In order to further confirm our supposition, in our work, we also used Type I collagen monomers as the protein for quasiepitaxial growth of fibrils on different substrates under physiological conditions, which is our main motivation to conduct our experiments.

As the most abundant protein in multicellular animals' body, collagens are the most important tensile reinforcing elements. In the extracellular matrix (ECM) of a wide range of vertebrates and invertebrates, collagen fibrils are acting as both solid state regulators for cellular function and scaffolding of the tissue architecture, particularly in large vertebrates.[64-78] Among more than 20 different types of monomers, Type I collagen is the most abundant one found in mammalian organisms and is also one of the species that can self-assemble into fibrils of 67 nm axial periodicity (*D*-banding).[68] Type I collagen monomer consists of three polypeptide chains coiled around each other and thus forms a triple helical main part. And in every single chain of a collagen monomer helix, every three amino acid residues there must be a glycine to induce the final triple-helical structure, and other amino acids present abundantly are most likely to be proline and hydroxyproline.[68-78] Like other types of collagens, Type I collagen monomers are secreted from cells as procollagen first, then after the removal of the *N*-propeptides and *C*-propeptides on procollagen terminal ends by procollagen *N*-proteinase and procollagen *C*-proteinase respectively, tropocollagen can be obtained for further self-

47

assembly into fibrils in the extracellular matrix (ECM).[79,80] The size and shape of the collagen fibrils are important to determine tissues' functions since the hierarchical spatial arrangement of collagen fibrils can dominate the mechanical and physical properties of tissues. In bones and dentins, with the assistance of some noncollagenous proteins (NCPs) tightly bound to the collagen fibers, hydroxyapatite is first nucleated in the gap region of the parallel large fibrils of a high density, and then grows into mineral platelets within the collagen fibrils in a highly organized staggered manner.[68,81,82]

The self-assembly process of collagen and the biomineralization process in tissues has been widely widely investigated by many different methods from both theoretical and experimental approaches.[83] For theoretical approaches, different models to predict the growth of collagen fibrils such as diffusion limited aggregation (DLA) model, segment-fusion model, and helical model were proposed but were limited to making some specific predictions of the shapes and molecular orientations of fibrils.[70,83-85] In the meantime, all kinds of multidisciplinary experimental methods combining molecular biology and instrumental analysis have been applied to explore the collagen fibril self-assembly process and the biomineralization process at different stages both *in vitro* and *in vivo*. For example, enzymology research combining electron microscopy analysis showed that procollagen *N*-proteinase is crucial to forming some bipolar fibrils by selectively removing the *N*-propeptides on *N*-terminal procollagen.[68,86,87] Other *in vivo* genetic approaches like gene knock-out technique and mutagenic technique have obtained lots of achievements on explaining the functions of the noncollagenous proteins (NCPs) during the biomineralization process.[88-92] However, in spite of such efforts,

48

the molecular mechanisms of fibril assembly in the extracellular matrices and the biomineralization in tissues remain poorly understood. In our experiment, the investigation on the quasiepitaxial growth of collagen fibrils will hopefully cast some light on the understanding of the molecular mechanisms of collagen fibril assembly from a very different angle.

While focusing on instrumental analysis, we must recognize that electron microscopy,[68,93,94] X-ray diffraction[95,96] and FTIR (Fourier Transform Infrared) spectroscopy[97,98] have been the main resources in exploring the structure of collagen fibrils and biominerals and their self-assembly and mineralization process over decades. But other techniques such as AFM (atomic force microscopy)[99,100], and optical tweezers [101] can also provide important information from different aspects of the biomineralization of collagen.

Among all of the techniques mentioned above, AFM has been widely applied more recently to solve some biological puzzles due to its advantages[71]: AFM has a really high resolution (angstroms); it can be operated under physiological conditions, which means no need to pretreat samples before imaging; and of course only small amounts of samples are required. Since AFM can be used to touch the nanoworld so precisely and conveniently, many exciting experiments such as imaging and physical modulating a single protein's conformation, stretching and unfolding a individual DNA molecule, and disrupting antibody-antigen bonds have been carried out with AFM. [64-67,72-77,102-106]

Many AFM experiments have also been done to study the self-assembly process of

49

collagen in different biological systems. Early studies involving AFM and collagen were carried out under dry conditions[77,99], but recently, AFM experiments to describe the structure of collagen fibrils were carried out under physiological conditions although still *in vitro*. As we mentioned above, Muller and coworkers reported that collagen monomers self-assembled into ultrathin (cross-sections of around 3nm × 5nm), highly anisotropic microribbons coating the entire substrate, and a high-resolution AFM was applied to characterize and manipulate such microribbons under physiological conditions.[64-67] In their work, they found that the pH of the buffer solution affects the orientation, width, spacing, and assembly of collagen into microribbons and certain electrolyte compositions can influence the 67 nm characteristic D-banding formation on collagen fibrils.

In our experiments, we were trying to carry out a more systematical work on investigating the quasiepitaxial growth of collagen fibrils on different substrates with high resolution AFM under physiological conditions. Both mica and HOPG (Highly Oriented Pyrolytic Graphite) were used as substrates in our experiments. We also tried many different buffers to confirm the influence of certain electrolyte compositions on the formation of fibrils, and specific ions that can form hydroxyapatite were used in our tentative work to provide some insight into our future biomineralization work. Moreover, different concentration of collagen solutions were used to observed how concentration factors could change the quasiepitaxial growth: the height, the width, and the spacing of the assembled collagen fibrils. In addition, long time incubation was applied to observe if more complicated structure could be formed on substrates under specific conditions.

3.2 *Experimental procedures*

Preparation of collagen samples under physiological conditions on two substrates of which one is mica and the other is HOPG (Highly Oriented Pyrolytic Graphite)

All the chemical reagents used were of analytical grade and prepared with ultrapure water (18 MΩ Barnsted Nanopure). 3.0 mg/ml VITROGEN (purified) collagen for cell culture and biochemistry (pH 2.0, dissolved in 0.012 M HCl) was purchased from Cohesion (California, USA) and stored at 4 °C. VITROGEN (purified) collagen is 99.9 % pure collagen which is 95-98 % Type I collagen with the remainder being comprised of type III collagen. For collagen solution preparation there were five different solutions used: 1) a phosphate buffer (pH 7.5) of 8.2 mM NaH_2PO_4, 41.8 mM Na_2HPO_4 and 200 mM NaCl, 2) a phosphate buffer (pH 7.5) of 8.2 mM KH_2PO_4, 41.8 mM K_2HPO_4 and 200 mM KCl, 3) a buffer (pH 7.5) of 50 mM Tris-HCl and 200 mM KCl, 4) a solution (pH 7.5) of 20 mM Ca^{2+} and 200 mM KCl, and 5) a solution (pH 7.5) of 20 mM Ca^{2+} and 200 mM NaCl. The VITROGEN (purified) collagen was first diluted in one of the five buffers (solutions) to a concentration of 30 μg/ml, and then collagen solutions of different concentration were obtained by diluting the 30 μg/ml collagen solution into the same buffer (solution). As substrates, square mica pieces of an average size about 7.0 mm × 7.0 mm (one exception, see details in *'Substrates'* section), and a square HOPG crystal of a fixed size of 1.0 cm × 1.0 cm were used. After being freshly cleaved with an adhesive tape, the mica {001} cleavage plane or HOPG {0001} cleavage plane was flushed with a collagen solution to introduce collagen monomers or initial collagen aggregates on the surface and was left for 15 min with the collagen solution staying on it. After the same surface was rinsed with the one of the three buffers mentioned before (not necessarily the

same buffer used for collagen solution preparation) to remove loosely bound collagen monomers or aggregates, it was then incubated by around 60 μl of that buffer overnight (one exception, see details in 'Incubation time' section). The incubation process was

Step 1: Making monomer solution

Step 2: Introducing collagen monomers to a substrate

Step 3: Incubating monomers with a buffer
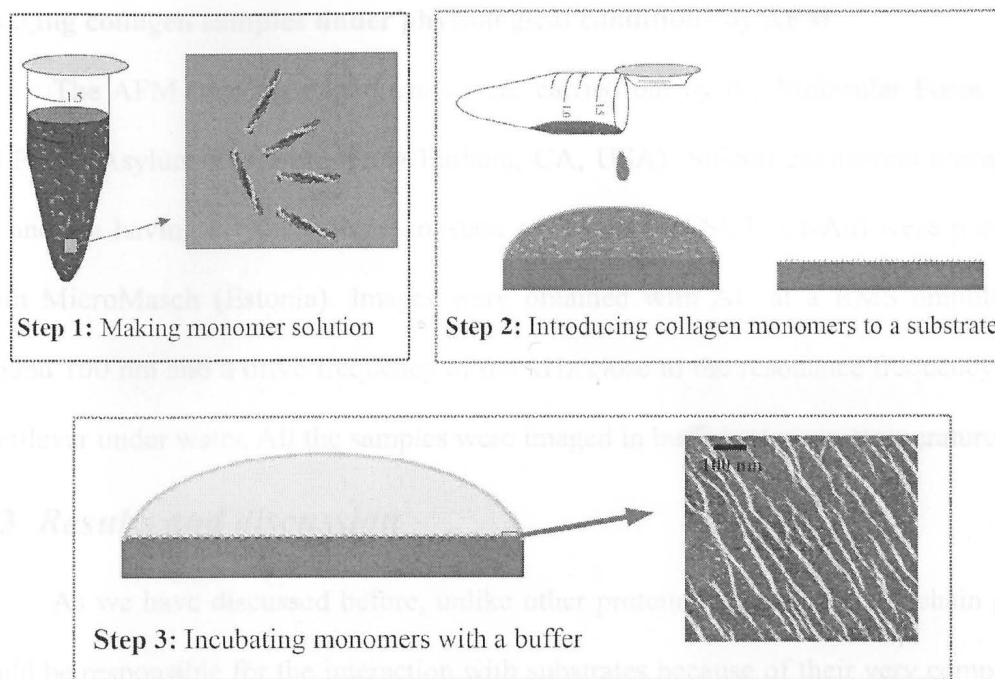
Figure 3.1   Preparation of collagen samples under physiological conditions on a substrate. Step 1, collagen monomers are dissolved into a buffer, but there could be lots of initial collagen aggregates coexisting under the conditions. Step 2, the substrate surface is flushed with the collagen solution to introduce collagen monomers or initial collagen aggregates on the surface. Step 3, the same type of buffer used in step 1, or a totally a new buffer, is used first to rinse the substrate surface to remove loosely bound collagen monomers or aggregates, then to incubate the collagen coated surface to allow the quasiepitaxial growth of fibrils.

carried through in an enclosed plastic dish with ultrapure water drops scattered around to keep the buffered sample surface from drying. The whole procedure is demonstrated in Fig.3.1. All the samples were prepared at room temperature.

Imaging collagen samples under physiological conditions by AFM

The AFM imaging experiments were carried out by the Molecular Force Puller, MFP 3D (Asylum Research, Santa Barbara, CA, USA). Silicon cantilevers coated with Cr and Au having a typical force constant of 0.1 N/m (CSC37/Cr-Au) were purchased from MicroMasch (Estonia). Images were obtained with AC at a RMS amplitude of around 100 nm and a drive frequency of 6.8 kHz close to the resonance frequency of the cantilever under water. All the samples were imaged in buffers at room temperature.

3.3 *Results and discussion*

As we have discussed before, unlike other proteins where only side-chain groups could be responsible for the interaction with substrates because of their very complicated tertiary structures, the long Type I collagen monomer has a quite simple main right-handed helix part formed from winding three a-chains with left-handed helical conformation, which have the repeating amino acid sequence $(Gly-X-Y)_n$, where X and Y are frequently the imino acids proline and hydroxyproline, respectively.[68-82] Fig.3.2 shows a modeled collagen monomer made of three identical chains with the same repeating sequence $(Gly-Pro-Hyp)_n$ based on the X-ray diffraction results.[107,108] One can clearly find that in Fig.3.2 A three left-handed individual helices are supercoiled in a right-handed manner with a periodic supercoil pitch around 85.5 Å. However, the

morphology of the molecule's surface seems to be more influenced by the left-handed individual helical chain. Every single helical chain with a helix rise of 8.6 Å per triplet also causes such a rough periodicity for all of the zigzag arranged side-chain groups on the whole molecule, and results in the meridional arcs of regular spacing along the long axis of the molecule as shown in Fig.3.2 B.[107] Consequently, as shown in Fig.3.2 C, for such a molecule lying on a substrate, in the contact area the exposed sequences, i.e.
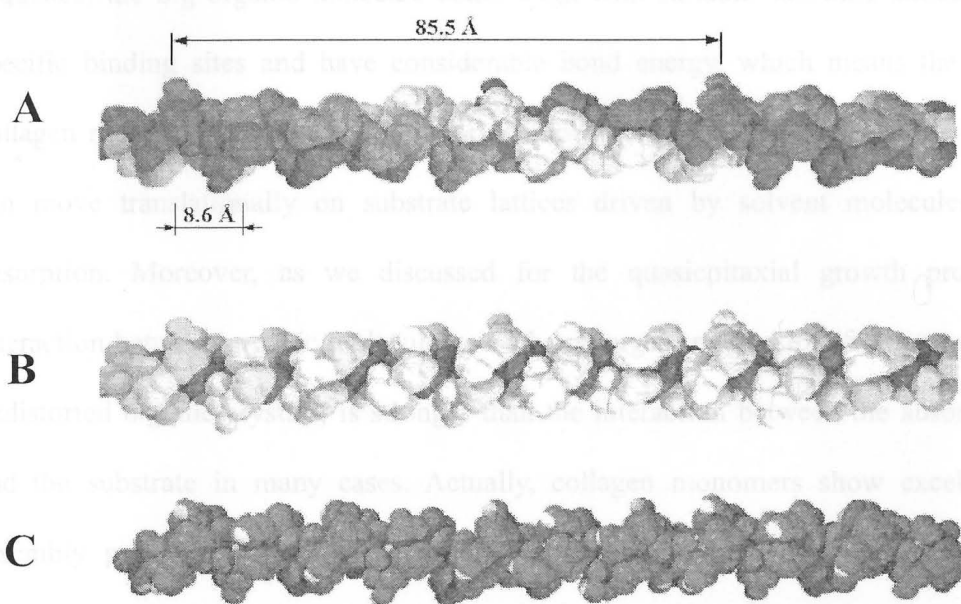
Figure 3.2   Collagen monomer model (Gly-Pro-Hyp)$_n$. Three left-handed helical polypeptide chains with a helix rise of 8.6 Å per triplet are wound by each other into a right-handed super triple helix with a periodic supercoil pitch around 85.5 Å. A, the model is colored by chains (blue, red and yellow). B, the same model is colored by residues: Gly (blue), Pro (yellow) and Hyp (white). C, the same model is colored by atoms: C (dark), O (red), N (blue), H (white).[107,108]

the nonpolar prolyl (Pro) and polar hydroxyprolyl (Hyp) residues, are also distributed in a zigzag way with a distance around 9 Å along the long axis of the helix, although these residues do not have the same backbone.[107]

Because such a periodicity around 9 Å is on the same length scale of most inorganic lattices, if one sequence electrostatically matches the inorganic substrate lattice, so do the others. Even for a real Type I collagen momoner without such regular repeating sequence, the big organic molecule could align with suitable substrate lattices without specific binding sites and have considerable bond energy, which means the absorbed collagen monomers could have some orientations defined by substrate lattices, but they can move translationally on substrate lattices driven by solvent molecules without desorption. Moreover, as we discussed for the quasiepitaxial growth process, the interaction between organic molecules, which are largely responsible for determining the undistorted organic crystals, is stronger than the interaction between the absorbed layer and the substrate in many cases. Actually, collagen monomers show excellent self-assembly properties. From those aspects, collagen monomers are super models for research in protein fibril quasiepitaxial growth on inorganic substrates and the final turnout morphologies could be many well defined self-assembled fibrils aligned with substrate lattices in azimuthal orders, which is quite coincident with Muller's results[64-65].

However, several issues about collagen fibril quasiepitaxial growth have to be pointed out here. Firstly, compared to the organic molecular crystal growth process in ultrahigh vacuum, the physiological environment for collagen fibril growth and the

55

structures of the fibril by itself are more complicated in our studies. Secondly, for the traditional molecular organic films or crystals quasiepitaxially growing on substrates by ultrahigh vacuum process of organic molecular beam deposition, the lattice mismatch between substrates and organic bulk crystals is relatively small. But in our case, collagen fibrils growing under physiological conditions are of a huge axial periodicity, e.g. the 67 nm D-banding, which is obviously not of the same order as that of the lattice constants of most inorganic substrates. And unlike crystals with specific lattice constants, collagen fibrils can adopt many different structures to fulfill multiple functions *in vivo* due to the monomers' intrinsic properties. So, it is very possible for collagen monomers to be aligned with substrate lattices in azimuthal orders first, and then to grow into fibrils, which is quite different from the quasiepitaxially growing process of small organic molecular crystals. In addition, for organic films or crystals quasiepitaxially growing on substrates in ultrahigh vacuum, the process is under appropriate thermodynamic conditions with continuous evaporant supply from a temperature-controlled oven.[1,9-15] But in our experiment, in order to simplify our tentative investigation, we just introduced the substrate with a thin film of collagen monomers or initial aggregates[93,94] once, and tried to observe how the underlying substrate lattice could influence the fibril assembly process within the film.

In our experiments, we flushed one cleavage plane of the substrate, mica {001} or HOPG {0001}, with collagen solution first to introduce collagen monomers or initial aggregates on the lattice plane, then rinsed the surface to remove the loosely bound molecules or aggregates, and finally incubated the samples in solution to allow collagen

molecules to assemble into fibrils. Since there were no collagen monomers or aggregates in the buffer solution covering the substrate's surface, self-assembly on one lattice plane of the substrate was the only way to fibril formation. We were expecting that once collagen monomers or initial aggregates were covering a substrate, these huge molecules or aggregates could be aligned with azimuthal angles on a certain lattice plane of the substrates first. And since the substrates we used are all, at least in local areas for the quasiepitaxial growth studies, single crystals, hopefully, we will observe that the fibrils thus formed are also aligned with azimuthal angles on a certain lattice planes of the substrates in our experiments.

As we mentioned, several factors that could influence the quasiepitaxial growth of collagen fibrils were taken into account. In our experiment, two substrates, different concentration of collagen solutions, specific ions, and even the time for incubation were investigated to observe how those factors could change the quasiepitaxial growth of collagen fibrils.

3.3.1 Substrates

3.3.1.1 Mica (2M_1 muscovite)

The structure of Mica (2M_1 muscovite)

As a substrate, mica (2M_1 muscovite) was used first in our experiment. Among a huge mica family, mica (2M_1 muscovite) of a composition close to {KAl$_2$(AlSi$_3$O$_{10}$)(OH)$_2$} shows a monoclinic crystal structure with $a = 5.2906$ Å, $b = 9.0080$ Å, $c = 20.0470$ Å, $\beta = 95.757°$.[109-111] All types of mica crystals are constructed by repeating thin layers along the c axis. An adhesive tape can be used to peel layers off to get a perfect basal

57

cleavage, the {001} cleavage plane. The freshly cleaved mica surface is flat at an atomic scale and makes an ideal substrates for SPM experiments. As one of the mica polytypes, the $2M_1$ type mica has a two-layer unit cell within which two adjacent layers was staggered ±120° relatively to each other. So, along the [001] direction, i.e. the c axis, adjacent layers are alternately staggered regularly by angles of +120°, -120°, + 120°. . . .

As shown in Fig.3.3, in each layer of the two-layer $2M_1$ muscovite crystal unit cell,
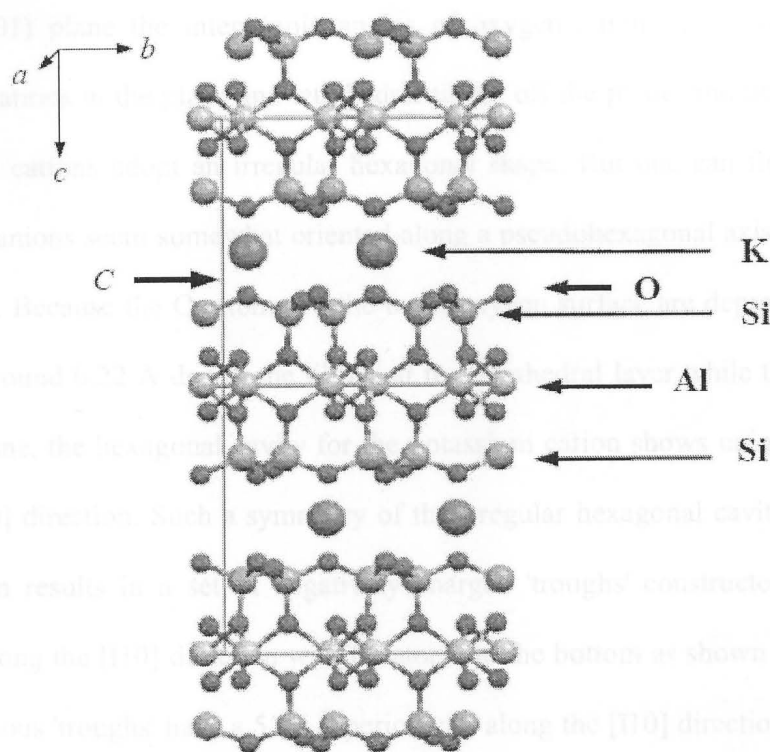
Figure 3.3   The structure of the mica layers around one two-layer unit cell projected along the [100] direction. The vertical line shows the crystal lattice constant c. Within one layer of the two-layer unit cell along the c axis, a central sheet of Al cations in octahedral coordination with oxygen anions and hydroxyl groups is sandwiched by two sheets of Si cations in tetrahedral coordination with oxygen anions. {001} cleavage

58

along the the c axis, a central sheet of Al cations in octahedral coordination with oxygen anions and hydroxyl groups is sandwiched by two sheets of Si cations in tetrahedral coordination with oxygen anions. On the (001) lattice plane, the tetrahedral Si/O sheet gives rise to an oxygen surface that creates interlayer negatively charged cavities for potassium cations. Due to the distortion of the tetrahedral layers, the oxygen anions on the basal plane show a huge deviation from ideal hexagonal arrays. As shown in Fig.3.4 A, on the (001) plane the interatomic angles of oxygen anions are twisted by both tetrahedral rotations in the plane and tetrahedral tilting off the plane, and the cavities for the potassium cations adopt an irregular hexagonal shape. But one can find that these basal oxygen anions seem somewhat oriented along a pseudohexagonal axis, the $[\bar{1}10]$ or $[1\bar{1}0]$ direction. Because the O_d atoms on the basal oxygen surface are depressed into the (001) plane around 0.22 Å due to the tilting of the tetrahedral layer while the others are still in the plane, the hexagonal cavity for the potassium cation shows unique symmetry along the $[\bar{1}10]$ direction. Such a symmetry of the irregular hexagonal cavities along the $[\bar{1}10]$ direction results in a set of negatively charged 'troughs' constructed by oxygen anions also along the $[\bar{1}10]$ direction with O_d atoms in the bottom as shown in Fig.3.4 B. These continuous 'troughs' have a 5.23 Å periodicity along the $[\bar{1}10]$ direction, a radius of curvature around 1.960 Å, and a depth about 0.22 Å, and normally are occupied by potassium cations with the same periodicity along the $[\bar{1}10]$ direction. In a mica ($2M_1$ muscovite) crystal, the interlayer potassium cations are locked by another set of "troughs" almost running along the $[110]$ direction in the $(00\bar{1})$ plane of the upper unit cell due to the $\pm 120°$ two-layer staggering unit cell structure. However, for a freshly {001} cleavage

59
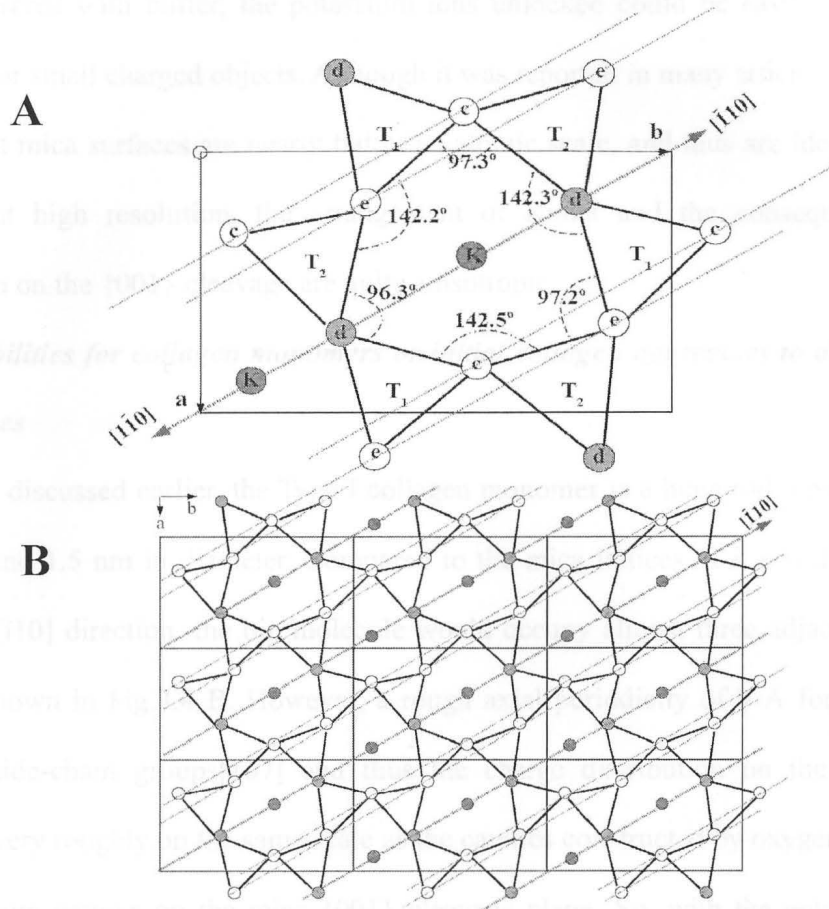
Figure 3.4   The upper tetrahedral sheet of $2M_1$ muscovite projected onto (001). Due to

the distortion of the tetrahedral layers, the oxygen anions on the basal plane show a

huge deviation from the ideal hexagonal arrays. The O_d atoms on the basal oxygen

surface are depressed into the (001) plane around 0.22 Å due to the tilting of the

tetrahedral layer. A: a view around one unit cell on (001). B: a view of about nine

parallel unit cells on (001). A set of negatively charged 'troughs' constructed by

oxygen anions along the [ī10] direction with O_d atoms in the bottom are indicated by

dashed lines and arrows. See details in [109].

60

surface covered with buffer, the potassium ions unlocked could be easily replaced by other ions or small charged objects. Although it was reported in many articles about AFM studies that mica surfaces are nearly flat at an atomic scale, and thus are ideal for AFM scanning at high resolution, the arrangement of atoms and the consequent charge distribution on the {001} cleavage are quite anisotropic.

The possibilities for collagen monomers or initial collagen aggregates to align on the mica lattices

As we discussed earlier, the Type I collagen monomer is a huge rod around 300 nm in length and 1.5 nm in diameter. Compared to the mica lattices, if it could align itself along the [$\bar{1}$10] direction, the big molecule would occupy almost three adjacent parallel 'troughs' shown in Fig.3.4 B. However, a rough axial periodicity of 9 Å for the zigzag arranged side-chain groups[107] and thus the charge distribution on the molecule's surface is very roughly on the same scale as the cavities constructed by oxygen anions for the potassium cations on the mica {001} cleavage plane. So, with the entropic forces driven by solvent molecules, Type I collagen monomer could find the most preferred directions to align itself on the mica {001} cleavage plane so as to maintain its minimum energy configuration.

Since in Fig.3.4 A it seems that the mica (001) plane has one rough symmetry along the [$\bar{1}$10] direction or (110) plane, we have to ask, if the molecule has one preferred direction along the mica surface, is it possible there is another 'degenerate' direction due to the symmetry? First, let's consider the [$\bar{1}$10] direction and its perpendicular direction. Because of the symmetry, if one collagen monomer finds that it can turn into the

minimum energy configuration by aligning itself with any one of the two directions, any other direction could not also be an energy minimum. But how about other directions besides the $[\bar{1}10]$ direction and its perpendicular direction? It seems that other directions come in 'degenerate' pairs because of the symmetry. But as a matter of fact, that is not the truth. If we take a closer look at Fig.3.4 A, we can find that neither the $[\bar{1}10]$ axis nor (110) plane is the element of symmetry for O_c and O_c atoms. Even if we roughly assume O_c and O_c atoms are identical in every way, we will not find a 'degenerate' direction for collagen monomers on the mica {001} cleavage plane either.

Let's take an example: on the mica {001} cleavage plane, imagine one monomer is lying along the [110] direction while the other is lying along the $[\bar{1}00]$ direction. One can find these two directions are actually images with each other roughly along the (110) plane. It might not be so surprising for one to find the lattices of oxygen anions arranged along the [110] direction and the $[\bar{1}00]$ direction on the mica {001} cleavage plane are chiral images along the (110) plane. But on the other hand, for a natural Type I collagen monomer, from N-terminal to C-terminal, the repeating amino acid sequences $(Gly-X-Y)_n$ are not really regular, which makes the long rod without any element of symmetry although the helical part of the monomer has a rough, in many cases just local, axial periodicity of 9 Å for the zigzag arranged side-chain groups. And compared to mica lattices, the huge collagen monomer can not be considered as an infinite thin charged string because the distribution of side-chain groups and charges on transverse sections (relative to the c axis) can not be ignored. So, one monomer can feel very different morphologies and electric fields of the mica lattice while comparing lying along the

[110] direction or [$\bar{1}$00] direction.

One conclusion can be deduced from the discussion, that if one collagen monomer finds one most preferred direction on the mica {001} cleavage plane, this is also the only one most preferred direction for all other identical collagen monomers. One thing has to be pointed out here, even for a freshly made and very diluted collagen solution under physiological conditions, there could be lots of small initial collagen aggregates like *4D*-staggered dimers and trimers. If the collagen monomers could find their most preferred direction on the mica {001} cleavage plane, the initial collagen aggregates could also behave the same way.

Before the real experimental analysis, two issues have to be stressed again based on the previous discussion: firstly, it is very possible for Type I collagen monomers or small initial aggregates to be electrostatically absorbed on the mica surface; and secondly, if Type I collagen monomers or aggregates can be absorbed on the mica surface, there will be only one most preferable direction to align themselves on the underlying lattice. So here, we might imagine that all of the monomers and small initial aggregates after some time on the mica {001} cleavage plane under buffer are aligned in the same direction due to the minimum energy configurations, but solvent molecules can drive them to translationally slide in random directions. Once one monomer or aggregate bumps into another, they will not separate from each other again due to the entropic forces and self-assembly properties of the collagen monomers, and thus big aggregates or small protofibrils are formed gradually. While growing to some critical size, protofibrils stay still on the surface because they can not be easily driven around by solvent molecules, but

63

they can accept smaller aggregates and even monomers. Finally, monomers and small aggregates will disappear, and the mica surface will be covered only by lots of protofibrils with the same orientation, which is probably a reasonable explanation for the patterned ultrathin collagen microribbons on the mica surface in Muller's work[64-66] and is definitely an expectation for our work on the mica.

The first trial on the mica lattices

In our first run, the sample prepared under phosphate buffer on a mica surface was imaged. This sample was made by the 0.3 μg/ml collagen solution in a phosphate buffer (pH 7.5) of 8.2 mM NaH_2PO_4, 41.8 mM Na_2HPO_4 and 200 mM NaCl, but then rinsed and buffered by a phosphate buffer (pH 7.5) of 8.2 mM KH_2PO_4, 41.8 mM K_2HPO_4 and 200 mM KCl overnight (see the experimental procedures). Fig.3.5 represents the topographic image on the mica {001} cleavage plane. One can find in Fig.3.5 lots of protofibrils with a well-defined pattern formed on an area of 3.0 μm × 3.0 μm. The protofibrils were aligned generally parallel to each other, which was probably directed by quasiepitaxial growth of collagen fibrils on the mica surface as we discussed. Such long protofibrils have a length ranging from one to several micrometers. On average, every single fibril is around 60 nm in width while 1.5 nm in height; and average spacing between two neighbour fibrils is around 400 nm. AFM images over a larger area of 20 μm × 20 μm on different spots (images not shown) demonstrated a consistent pattern over whole mica surface. In Fig.3.5, one might also notice that the mica surface is not really flat and the background curvature could up to 5 nm. There were several potential reasons that could account for this problem. For one thing, the substrate, a mica disk around 7.0

64
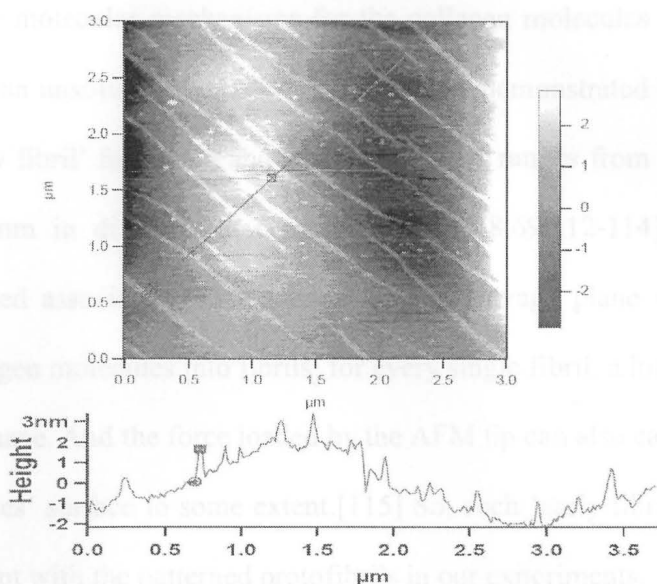
Figure 3.5 AFM topographic image (AC Mode) of patterned collagen protofibrils quasiepitaxially grown on mica under phosphate buffer, with the line-scan height spectrum shown below. The scan area is 3.0 μm × 3.0 μm. The mica surface was flushed by 0.3 μg/ml collagen monomers dissolved in 50 mM phosphate buffer (200 mM Na$^+$, pH 7.5) and incubated by 50 mM phosphate buffer (200 mM K$^+$, pH 7.5) overnight.

mm × 7.0 mm was fixed by an double-side adhesive tape on a glass silde with a drop of buffer covering on it. When the AFM cantilever was dipped into the buffer on the mica surface during the imaging, the mica surface was experiencing huge surface tension from the buffer while the AFM cantilever was moving around and the mica surface was bent subsequently. Another aspect could be piezo drift of the tip movement. The piezo can drift to some extent, so that it has to retract to compensate for the drift. As a consequence, it could appear that the surface is curved.

65

So far, the molecular mechanisms for the collagen molecules to self-assemble into fibrils are still an unsolved puzzle. But many studies demonstrated that there is an initial stage for 'early fibril' formation and such protofibrils ranges from 1 to 20 μm in length and 3 to 15 nm in diameter at cross-section.[64,68,69,112-114] Since in our case, surface-mediated association on the mica {001} cleavage plane was the only way to assemble collagen molecules into fibrils, for every single fibril, a long flat strip should be a reasonable shape. And the force loaded by the AFM tip can also cause fibrils to collapse on the substrates' surface to some extent.[115] So, such 'early fibrils' reported before is really coincident with the patterned protofibrils in our experiments.

More proof about the quasiepitaxial growth of collagen fibrils on the mica lattices

From our experiment above, we obtained very nice patterned protofibrils similar to the patterned ultrathin collagen microribbons in Muller's work. In order to prove that there is no such a thing as the 'hydrodynamic flow', and that the patterned protofibrils are absolutely a result of the quasiepitaxial growth of collagen fibrils on the mica lattices, we designed a new experiment to further confirm it. This time a square-shape mica of a size about 7.0 mm × 18.0 mm was used. After being cleaved with an adhesive tape to get a fresh and complete surface, the middle part of the mica surface was pasted with two layers of adhesive tape strips, so that the whole mica surface was divided into two parts with a similar area around 7.0 mm × 7.0 mm. As shown in Fig.3.6 A, we flushed the two areas with collagen solution in two perpendicular directions to introduce collagen molecules on the surface. We used collagen solution of higher concentration here, 6.0 μg/ml collagen solution in the phosphate buffer (pH 7.5) of 8.2 mM NaH_2PO_4, 41.8 mM

66

Na$_2$HPO$_4$ and 200 mM NaCl, to make patterned protofibrils more easily found because collagen solution of higher concentration can make a more crowded pattern (to be discussed in the 'Concentration of collagen' section). Then the two surfaces were rinsed and buffered by a phosphate buffer (pH 7.5) of 8.2 mM KH$_2$PO$_4$, 41.8 mM K$_2$HPO$_4$ and 200 mM KCl overnight.
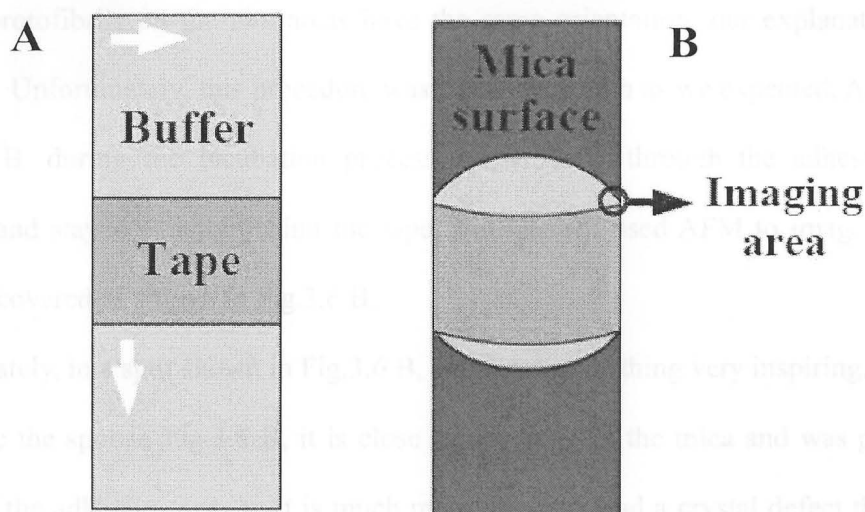
Figure 3.6   After being cleaved with an adhesive tape, the middle part of the square-shape mica of a size about 7.0 mm × 18.0 mm was pasted with two layers of the adhesive tape strips, so that the whole mica surface was divided into two parts with a close area around 7.0 mm × 7.0 mm. The two divided areas were flushed by collagen solution in two perpendicular directions indicated by white arrows as shown in A. Then the two areas were separately rinsed and incubated by the same buffer. However, as shown in B, during the incubation process, buffer went through the adhesive tape somehow, and stayed exactly behind the tape. A spot with buffer covered shown in B was imaged by AFM anyway.

We assumed that the two divided mica surfaces originating from one complete surface should have identical lattice orientation. So, if there is a so-called 'hydrodynamic flow', we will find that the pattern protofibrils on the two surfaces should have perpendicular orientations because we flushed the two areas with collagen solution in two perpendicular directions to induce two perpendicular 'hydrodynamic flow'. And if the patterned protofibrils on the two areas have the same orientation, our explanation will stand valid. Unfortunately, this procedure was not so thorough as we expected. As shown in Fig.3.6 B, during the incubation process, buffer went through the adhesive tape somehow, and stayed exactly behind the tape. But we still used AFM to image an area that buffer covered as shown in Fig.3.6 B.

Fortunately, in a spot shown in Fig.3.6 B, we found something very inspiring. In such an area like the spot in Fig.3.6 B, it is close to one edge of the mica and was probably touched by the adhesive tape, so it is much more likely to find a crystal defect there. As shown in Fig.3.7 A, the background shows the mica crystal defects very clearly and it seems that at least four basal planes (I, II, III, IV), of which plane II is a long strip, were exposed. Surprisingly, we found that in each of three areas (I, II, and IV), the protofibrils were aligned parallel to each other, and the orientations of protofibrils on three different cleavage planes are either the same or antiparallel. However, although the patterned protofibrils have one uniform orientation all over area III, the orientation of the patterned protofibrils in that area is quite different from the protofibrils in area I, II, and IV. And the two orientations of the protofibrils are generally 60° or 120° relative to each other on the basal plane.

68

The experiment above is quite meaningful and much better than what we expected. First of all, it absolutely disproved the 'hydrodynamic flow' proposed by Muller and coworkers. When the mica surface was flushed by collagen solution, the 'hydrodynamic flow' swept an area around 7.0 mm × 7.0 mm. But in Fig.3.7 A, the scanned area was
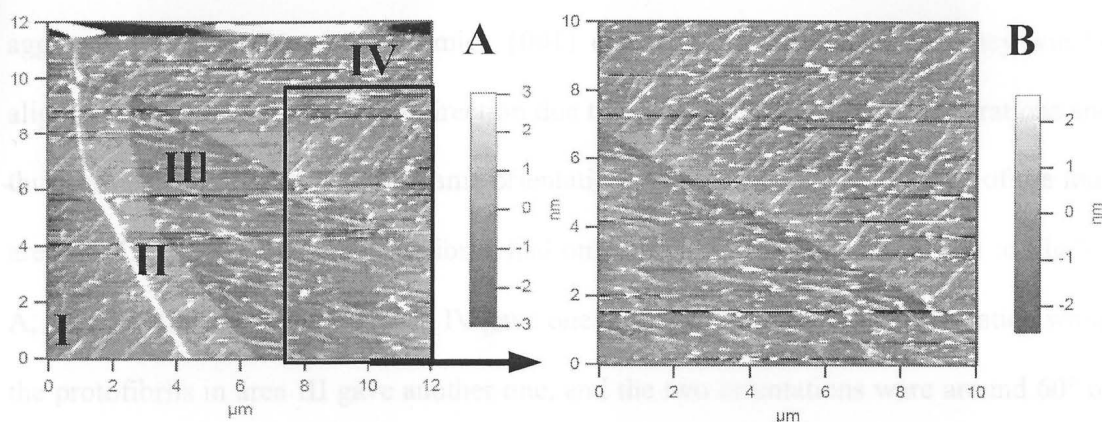
Figure 3.7 AFM topographic image (AC Mode) of patterned collagen protofibrils quasiepitaxially grown in the spot shown in Fig.3.6 B. A: the background shows the mica crystal deficiency very clearly. At least four basal planes (I, П, Ш, IV), of which plane П is a long strip, can be seen. In each of the three areas (I, П, and IV), the protofibrils were parallelly aligned to each other, and the orientations of protofibrils on three different cleavage planes are almost the same. In area III, although the patterned protofibrils have one uniform orientation, the orientation is quite different from the protofibrils in area I, П, and IV. And the two orientations of the protofibrils are generally around 120° relative to each other on the basal plan. B: the border of area Ш and area IV is very clearly in the AFM image. It seems that the quasiepitaxial growth of collagen fibrils was very sensitive to the orientation of the mica {001} cleavage plane.

69

of a size only around 12 μm $\times$ 12 μm and it is absolutely impossible to create two 'hydrodynamic flows' with different directions in such a small area. Most importantly, only Fig.3.7 A by itself can perfectly explain the quasiepitaxial growth of collagen fibrils on the mica {001} cleavage plane as we proposed: once the monomers or initial aggregates are introduced to one mica {001} cleavage plane under buffer, they will be aligned in the same and the only direction due to the minimum energy configurations and thus formed protofibrils with the same orientation. As a matter of fact, in each of the four areas (I, II, III and IV), the protofibrils had only one uniform orientation. But in Fig.3.7 A, the protofibrils in area I, II, and IV gave one or maybe an antiparallel orientation while the protofibrils in area III gave another one, and the two orientations were around 60° or 120° relative to each other on the basal plane.

As we mentioned, the $2M_1$ type mica has a two-layer unit cell within which two adjacent layers were staggered ±120° relative to each other along the c axis. So, for a mica single crystal, when we use the adhesive tape to get a freshly cleaved surface, we have equal probability to get new cleavage planes with two different staggering angles. In our case, the cleavage planes of the area I, II, and IV probably have the same staggering angle while the cleavage plane of the area III has the other. Since collagen monomers or initial aggregates introduced to one mica {001} cleavage plane under buffer would be probably aligned in the only most preferred direction to form the protofibrils with the same orientation, the protofibrils on two cleavage {001} planes in the same single crystal of mica no matter how far the two layers are apart along the c axis, should either have the same orientation, or have an staggered orientation angle of 120°. So, what we found in

70

Fig.3.7 A were probably telling us that the protofibrils in area I, II, and IV gave the same orientation and were staggered 120° relative to the protofibrils in area III on the basal plane. So far, our experiment gives our proposal, the quasiepitaxial growth of collagen fibrils on the mica {001} cleavage plane, a very convincing proof.

Although the protofibrils on area III are differently oriented from the patterned protofibrils in the other areas, the borders of area III are quite clean and no overlapping of the protofibrils on the border areas could be clearly seen. Fig.3.7 B shows the border of area III and area IV very clearly. It seems that the quasiepitaxial growth of collagen fibrils was very sensitive to the orientation of the mica {001} cleavage plane. Another point from the experimental results here is that the protofibril patterns were found far from any defects or step edges and hence were not nucleating from the defects.

However, one thing has to be pointed out, that the patterned protofibrils from the flushing of 6.0 μg/ml collagen solution in Fig.3.7 were not more crowded than that from 0.3 μg/ml collagen solution shown in Fig.3.5. Our explanation is that the defects on the mica's surface in the imaging area in Fig.3.6 B could be created by the adhesive tape when the buffer were going through the tape because that spot was too close to the mica' edge and the adhesive tape; and the collagen monomers or initial aggregates in that area were probably brought by buffer from other areas around.

3.3.1.2 HOPG (Highly Oriented Pyrolytic Graphite)

In the following experiment, a graphite substrate, HOPG (Highly Oriented Pyrolytic Graphite) instead of mica was used to investigate if the new substrate could also mediate the quasiepitaxial growth of collagen fibrils on its surface.

71

The structure of HOPG and the possibilities for collagen monomers or initial aggregates to be absorbed on the mica lattices

HOPG (Highly Oriented Pyrolytic Graphite) can be simply described as a periodic stack of two-dimensional (*a-b* plane) graphene sheets or layers along the *c* axis, although it can be considered as a 'supermosaic' structure, consisting of graphene crystallites grouped to form blocks or layers highly oriented along the *c* axis. The term, HOPG, came from the measurement of how highly ordered the HOPG is along the *c* axis. The lower the mosaic spread, the more highly Oriented is the HOPG, resulting in a cleaved surface with less steps. But as stacked graphene sheets, HOPG exhibits the typical properties of graphite. Each sheet of HOPG consists of equilateral hexagonal lattice of carbon bonded by strong σ bonding (sp^2) and parallel π-orbital electrons oriented along the *c* axis in the *a-b* plane. Each graphene sheet is so weakly bonded to its neighboring sheets by interlayer interaction forces that the graphene sheets can easily slide against each other and peel off easily. In the HOPG *a-b* plane, each atom is equally surrounded by six nearest neighbors with an in-plane nearest carbon-carbon distance of 0.142 nm and thus the equilateral hexagonal lattices are formed with a lattice constant of 2.46 Å.[116-121]

Like mica, HOPG has a perfect basal cleavage, allowing crystals to be split into very thin sheets. The freshly cleaved HOPG {0001} plane is also clean and of a local atomic smoothness. As a type of graphite, one intrinsic property of HOPG is its highly hydrophobic, actually nonpolar, basal plane compared to mica's highly charged surface. Moreover, unlike mica, because HOPG is a 'supermosaic' structure and the thin basal plane sheets of HOPG are super fragile, when HOPG is cleaved using adhesive tape to

expose a fresh {0001} plane, steps are usually generated , which can result in local height difference on the basal plane.[122,123] Fig.3.8 A represents the AFM topographic image of a clean HOPG surface on a $10.0\ \mu$m $\times$ $10.0\ \mu$m area: the steps generated on the surface are obvious and the height difference between two adjacent graphene sheets are up to 4 nm. On the basal plane of a single crystal sheet, the surface is very flat, and such flat crystal sheets are very long but around 1 μm in width, and the orientation of the crystal sheets are roughly uniform, which was probably mainly caused by the tape peeling process.

Since we have known a lot about HOPG, our next concern is the possibility for Type I collagen monomers to be absorbed on the HOPG surface. Taking a look again at Fig.3.2 B, one will find that the nonpolar prolyl residues are also zigzag arranged along the c axis with a rough periodicity of 9 Å. Because our system is under buffer, the collagen monomers or initial aggregates could be simply pushed by entropic forces to the nonpolar HOPG surface without any specific charge complementation. It seems although it is very possible for collagen monomers or aggregates to be attracted on HOPG {0001} plane, a specific alignment with the underlying lattices might be a problem. In addition, even if one collagen monomer could align itself along a specific azimuthal angle of the underlying HOPG lattices in order to get the minimum energy configuration, the equilateral hexagonal lattices of HOPG {0001} plane can provide other, at least five, possibly eleven, 'degenerate' alignment directions for collagen monomers. If we consider the 'supermosaic' basal planes of HOPG, there could be more alignment directions. So, according to our expectation, collagen monomers or small initial aggregates could be

73

absorbed on HOPG {0001} plane to form bigger aggregates or even fibrils, but the resulting morphologies could be lots of big aggregates or protofibrils with different orientations under amorphous growth.

The experiment on the HOPG surface

To investigate if the HOPG substrate could induce patterned protofibril formation, in the following experiment we prepared the sample the same way as that in Fig.3.5: 0.3 μg/ml collagen solution in the phosphate buffer (pH 7.5) of 8.2 mM NaH_2PO_4, 41.8 mM Na_2HPO_4 and 200 mM NaCl flushed the HOPG surface, then rinsed and buffered by a phosphate buffer (pH 7.5) of 8.2 mM KH_2PO_4, 41.8 mM K_2HPO_4 and 200 mM KCl overnight. In Fig.3.8 B, C, D, we found a big difference on the topographic image of the collagen fibril pattern compared to that on the mica surface (see Fig.3.5). AFM images over a larger area of 10 μm $\times$ 10 μm on different local spots (Fig.3.8 B,C,D) demonstrated three main representative patterns on the whole HOPG surface. In Fig.3.8 B, beautiful porous collagen structures with pores of different sizes covered most of the HOPG surface while the exposed areas in the pores were almost empty substrate surface. The diameter of the pores on the area ranged from 100 nm to 3 μm while the height of the porous structure above the substrate ranged from 2 nm to 20 nm. In another spot of the substrate a similar topographic image to that of Fig.3.8 B is shown in Fig.3.8 C1: a porous structure of collagen fibrils was also found, but the pores in Fig.3.8 C1 are generally bigger and more uniform, and most of them had a diameter above 1 μm; the height of the the porous structure above the substrate ranged from 20 nm to 50 nm; exposed areas in the pores were not empty and it seems there were lots of particles
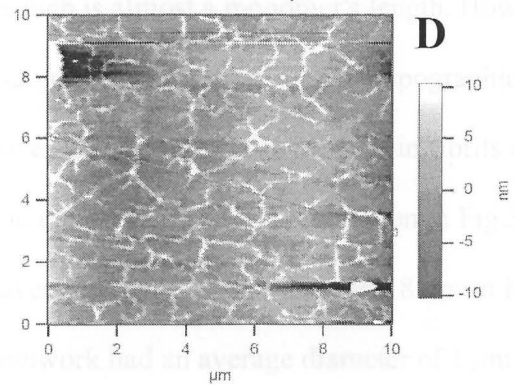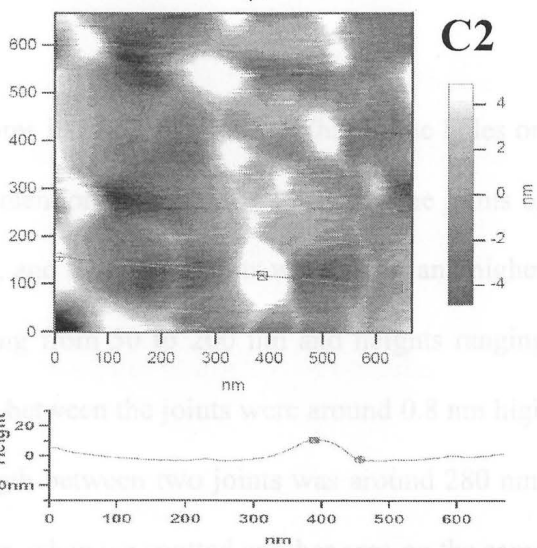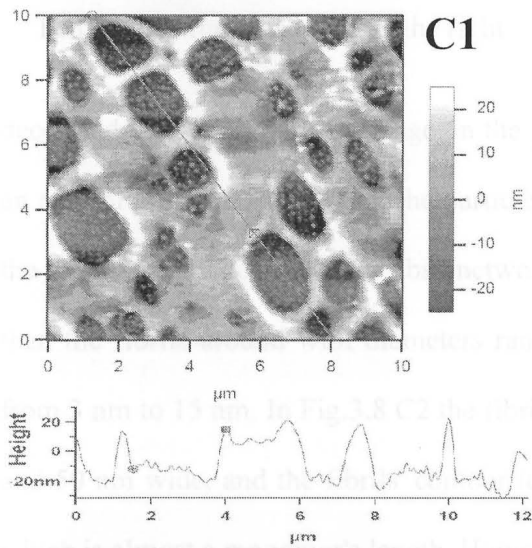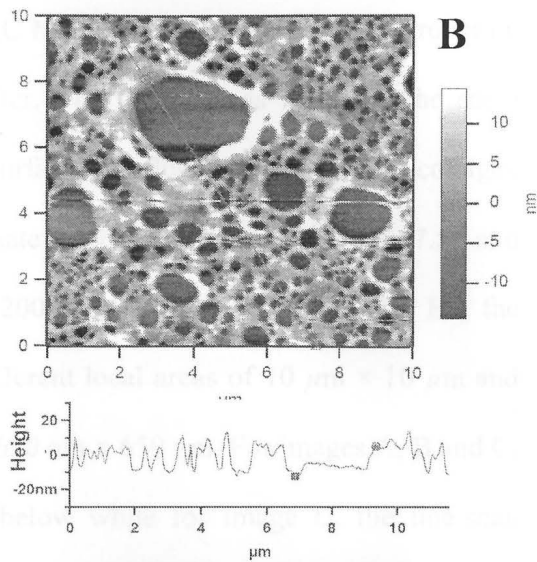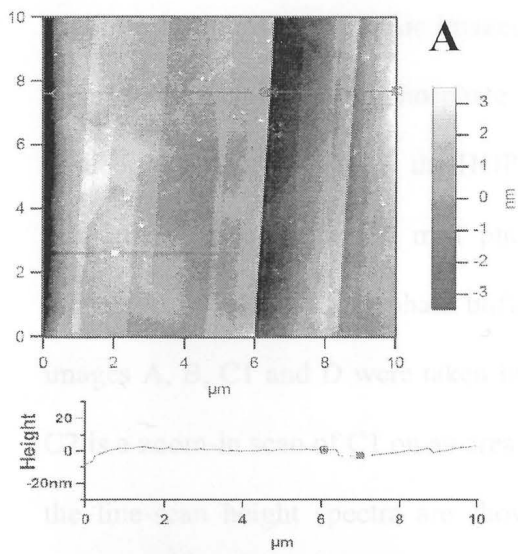
Figure 3.8 AFM topographic images (AC Mode) of collagen structures grown on the HOPG surface under phosphate buffer. The sample was made by the same procedure as that in Fig.3.5: the HOPG surface was flushed by 0.3 μg/ml collagen monomers dissolved in 50 mM phosphate buffer (200 mM Na$^+$, pH 7.5) and incubated by 50 mM phosphate buffer (200 mM K$^+$, pH 7.5) overnight. But the images A, B, C1 and D were taken in different local areas of 10 μm × 10 μm and C2 is a zoom-in scan of C1 on an area of 650 nm × 650 nm. For images A, B and C, the line-scan height spectra are shown below while for image D, the line-scan height spectrum is shown on the right.

decorated inside. A zoom-in image on the pores in Fig.3.8 C2 shows that in the holes on an area of 0.65 μm × 0.65 μm, the particles mentioned above were actually the joints of the highly overlinked collagen fibril network, and the round joints were wider and higher than the fibrils around with diameters ranging from 50 to 200 nm and heights ranging from 3 nm to 15 nm. In Fig.3.8 C2 the fibrils between the joints were around 0.8 nm high and 50 nm wide, and the fibrils' contour length between two joints was around 280 nm, which is almost a monomer's length. However, when we spotted another area on the same sample, a totally different topographic image was obtained in Fig.3.8 D: highly overlinked networks made of thin fibrils on an area of 10 μm × 10 μm could be seen, but no clear round and big joints seen in Fig.3.8 C2 were found. The fibrils in Fig.3.8 D were averagely 250 nm in width and 8 nm in height, and the rings formed by the fibrils in the network had an average diameter of 1 μm.

From the results above, it is obvious that the nonpolar HOPG surface can attract a lot more collagen monomers or initial aggregates compared to mica if we just compare the heights of the collagen structures on the two substrates. Although it is not really surprising to see very strong entropic forces (also called hydrophobic forces) based interaction between the nonpolar HOPG surface and the collagen molecules or aggregates, there is no proof that collagen monomers or fibrils could align themselves along a specific azimuthal angle of the underlying HOPG lattices, which is absolutely within our expectation. From our experimental results about HOPG, we might conclude that collagen protofibrils can not quasiepitaxially grow on the HOPG {0001} cleavage plane, so from now on, we are not going to consider HOPG as the substrate for quasiepitaxial growth of collagen protofibrils again. All of the rest experiments discussed here on the quasiepitaxial growth of collagen protofibrils will use only the mica {001} cleavage plane.

3.3.2 Factors that can influence the pattern of the protofibrils on mica

3.3.2.1 Concentration of collagen solution

Higher concentration can result in a more crowded pattern

Two collagen solutions of which one is 1.0 μg/ml and the other is 3.0 μg/ml made by the same procedure discussed above were investigated in our studies. The mica {001} cleavage plane was flushed by collagen solution in Na^+ containing phosphate buffer, then was rinsed and buffered by K^+ containing phosphate buffer overnight. While comparing Fig.3.5 (0.3 μg/ml collagen solution), Fig.3.9 A (1.0 μg/ml collagen solution), and Fig.3.9 B (3.0 μg/ml collagen solution), one can find the difference among the three samples. In

77

Fig.3.9 A, the sample made by 1.0 μg/ml collagen solution shows that generally parallel aligned protofibrils form a well-defined pattern already seen in Fig.3.5; fibrils are normally longer than those in Fig.3.5 and some of them are longer than 3 μm; fibrils are averagely 50 nm in width while 0.8 nm in height; and average spacing between two neighbour fibrils is around 188 nm, which is much smaller than 400 nm in Fig.3.5. Within our expectation, in Fig.3.9 B (3.0 μg/ml collagen) a well-defined pattern was formed by even longer fibrils than those in Fig.3.9 A, but with a narrower average
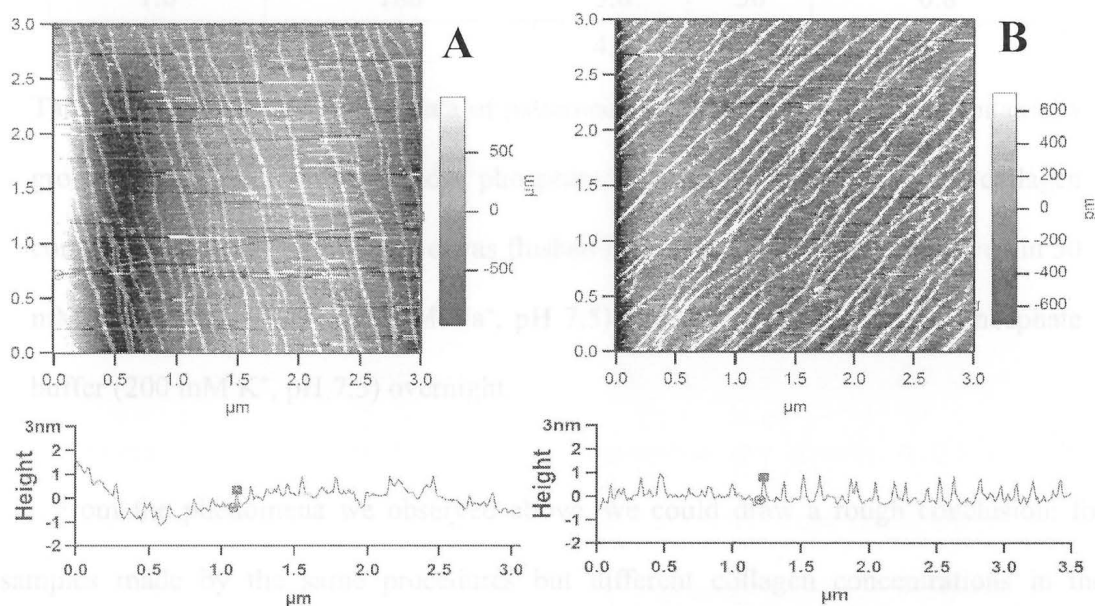
Figure 3.9   AFM topographic images (AC Mode) of patterned collagen protofibrils quasiepitaxially grown on the mica surface under phosphate buffer with the line-scan height spectra shown below. The scan area is always 3.0 μm × 3.0 μm. The mica surface was flushed by collagen monomers dissolved in 50 mM phosphate buffer (200 mM Na$^+$, pH 7.5) and incubated by 50 mM phosphate buffer (200 mM K$^+$, pH 7.5) overnight. A: 1.0 μg/ml collagen solution; B: 3.0 μg/ml collagen solution.

spacing of around 180 nm between two neighbour fibrils than that in Fig.3.9 A. For a single fibril in Fig.3.9 B, the average width is around 60 nm while the height is around 1 nm. In Table 3.1, the main data of the protofibrils grown on mica surface from three solutions of different concentration are listed.

Concentration (μg/ml)	Average neighbour fibrils Distance (nm)	Average Length (nm)	Average Width (nm)	Average Height (nm)
0.3	400	2.5	60	1.5
1.0	188	3.0	50	0.8
3.0	180	4.5	60	1.0

Table 3.1   AFM topographic data of patterned collagen protofibrils quasiepitaxially grown on the mica surface under phosphate buffer with different initial collagen concentrations. The mica surface was flushed by collagen monomers dissolved in 50 mM phosphate buffer (200 mM Na^+, pH 7.5) and incubated by 50 mM phosphate buffer (200 mM K^+, pH 7.5) overnight.

From the phenomena we observed above, we could draw a rough conclusion: for samples made by the same procedures but different collagen concentrations in the solution, more concentrated solution can result in a more crowded pattern, i.e. in a same size of area, more fibrils could be found and the average spacing between two neighbour fibrils is smaller; while the fibril growth in width and height from 0.3 μg/ml collagen solution to 3.0 μg/ml collagen solution was not so obvious.

Possible regulation during the quasiepitaxial growth of ultrathin collagen protofibrils by the mica lattices

79

Our experiment above provoked two questions, of which one is why the collagen protofibrils are ultrathin, and the other is why the protofibril growth in width and height did not change much in spite of the concentration of collagen solution compared to the growth in length.

For the first question, it was reported that during the early stage of collagen fibril assembly, the N-telopeptide of Type I tropocollagen is critical for the formation of the polarized $4D$-staggered dimers, while the C-telopeptide has a dual role, promoting a transverse accretion of linear aggregates as well as participating in the formation of the early linear assemblies.[68,124] So, from a statistical view, the linear association of collagen molecules or initial microaggregates are more preferred, which might be a reason for the formation of ultrathin protofibrils in our experiment.

However, this explanation above becomes ambiguous when we try to answer the second question about the regulation on the protofibril growth in width and height during the quasiepitaxial growth. In the following discussion, our answer to the protofibril growth pattern in width and height could explain the linear shape of ultrathin collagen structure even better, which makes the first explanation (statitical view from telo-peptides) less valid.

Although we mentioned before that collagen monomers or initial aggregates coated on the mica {001} cleavage plane under buffer are aligned in one direction due to the anisotropic regulation of the mica lattices, and solvent molecules can drive them to form bigger aggregates till the protofibrils growing to a critical size can stay still on the surface, it was just our rough model.

80

In 1993, in order to answer some puzzling observations about strained epitaxial layers during that time, Tersoff and Tromp theoretically proved that strained epitaxial layers tend initially to grow as dislocation-free crystalline islands on a wetting layer, but at a large critical size, under the control from both the thermodynamics (energy minimum) and the kinetics (continuous deposition), the islands will adopt a long thin shape of a constant height with high aspect ratios (length/height and length/width) along specific crystal directions of the substrate, which allows better elastic relaxation of the island's stress, although even at high island densities, island-island interactions have only slight effect on the formation of such long thin shape structures.[3] Something has to be straightened out here to avoid any confusion since we mentioned before, due to the lattice mismatch between substrates and organic bulk crystals, the strain developed in the absorbed organic film could be released by forming small crystallite domains. While in Tersoff and Tromp's work, their main concern was a second order strain, the strain exerting on the crystallite domains, causes the crystallite domains to achieve their minimum energy by adopting an optimal shape (surface area/volume ratio) and a well defined orientation with the substrate lattices.

Almost a decade later, many researchers reported that during the fabrication of organic semiconductor thin films of PSP (para-sexiphenyl, $C_{36}H_{26}$) on a series of substrates like mica {001}, TiO_2 {110}, and KCl {001} cleavage planes in the ultrahigh vacuum environment by organic molecular beam deposition, small individual crystallites (islands) spontaneously arrange into parallel running, high-aspect ratio chains with a length in the micrometer range, but with a height around 20 nm and a width around 50

81

nm.[9-15] The new discoveries[9-15] could enrich Tersoff and Tromp's model[3] by considering the effect of island density and island-island interactions on the formation of the long thin shape structures.

Researchers proposed the following mechanism of spontaneous rearrangement of PSP crystallites into high-aspect ratio crystal chains on mica. A strain induced locally by the crystallites into the wetting layer (in Tersoff and Tromp's model, an island under stress also exerts a force on the surface, which could even elastically distort the substrate [3]) leads to the formation of a linear defect in the wetting layer whose orientation is related to the substrate geometry. This defect stimulates the mobile crystallites to touch each other in a specific direction. The rearrangement process is performed by the mobile crystallites as nucleation centers for the chain. This proposal was supported by AFM, which recognized the individual crystallites, and by electron diffraction and TEM measurements, which revealed the existence of three differently oriented PSP domains within one chain.

During those experiments, researchers also found that there are different growth stages of PSP films on mica while the organic molecular beam deposition continues. At the beginning, only islands (crystallites) are formed. When the islands (crystallites) get saturated, short crystal chains emerge. Then, more chains are gradually formed while the existing chains keep growing rapidly in length but slowly in width and hight, but crystallites still coexist. Finally, isolated crystallites disappear and the long term growth morphology consists only of chains.[9-15] From the results of the formation of PSP crystal chains, it seems that the density of the crystallites and island-island interactions

have huge influence on the formation of such long thin crystal chains.

In our understanding, during the formation of PSP crystal chains[9-15], a linear defect in the wetting layer induced locally by the crystallites could be totally an entropy effect. First, let's assume that the organic molecules in the wetting layer are also mobile to some extent on the mica surface, although they prefer to be absorbed on the mica lattices rather than be incorporated into crystallites. So, in order to increase their entropy and hence lower their free energy, such mobile molecules in the wetting layer are eager to push crystallites together, which is also called the depletion interaction.[125] Based on the assumption, one possible explanation is that for any single mobile molecule in the wetting layer, the movement in every direction on the mica surface is differently regulated by the anisotropic mica lattices so that all the isolated crystallites will similarly experience intense 'bumping' by the mobile molecules only from specific directions (very possibly along the linear defect), which will definitely result in the high-aspect ratio chains, and the weak bumping from other directions, which could contribute to the slow growth in width. But another possible explanation is that even if the mobile molecules in the wetting layer randomly move in every direction without any preference on the mica surface and thus all the isolated crystallites can experience the bumping of almost the same intensity from all directions by the mobile molecules, the movement of a crystallite on the wetting layer is differently regulated by the anisotropic mica lattices, which allows the crystallite to move more easily only along specific directions (very possibly along the linear defect) and thus to form the high-aspect ratio chains.

As a matter of fact, our two explanations are quite similar because the regulation

from the substrate plays an important role in the formation of the high-aspect ratio chains. And it is very possible that in the real situation, the substrate could regulate both the mobile molecules in the wetting layer and the mobile crystallites on the wetting layer. Our understanding was supported by two facts. Firstly, the surface morphology quite depends on the substrate temperature. With the same deposition rate and the same deposition time, at low temperature (352 K) only small crystallites were available on the mica surface, while at higher temperature (523 K), only the high-aspect ratio chains existed. And of course, at a temperature between 352 K and 523 K, both small crystallites and the high-aspect ratio chains coexisted.[10] Obviously, this fact proved that from a view of the thermodynamics, the formation of the high-aspect ratio is dominated by the entropy effect because the enthalpy effect can not contribute too much to the free energy change of the system. The other fact came from the results of the annealing process of such a system. When the growth was interrupted at a point where both small crystallites and the high-aspect ratio chains coexisted, and the sample was kept at the deposition temperature for a certain time, a further reduction of the strain can be achieved by incorporation of surrounding crystallites into the already-existing chains to just increase the length of the chains.[15] Undoubtedly, the annealing process is a concrete proof of the role of the mobile molecules in the wetting layer played during the formation of the chains from a view of the microscopic kinetics.

Back to our case, the ultrathin protofibrils without noticeable growth in height and width are really coincident with Tersoff and Tromp's predictions and others' experiments on high-aspect ratio chains of PSP in the ultrahigh vacuum environment. Although our

system under buffer seems quite complicated, our understanding to the formation of the highly oriented collagen ultrathin protofibrils could get simplified if we can borrow some ideas from the formation of the high-aspect ratio chains of PSP in the ultrahigh vacuum environment. In our system under buffer, the whole mica surface was covered by solvent molecules or ions and there could be one or more layers of solvent molecules or ions absorbed on the mica surface. When collagen monomers or initial collagen aggregates were introduced to the mica surface, a strain was surely induced locally into the absorbed solvent layer. Actually, in our case, the strain is not only limited to the absorbed solvent layer but also includes the surface of collagen monomers or initial collagen aggregates. So, in order to increase their entropy and hence lower their free energy, the solvent molecules or ions will push collagen monomers or initial collagen aggregates from all directions almost in three dimensions (assuming no push from the contact area between collagen and mica surface). However, the highly oriented collagen monomers or initial aggregates will experience very different resistance when they translationally move in different directions on the anisotropic mica lattices, which allows the monomers or initial aggregates to move more easily along specific directions (very possibly along the orientation of the monomers or initial aggregates) and thus to form the highly oriented collagen ultrathin protofibrils with relatively slow growth in height and width.

Here, we believe that it is quite reasonable to take the collagen monomers or initial aggregates as the equivalent of the dislocation-free crystallites on the PSP wetting layer in the ultrahigh vacuum environment. A Type I collagen monomer has a huge size (300 nm in length and 1.5 nm in diameter) similar to that of the PSP crystallites (typical 100 ×

50×20 nm^3 in size). Moreover, the PSP crystal chains are spontaneously formed by rearrangement of the individual crystallites as entities, and thus even differently oriented PSP crystallites could be incorporated into one chain. As a matter of fact, collagen monomers can self-assemble into nonpolar or bipolar fibrils both *in vivo* and *in vitro* depending on the orientation of the collagen monomers inside the fibrils. In addition, some collagen self-assembly models also predicted the existence of the fusion of relatively small fibril segments (initial aggregates) into bigger fibrils during the fibrogenesis process.[85] So, the rearrangement of the individual PSP crystallites into crystal chain is a really good comparison to the quasiepitaxial growth of ultrathin collagen protofibrils in our experiment.

It seems that from the discussion we had so far, two most important factors for the quasiepitaxial growth of ultrathin collagen protofibrils on the mica surface can be abstracted. Firstly, collagen monomers or small initial aggregates can be electrostatically absorbed and be likely aligned in only the one most preferable direction on the underlying mica lattice. Secondly, the movement of collagen monomers or small initial aggregates is strictly regulated by the anisotropic mica lattices, which makes the crystallite move more easily only along specific directions (possibly along the orientation of the monomers or initial aggregates). Interestingly, the two questions, of which one is why the collagen protofibrils are ultrathin, and the other is why the protofibril growth in width and height did not change much in spite of the concentration of collagen solution, are possible to be answered if we take just the two factors stressed above into account. One has to ask what roles are expected for the monomers' inherent self-assembly

86

properties to play here? Actually, in Muller's work, they pointed out that the monomers' self-assembly properties could allow the fine adjustment within a collagen fibril by arranging the monomers to reach the most preferred interaction sites, which resulted in the D-banding fibrils in their work. In the next section, we will use different kinds of buffer or solution to further confirm their opinions.

Although more evidence is required for our explanations on the ultrathin protofibrils without noticeable growth in height and width, we have to admit that with the regulation of mica {001} cleavage lattices, the formation of the protofibrils happened on some specific scale because when collagen solution with higher concentration was used, more crowded protofibrils were formed, instead of thicker protofibrils. It is reported that the early collagen fibrillogenesis process in extracellular environment *in vivo* always happens on some critical scale to form fibrils of generally the same dimension. Many observations demonstrated that the fibril formation process is not a simple process like that: a single monomer fuses into a fibril already existed to get a bigger one.[93,126-128] Early studies on three dimensional structure analysis suggested that microfibrils of 4 nm in diameter and with 67 nm D-banding are probably the basic structural unit of collagen fibrils on a larger scale than monomers; they consist of five quarter-staggered monomers and are loosely entwined with each other for internal readjustment to form full fibrils.[93,128] But later studies identified that the assembly of *4D*-staggered dimers and trimers into oligomers might be crucial for the early stages of fibril formation.[129-131] More interestingly, Goh and coworkers found that by the addition of α_1-acid glycoprotein to an acidified solution of monomeric collagen, fibrous long spacing (FLS) collagen fibrils,

which are collagen fibrils of the periodicity greater than the 67-nm periodicity of native collagen and have been found *in vivo* associated with a number of pathological conditions, were formed *in vitro* at a pH around 4 and showed protrusions spaced at around 270 nm. Because neither the $0D$-stagger model (end-on-end packing of collagen monomers) nor $4D$-staggered pentamer could account for such FLS fibrils, they proposed a new mechanism for the formation of FLS collagen fibrils based on their AFM results. Firstly, collagen monomers are staggered into microfibrils possibly with α_1-acid glycoprotein in the overlap region. Then protofibrils of 3-7 nm in diameter and 1-2 μm in length with protrusions at 270 nm periodicity are formed from such microfibrils and are very possible to be the structural units for the final FLS collagen fibrils. Finally, by the merging, the entangling, and the tight packing of the protofibrils, the FLS collagen fibrils are formed with protrusions spaced evenly at 270 nm.[100,132] So, based on our and others' discoveries, we strongly believe that our investigation on the quasiepitaxial growth of ultrathin protofibrils on anisotropical mica {001} cleavage plane will hopefully provide insight into the mechanism of collagen assembly in the anisotropic extracellular environment *in vivo*.

3.3.2.2 Buffers or Solutions

As we discussed in the previous section, the regulation by the mica lattices could be dominant during the quasiepitaxial growth of protofibrils, but we are really curious about to what extent the monomers' inherent self-assembly properties can influence the pattern of the protofibrils on the mica surface. So, in the following experiments, different buffers or solutions for making the collagen suspension and for incubating samples on substrates

88

were used to investigate this question. The method mentioned before on the mica surface was to make collagen solution in phosphate buffer containing Na^+ ions, then incubate samples by phosphate buffer containing K^+ ions overnight. However, different buffers could make a big difference on the protofibril pattern formed on the substrate. Based on our proposal of quasiepitaxial growth of collagen fibrils, the interaction between collagen monomers and mica surface is the complementary electrostatic match between the protein's zigzag distributed charged residues and the mica {001} charged lattices. Obviously, a buffer with different ions could change the charge distribution on the mica {001} cleavage plane somehow such as replacing the cations in the negatively charged 'troughs'. Moreover, it was reported that different ions *in vitro* could accelerate or inhibit the fibrillogenesis process by influencing the charged side chains of collagen monomers and by competing the hydrogen bonding sites with water molecules.[93,133,134] Since the charge distribution of the mica {001} cleavage plane, the charge distribution of the collagen monomers, and the self-assembly properties of collagen monomers could be drastically changed when different buffers are used, undoubtedly, the quasiepitaxial growth of collagen fibrils would be also influenced to some extent.

Making collagen solution and incubating samples with the same buffer

In this experiment, we first tried to use the same buffer to make collagen solution and to incubate samples on the mica surface. In Fig.3.10 A, the sample was made by 30 μg/ml collagen solution in the phosphate buffer (pH 7.5) of 8.2 mM KH_2PO_4, 41.8 mM K_2HPO_4 and 200 mM KCl, and was incubated by the same buffer overnight. From the topographic image, we can find that lots of protofibrils were interwoven with each other, but they also

89

show a general orientation. Such fibrils are around 150 nm in width and 1 nm in height.

We also prepared a sample made by 0.3 μg/ml collagen solution. Although nothing could

be found on that sample (image not shown), it is really consistent with our opinion about

the concentration of collagen solution discussed above. Another point is that it seems that

for a specific quasiepitaxial growth of collagen protofibrils, there is a critical

concentration of collagen solution to form such patterned protofibrils. However, in
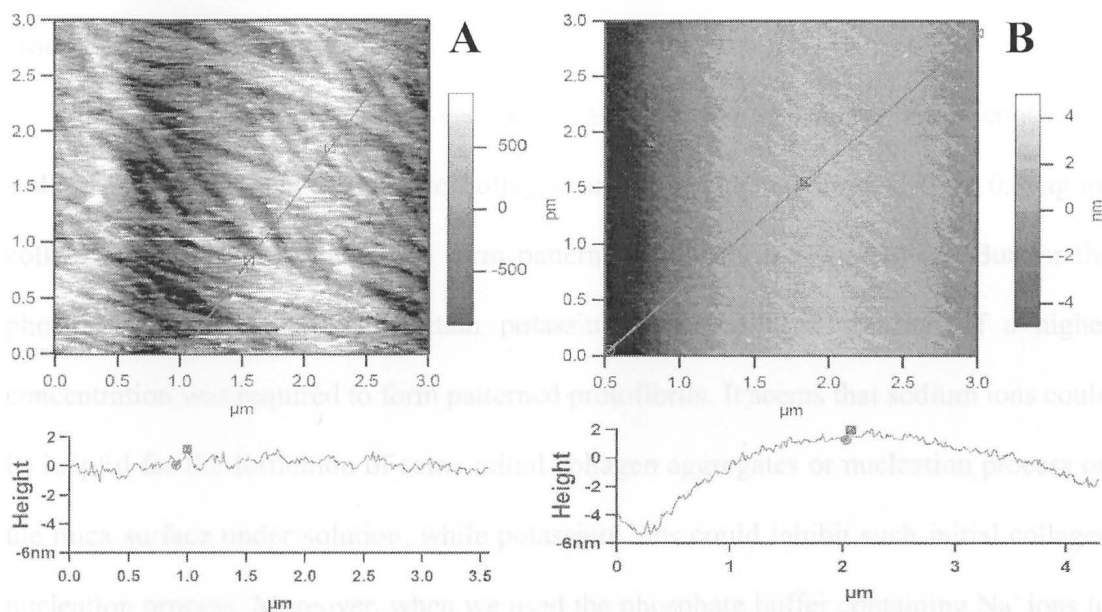
Figure 3.10 AFM topographic images (AC Mode) of patterned collagen protofibrils

quasiepitaxially grown on the mica surface under phosphate buffer with the line-scan

height spectra shown below. The scan area is always 3.0 μm × 3.0 μm. The mica

surface was flushed by collagen monomers in 50 mM phosphate buffer and

incubated by the same buffer overnight. A: 30 μg/ml collagen in 50 mM phosphate

buffer (200 mM K$^+$, pH 7.5); B: 0.3 μg/ml collagen in 50 mM phosphate buffer (200

mM Na$^+$, pH 7.5).

Fig.3.10 B for the sample made by 0.3 μg/ml collagen solution in the phosphate buffer (pH 7.5) of 8.2 mM NaH$_2$PO$_4$, 41.8 mM Na$_2$HPO$_4$ and 200 mM NaCl, and incubated by the same buffer overnight, one can find a very fuzzy morphology of bundled protofibrils on a scanned mica surface around 3.0 μm × 3.0 μm. But the overall orientation of the big protofibrils in Fig.3.10 B is still quite clear. The protofibril clusters in Fig.3.10 B are around 0.7 nm in height and 80 nm in width, and the spacing between these groupings is around 300 nm.

From the results above, one can find that when the phosphate buffer containing sodium ions was used to dissolve collagen and to incubate samples, only 0.3 μg/ml collagen solution was required to form patterned protofibrils (Fig.3.10 B). But for the phosphate buffer containing contain potassium ions, collagen solution of a higher concentration was required to form patterned protofibrils. It seems that sodium ions could be helpful for the formation of some initial collagen aggregates or nucleation process on the mica surface under solution, while potassium ions could inhibit such initial collagen nucleation process. Moreover, when we used the phosphate buffer containing Na$^+$ ions to make collagen solution, but the phosphate buffer containing contain K$^+$ ions to incubate samples, even with the collagen solution of a low concentration of 0.3 μg/ml, a beautiful pattern with distinct protofibrils was formed everywhere on the whole mica surface. This result probably showed us that the initial aggregates formed on the mica surface under the phosphate buffer containing Na$^+$ ions could act as the main nucleation centers for the protofibrils, while during the incubation by the phosphate buffer containing K$^+$ ions, the main process could be the adding the collagen monomers or small aggregates to the

91

already existing nucleation centers due to potassium ions' inhibition of the initial collagen nucleation process. So, from this perspective, potassium ions could be really crucial for the longer and thicker fibrils' formation although they might inhibit the initial collagen nucleation process on the mica surface under solution. As a matter of fact, in Muller's work, they also found potassium ions are crucial to the formation of D-banding ultrathin protofibrils. Muller and coworkers proposed that if the interaction between collagen monomers is too strong, the collagen monomers could assemble randomly by any available interaction sites and thus result in a loss of the characteristic fibril periodicity, the D-banding; however, if the interaction is appropriate, the monomers within a fibril could adjust themselves to pursue the most preferred sites, probably the periodic interaction sites, to form the fibrils with D-banding.[64] Because they believed that potassium ions could inhibit the collagen fibrillogenesis somehow, and thus allow the monomers within a fibril to find periodic interaction sites to form the D-banding fibrils. [64] Unfortunately, in all of our experiments, we could not find convincing proof about D-banding fibrils, which is probably due to the low resolution of our imaging under fluid.

Tris-HCl buffer

It is reported that Tris-HCl, glucose, and arginine can interfere with the collagen fibrillogenesis process.[126,132] So, in the following experiment, a Tris-HCl buffer for sample incubation was applied to further the investigation on the influence of buffer on the quasiepitaxial growth of collagen fibrils. But collagen was still dissolved in the phosphate buffer (pH 7.5) of 8.2 mM NaH_2PO_4, 41.8 mM Na_2HPO_4 and 200 mM NaCl because based on our previous experiments, it seems that enough collagen initial

aggregates could be introduced on the mica surface if collagen solution containing sodium ions was used. After flushing by the collagen solution, the samples were incubated by the buffer (pH 7.5) containing 50 mM Tris-HCl and 200 mM KCl overnight. A sample made by 0.3 μg/ml collagen solution was imaged then: in Fig.3.11 A, ultrathin protofibrils were crowded on a 3.0 μm × 3.0 μm scanned area but they were generally aligned to one direction. Although it is hard to tell the length of such ultrathin fibrils, they are around 0.5 nm in height and 60 nm in width. If we compare Fig.3.11 A to
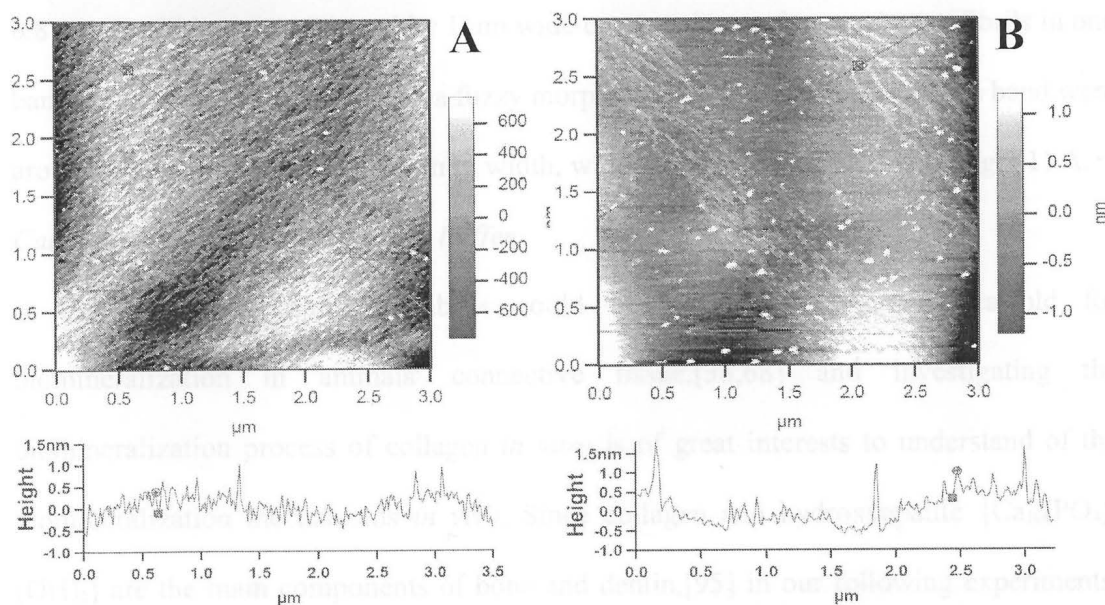
Figure 3.11   AFM topographic images (AC Mode) of patterned collagen protofibrils quasiepitaxially grown on the mica surface under Tris-HCl buffer with the line-scan height spectra shown below. The scan area is always 3.0 μm × 3.0 μm. The mica surface was flushed by collagen monomers in 50 mM phosphate buffer (200 mM Na⁺, pH 7.5) and incubated by 50 mM Tris-HCl buffer (200 mM K⁺, pH 7.5) overnight. A: 0.3 μg/ml collagen solution; B: 0.1 μg/ml collagen solution.

Fig.3.5 because the difference between the two samples was just the conjugate acid-base pairs in the two buffer systems, we can find that Tris-HCl could inhibit the later association of the initial aggregates on the mica surface after the initial collagen nucleation process was done on the mica surface in the phosphate buffer containing sodium ions. Since the 0.3 μg/ml collagen solution used above seems too concentrated for the Tris-HCl system, a sample made by 0.1 μg/ml collagen solution in sodium containing phosphate buffer was used instead. In Fig.3.11 B, parallel protofibril bands of 0.8 μm in width were separated by 1 μm wide empty mica surface; and protofibrils in one band were close enough and gave a fuzzy morphology. The small fibrils in one band were around 0.6 nm in height and 60 nm in width, which is very similar to that in Fig.3.11 A.

Calcium solution and Phosphate buffer

As we know, collagen fibrils could be the most important scaffold for biomineralization in animals' connective tissue,[38,68] and investigating the biomineralization process of collagen *in vitro* is of great interests to understand of the biomineralization mechanisms *in vivo*. Since collagen and hydroxyapatite $\{Ca_{10}(PO_4)_6 (OH)_2\}$ are the main components of bone and dentin,[95] in our following experiments, calcium ions were used to investigate their influence on fibrils' formation.

In our first trial, the mica surface was flushed by 0.3 μg/ml collagen solution containing 20 mM Ca^{2+} and 200 mM NaCl (pH 7.5) and then was rinsed and incubated by a solution containing 20 mM Ca^{2+} and 200 mM KCl (pH 7.5) overnight. In Fig.3.12 A, on a large area of 10.0 μm $\times$ 10.0 μm, the sample made by 0.3 μg/ml collagen solution gave many short and near symmetrical protofibrils with the thickest part in the middle

and paraboloidal pointed tip in the ends. Actually, the aligned protofibrils here were of different sizes ranging from 100 nm to 5 μm in length, but they almost maintained the same shape. The height for all of the protofibrils was almost around 0.5 nm, but the width ranged from several to 300 nm, while the spacing between such fibrils was around 1 μm. If we compare the results with those of Fig.3.5, the difference in morphologies could arise from several possible reasons: from the density of the protofibrils, it seems that a
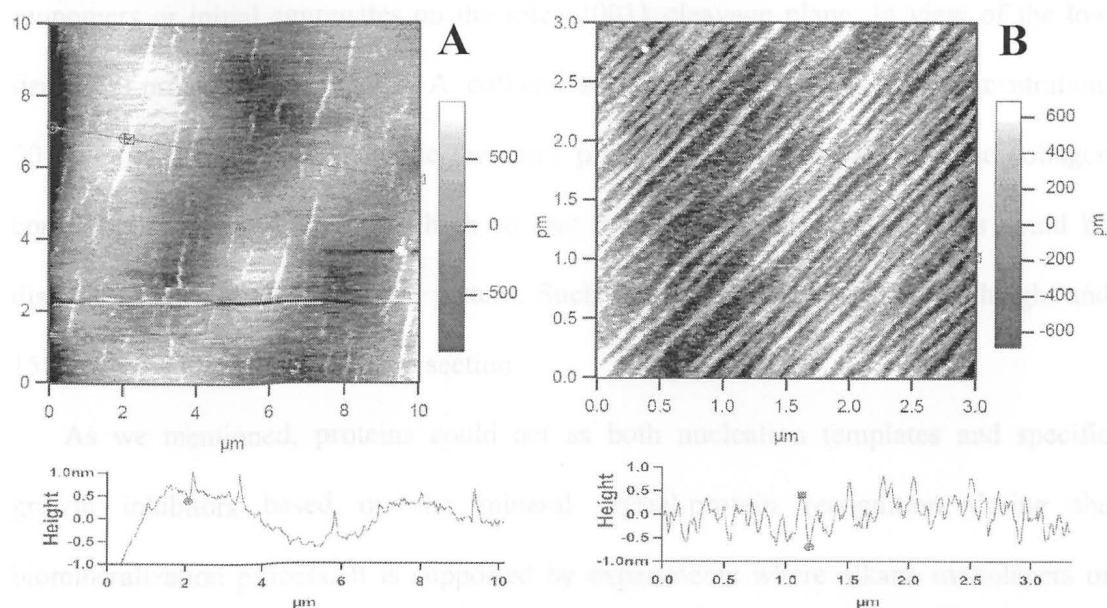
Figure 3.12 AFM topographic images (AC Mode) of patterned collagen protofibrils quasiepitaxially grown on the mica surface under solution with the line-scan height spectra shown below. The mica surface was flushed by collagen monomers in 20 mM Ca^{2+} solution (200 mM Na^+, pH 7.5) and incubated by 20 mM Ca^{2+} solution (200 mM K^+, pH 7.5) overnight. A: 0.3 μg/ml collagen solution and a scan area of 10 μm × 10 μm; B: 30 μg/ml collagen solution and a scan area of 3.0 μm × 3.0 μm.

stable pH in phosphate buffer could be preferred for the nucleation of fibril formation, and that calcium ions could influence the charge distribution on the mica {001} cleavage plane by replacing the cations in the negatively charged 'troughs' and thus decrease the absorption amount of collagen molecules on the mica surface; but from the width of the formed protofibrils, it seems that calcium ions could prohibit the nucleation of fibril formation, but be helpful for the surface-mediated association of the already existed monomers or initial aggregates on the mica {001} cleavage plane. In view of the low density of protofibrils in Fig.3.12 A, collagen solution with a much higher concentration, 30 μg/ml, was used instead while the same procedure was followed. But the collagen concentration was probably too high so that in Fig.3.12 B no single fibrils could be distinguished on such a crowded pattern. Such fibrils are generally 1 nm in height and 150 nm in width at the maximum section.

As we mentioned, proteins could act as both nucleation templates and specific growth inhibitors based on the mineral crystal-protein recognition during the biomineralization process. It is supported by experiments where alkane monolayers of various compositions as well as proteins were shown to operate as catalysts for crystallization by virtue of their complementarity to the crystal surface on one plane. [18,41-50] Because an osteon in the mammal cortical bone is structured by concentric collagen fiber networks with nano-sized thin elongated hydroxyapatite platelets fitting in extra- and intra- fibrillar spaces and aligning with the same orientation of the fibers [38,39], scientists have been very eager to understand the real roles played by collagens during the biomineralization process. Although it was reported that only with the

96

assistance of some noncollagenous proteins (NCPs) tightly bound to the collagen scaffold, hydroxyapatite could be first nucleated in the gap region of the collagen fibrils and then anisotropically grow into mineral platelets within the collagen fibrils in a highly organized staggered manner, we still want to further investigate it with our patterned protofibrils under quasiepitaxial growth. However, in our experiments, if we mix Ca^{2+} ions and phosphate ions together and put such mixture on a patterned collagen protofibrils existed already, amorphous calcium phosphate could cover the whole pattern and make AFM imaging impossible. So, in our experiment, first we tried to get some calcium rich or phosphate rich monomers or initial aggregates (assuming monomers could trap such ions at some specific biding sites), then incubate the samples in the buffer containing the other ions. Perhaps, we would be lucky to find hydroxyapatite nucleation on the protofibrils.

In Fig.3.13 A, we designed the experiment to make 5.0 μg/ml calcium rich collagen solution (pH 7.5) containing 20 mM Ca^{2+} and 200 mM NaCl first, flush the solution on a mica surface, and then rinse and incubate the sample with the phosphate buffer (pH 7.5) of 8.2 mM KH_2PO_4, 41.8 mM K_2HPO_4 and 200 mM KCl overnight. In Fig.3.13 A, on an area of 3.0 μm × 3.0 μm, fibrils were aligned perfectly to one direction. The average height of the fibrils was 2.5 nm, the average width is 100 nm, and the average spacing between two neighbors was around 450 nm. Comparing the protofibrils in Fig.3.5, one can find that the protofibrils in the two experiments look very similar. But the collagen solution used here was of a concentration more than ten times higher, and the fibrils obtained here were generally thicker. However, in this experiment, we could not find any

97

mineral crystal nucleation points along the fibrils. Probably during the rinsing procedure, most of the Ca^{2+} ions were just washed off; some Ca^{2+} ions trapped by collagen molecules were not concentrated enough to form calcium phosphate precipitate, much less crystalline hydroxyapatite.

Interestingly, a reverse procedure compared to the experiment above was used to
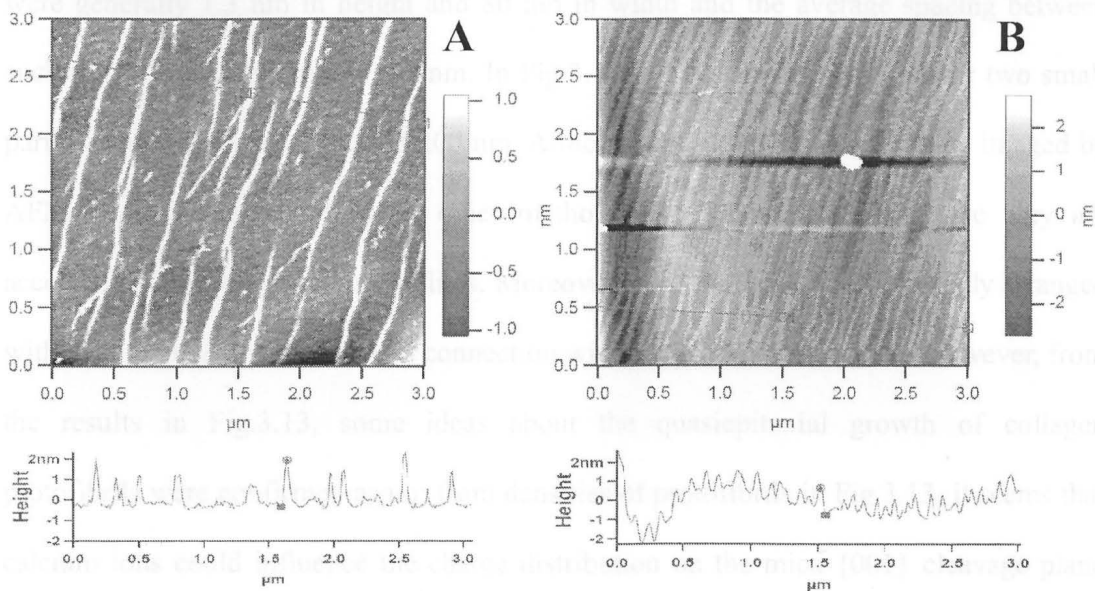
Figure 3.13 AFM topographic images (AC Mode) of patterned collagen protofibrils quasiepitaxially grown on mica surface under solution with the line-scan height spectra shown below. The scan area is always 3.0 μm × 3.0 μm. A: The mica surface was flushed by 5.0 μg/ml collagen monomers in 20 mM Ca^{2+} solution (200 mM Na^+, pH 7.5) and incubated by 50 mM phosphate buffer (200 mM K^+, pH 7.5) overnight; B: The mica surface was flushed by 5.0 μg/ml collagen monomers in 50 mM phosphate buffer (200 mM Na^+, pH 7.5) and incubated in 20 mM Ca^{2+} solution (200 mM K^+, pH 7.5) overnight.

98

prepare sample next. A freshly cleaved mica surface was flushed by 5.0 μg/ml collagen solution in the phosphate buffer (pH 7.5) containing 8.2 mM NaH_2PO_4, 41.8 mM Na_2HPO_4 and 200 mM NaCl, and then was rinsed and incubated by the solution (pH 7.5) containing 20 mM Ca^{2+} and 200 mM KCl overnight. In Fig.3.13 B, crowded protofibrils with uniform orientation were found everywhere on the mica surface. Protofibrils here were generally 1.3 nm in height and 80 nm in width and the average spacing between such fibrils was only around 100 nm. In Fig.3.13 B, one can also find one or two small particles with a diameter around 200 nm. Although the small particles can be imaged by AFM, more characterization by other methods like IR is required before they are accepted as hydroxyapatite crystallites. Moreover, such particles were randomly arranged without showing any pronounced connection with the protofibrils around. However, from the results in Fig.3.13, some ideas about the quasiepitaxial growth of collagen protofibrils were confirmed again: from densities of protofibrils in Fig.3.13, it seems that calcium ions could influence the charge distribution on the mica {001} cleavage plane and thus decrease the absorption amount of collagen molecules on the mica surface, and that making collagen solution in a stable pH in phosphate buffer could be useful for the initial nucleation of fibril formation and result in crowded protofibrils. From the average size of the protofibrils, it seems that phosphate ions could also be helpful for the surface-mediated association of the already existing monomers or initial aggregates on the mica {001} cleavage plane into thick protofibrils.

As we discussed previously, under the quasiepitaxial regulation of the mica lattices on both the alignment and the movement of the collagen monomers and initial

99

aggregates, ultrathin collagen protofibrils can be formed on the mica surface under solution and be oriented along a specific direction. However, from the experiments in this section, one can find the monomers' inherent self-assembly properties, which were adjusted by using buffers or solutions containing different ions, can severely influence the morphologies of the patterned protofibrils on the mica surface although those self-assembly properties might not change the orientation of the protofibrils at all.

3.3.2.3 Incubation time

It was reported that fibroblasts in cell culture could initially reorganize collagen gels into anisotropic strips at the first 6-15 min, and continue the process over 7 h. As a matter of fact, while Muller and coworkers tried to use AFM to manipulate the freshly assembled protofibrils, they also found that the protofibril arrays were stabilized over 4-5 hours. But after that critical period, the fibrils could not be further manipulated in a controlled manner, and the resulting collagen coatings could remain stable for several months without loss of fiber orientation or mechanical strength. Actually, in our experiments, we also found the patterned protofibrils were usually stabilized over 4-5 hours (data not shown). But during this short period, it is really hard for AFM to map the time course of the initial patterning due to the perturbation brought by the AFM tip.

As we discussed, with the regulation of mica {001} cleavage lattices, the quasiepitaxial growth of the protofibrils always happens on a specific scale. However, is it possible for higher hierarchical structures to emerge from the patterned protofibrils? Although we believed the long term results from Muller's work, we still investigated to what extent the long incubation time could influence the fibril pattern formation. In the

100
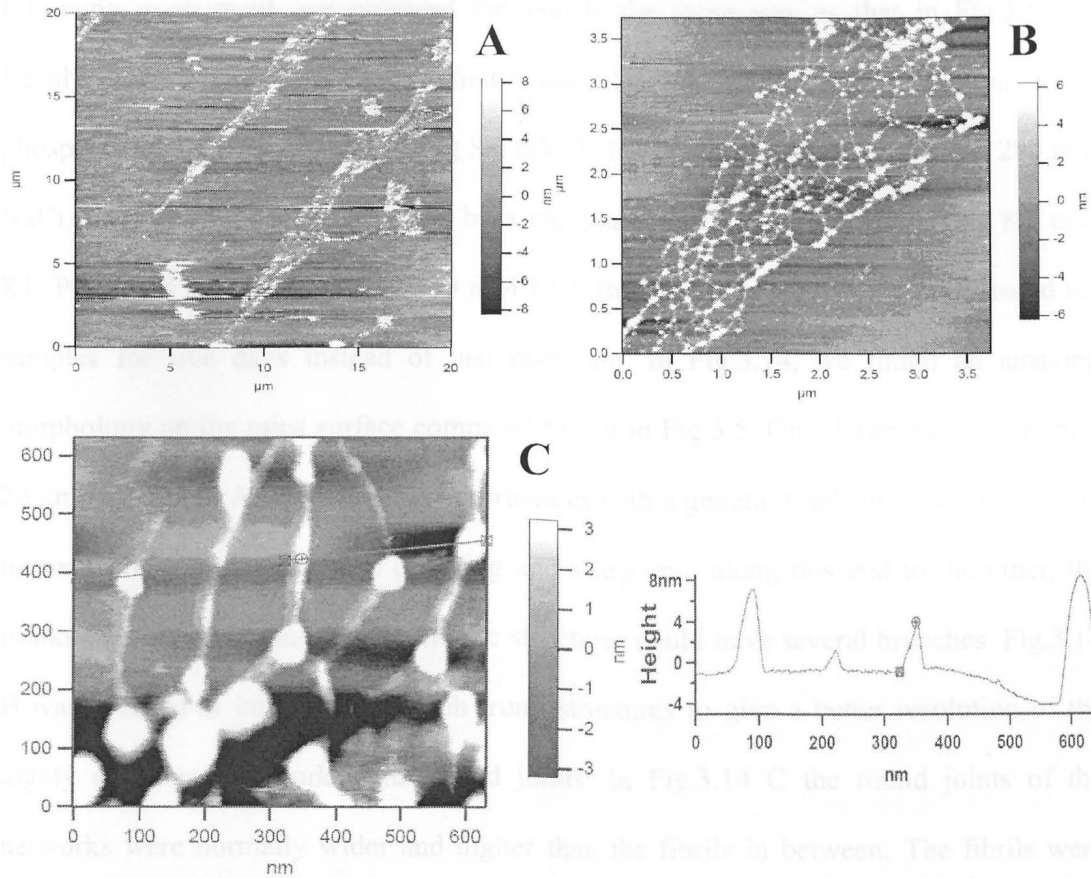
Figure 3.14   AFM topographic image (AC Mode) of patterned collagen protofibrils grown on the mica surface under phosphate buffer. The sample was made by the same procedure as that in Fig.3.5: the mica surface was flushed by 0.3 μg/ml collagen monomers in 50 mM phosphate buffer (200 mM Na$^+$, pH 7.5) and incubated by 50 mM phosphate buffer (200 mM K$^+$, pH 7.5). But the sample had been incubated for five days before imaging. A: a scan area of 20 μm × 20 μm; B: a zoom-in scan of A on an area of 3.7 μm × 3.7 μm; C: a zoom-in scan of B on an area of 630 nm × 630 nm with the line-scan height spectrum shown on the right.

following experiment, we prepared the sample the same way as that in Fig.3.5: the freshly cleaved mica surface was first flushed by 0.3 μg/ml collagen solution in the phosphate buffer (pH 7.5) containing 8.2 mM NaH_2PO_4, 41.8 mM Na_2HPO_4 and 200 mM NaCl, then was rinsed and buffered by a phosphate buffer (pH 7.5) containing 8.2 mM KH_2PO_4, 41.8 mM K_2HPO_4 and 200 mM KCl. But in this experiment, we incubated the samples for five days instead of just overnight. In Fig.3.14, we found an amazing morphology on the mica surface compared to that in Fig.3.5. On a large area of 20 μm × 20 μm in Fig.3.14 A, several network structures with a general trunk shape of trees could be seen: those structures have one long and sharp end; along this end to the other, the trunks became wider and wider; and the structures could have several branches. Fig.3.14 B was a zoom-in image within such trunk structures to give a better resolution of the highly organized networks with round joints. In Fig.3.14 C the round joints of the networks were normally wider and higher than the fibrils in between. The fibrils were around 4 nm high and 45 nm wide, and the average fibrils' length between two joints was around 250 nm; the joints ranged from 30 nm to 100 nm in width, and around 30 nm in height.

In view of the inconsistencies between our long term incubation results and Muller's, we found that during our incubation process, we used a drop of buffer solution to cover the mica surface, while in Muller's work, they probably used a fluid cell.[64] So, in our long time incubation, the huge drying effect probably caused collagen fibrils to rearrange into network structures, and caused mineral to precipitate among the initial networks and finally turn into the round joints. More systematical works are required for the further

102

investigation on the network based collagen trunk structures.

3.4 *Conclusion*

In sum, in our experiments, we successfully created and imaged patterned collagen protofibrils quasiepitaxially grown on the mica {001} and HOPG {0001} cleavage planes. Since our method was based on the self-assembly of collagen monomers or collagen initial aggregates, we might call this method a 'bottom up' method for creating patterned collagen protofibrils. In our experiments, we found that although amorphous growth of collagen structures on the nonpolar HOPG surface can not be well handled, the quasiepitaxial growth of collagen protofibrils on a charged mica surface can be precisely controlled by adjusting the concentration of collagen solution, the buffers, and maybe the incubation time. By our quasiepitaxial growth methods, we can roughly bridge the hierarchical structures on the nano-to-mesoscale between collagen monomers and big collagen fibrils. We believe that our unique discoveries will definitely provide insight into the origin of the collagen matrix from fibroblasts and even the structure-based functions of the extracellular matrix (ECM), and that the patterned collagen protofibrils could also serve as platforms or scaffolds to direct cellular research and biomineralization studies.

3.5 *Bibliography and References*

[1]   S. R. Forrest, *Chem. Rev.*, 1997, **97**, 1793-1896.

[2]   S. R. Forrest, M. L. Kaplan, P. H. Schmidt, *J. Appl. Phys.*, 1984, **56**, 543-551.

[3]   J. Tersoff, R. M. Tromp, *Phys. Rev. Lett.*, 1993, **70**, 2782-2785.

[4]   S. R. Forrest, P. E. Burrows, E. I. Haskal, F. F. So, *Phys. Rev. B*, 1994, **49**, 11309-11321.

[5]   C. W. Tang, S. A. VanSlyke, *Appl. Phys. Lett.*, 1987, **51**, 913-915.

[6]   P. E. Burrows, S. R. Forrest, *Appl. Phys. Lett.*, 1993, **62**, 3102-3104.

[7]   F. F. So, S. R. Forrest, *Phys. Rev. Lett.*, 1991, **66**, 2649-2652.

[8]   P. Fenter, F. Schreiber, L. Zhou, P. Eisenberger, S. R. Forrest, *Phys. Rev. B*, 1997, **56**, 3046-3053.

[9]   H. Plank, R. Resel, S. Purger, J. Keckes, A. Thierry, B. Lotz, A. Andreev, N. S. Sariciftci, H. Sitter, *Phys. Rev. B*, 2001, **64**, 235423-1-5.

[10]   A. Yu. Andreev, H. Sitter, C. J. Brabec, P. Hinterdorfer, G. Springholz, N. S. Sariciftci, R. Resel, H. Plank, *Mat. Res. Soc. Symp. Proc.*, 2001, **665**, C5.24.1-C5.24.6.

[11]   A. Yu. Andreev, H. Sitter, C. J. Brabec, P. Hinterdorfer, G. Springholz, N. S. Sariciftci, *Syn. Mater.*, 2001, **121**, 1379-1380.

[12]   A. Andreev, C. Teichert, G. Hlawacek, H. Hoppe, R. Resel, D. M. Smilgies, H. Sitter, N.S. Sariciftci, *Org. Electron.*, 2004, **5**, 23-27.

[13]   H. Sitter, A. Andreev, C. Teichert, G. Hlawacek, T. Haber, D. M. Smilgies, R. Resel, A. M. Ramil, N. S. Sariciftci, *Phys. Stat. Sol. (b)*, 2005, **242**, 1877-1882.

104

[14]   G. Hlawacek, C. Teichert, A. Yu. Andreev, H. Sitter, S. Berkebile, G. Koller, M. Ramsey, R. Resel, *Phys. Stat. Sol. (a)*, 2005, **202**, 2376-2385.

[15]   C. Teichert, G. Hlawacek, A. Yu. Andreev, H. Sitter, P. Frank, A. Winkler, N. S. Sariciftci, *Appl. Phys. A*, 2006, **82**, 665-669.

[16]   D. Perl-Treves, L. Addadi, *Mol. Cryst. Liq. Cryst.*, 1990, **187**, 1-16.

[17]   M. Kam, D. Perl-Treves, D. Caspi, L. Addadi, *FASEB J.*, 1992, **6**, 2608-2613.

[18]   L. Addadi, S. Weiner, M. Geva, *Z. Kardiol. 90: Suppl. 3*, 2001,III/92-III/98.

[19]   V. I. Shestopalov, S. Bassnett, *J. Cell Sci.*, 2003, **116**, 4191-4199.

[20]   M. J. Seibel, *Clin. Biochem Rev.*, 2005, **26**, 97-122.

[21]   C. B. Flies, J. Peplies, D. Schüler, *Appl. Environ. Microbiol.*, 2005, **71**, 2723-2731.

[22]   N. Nassif, N. Pinna, N. Gehrke, M. Antonietti, C. Jäger, H. Cölfen, *Proc. Natl. Acad. Sci. USA*, 2005, **102**, 12653-12655.

[23]   H. Endo, Y. Takagi, N. Ozaki, T. Kogure, T. Watanabe, *Biochem. J.*, 2004, **384**, 159-167.

[24]   T. J. Beveridge, L. L. Graham, *Microbiol. Rev.*, 1991, **55**, 684-705.

[25]   D. Emerson, W. C. Ghiorse, *J. Bacteriol.*, 1993, **175**, 7819-7827.

[26]   R. D. Klein, Q. Gu, A. Goddard, A. Rosenthal, *Proc. Natl. Acad. Sci. USA*, 1996, **93**, 7108-7113.

[27]   A. J. Dumanski, H. Hedelin, A. Edin-Liljegren, D. Beauchemin, R. J. McLean, *Infect. Immun.*, 1994, **62**, 2998-3003.

[28]   C. C. Keller, J. B. Hittner, B. K. Nti, J. B. Weinberg, P. G. Kremsner, D. J.

Perkins, *Mol. Med.*, 2004, **10**, 45-54.

[29]   S. Xiao, C. Yu, X. Chou, W. Yuan, Y. Wang, L. Bu, G. Fu, M. Qian, J. Yang, Y. Shi, L. Hu, B. Han, Z. Wang, W. Huang, J. Liu, Z. Chen, G. Zhao, X. Kong, *Nat. Genet.*, 2001, **27**, 201-204.

[30]   M. L. Wallwork, J. Kirkham, H. Chen, S. X. Chang, C. Robinson, D. A. Smith, B. H. Clarkson, *Calcif. Tissue Int.*, 2002, **71**, 249-255.

[31]   T. Sreenath, T. Thyagarajan, B. Hall, G. Longenecker, R. D'Souza, S. Hong, J. T. Wright, M. MacDougall, J. Sauk, A. B. Kulkarni, *J. Biol. Chem.*, 2003, **278**, 24874-24880.

[32]   H. Furedi-Milhofer, J. Mordian-Oldak, S. Weiner, A. Veis, K. P. Mintz, L. Addadi, *Connective Tiss. Res.*, 1994, **30**, 251-264.

[33]   D. S. C. Yang, M. Sax, A. Chakrabartty, C. L. Hew, *Nature*, 1988, **339**, 232-237.

[34]   Z. Jia, C. I. DeLuca, H. Chao, P. L. Davies, *Nature*, 1996, **384**, 285-288.

[35]   J. J. Gray, *Curr. Opin. Struct. Biol.*, 2004, **14**, 110-115.

[36]   D. A. Walters, B. L. Smith, A. M. Belcher, G. T. Paloczi, G. D. Stucky, D. E. Morse, P. K. Hansma, *Biophys. J.*, 1997, **72**, 1425-1433.

[37]   S. R. Qiu, A. Wierzbicki, C. A. Orme, A. M. Cody, J. R. Hoyer, G. H. Nancollas, S. Zepeda, J. J. De Yoreo, *Proc. Natl. Acad. Sci. USA*, 2004, **101**, 1811-1815.

[38]   S. Cazalbou, C. Combes, D. Eichert, C. Rey, *J. Mater. Chem.*, 2004, **14**, 2148-2153.

[39]   S. Weiner, W. Traub and H. D. Wagner, *J. Struct. Biol.*, 1999, **126**, 241-255.

[40]   L. Addadi, S. Weiner, *Angew. Chem. Int. Ed. Eng.*, 1992, **31**, 153-169.

[41]   L. Addadi, J. Moradian, N. G. Maroudas, S. Weiner, *Proc. Natl. Acad. Sci. USA*, 1987, **84**, 2732-2736.

[42]   E. M. Landau, M. Levanon, L. Leiserowitz, L. Lahav, J. Sagiv, *Nature*, 1985, **318**, 353-356.

[43]   B. R. Heywood, S. Mann, *Chem. Mat.*, 1994, **6**, 311-318.

[44]   A. Berman, D. J. Ahn, A. Lio, M. Salmeron, A. Reichert, D. Charych, *Science*, 1995, **269**, 515-518.

[45]   J. Aizenberg, A. J. Black, G. M. Whitesides, *Nature*, 1999, **397**, 495-498.

[46]   J. Falini, S. Albeck, S. Weiner, L. Addadi, *Science*, 1996, **271**, 67-69.

[47]   R. Lakshminarayanan, R. M. Kini, S. Valiyaveettil, *Proc. Natl. Acad. Sci. USA*, 2002, **99**, 5155-5159.

[48]   F. Marin, M. Smith, Y. Isa, G. Muyzer, P. Westbroek, *Proc. Natl. Acad. Sci. USA*, 1996, **93**, 1554-1559.

[49]   B. Christensen, M. Nielsen, K. Haselmann, T. Petersen, E. Sørensen, *Biochem. J.*, 2005, **390**, 285-292.

[50]   Y. C. Liou, A. Tocilj, P. L. Davies, Z. Jia, *Nature*, 2000, **406**, 322-324.

[51]   A. McPherson, P. Shlichta, *Science*, 1988, **239**, 385-387.

[52]   W. L. Kimble, T. E. Paxston, R.W. Rousseau, A. Sambanis, *J. Cryst. Growth*, 1998, **187**, 268-276.

[53]   N. E. Chaen, E. Saridakis, R. El-Bahar, Y. Nemirovsky, *J. Mol. Biol.*, 2001, **312**, 591-595.

[54]   E. Pechkova, C. Nicolini, *J. Cryst. Growth*, 2001, **231**, 599-602.

[55]   D. Tsekova, S. Dimitrova, Ch. Nanev, *J. Cryst. Growth*, 2001, **196**, 226-233.

[56]   S. Fermany, G. Falini, M. Munnicci, A. Ripamonti, *J. Cryst. Growth*, 2002, **224**, 327-334.

[57]   Y. Sheng, H. Tsao, J. Zhou, S. Jiang, *Phys. Rev. E*, 2002, **66**, 011911-1-5.

[58]   G. Di Profio, E. Curcio, A. Cassetta, D. Lamba, E. Drioli, *J. Cryst. Growth*, 2003, **257**, 359-369.

[59]   T. Bergfords, *J. Struct. Biol.*, 2003, **142**, 66-76.

[60]   A. A. Chernov, *J. Struct. Biol.*, 2003, **142**, 3-21.

[61]   G. Yang, K. A. Woodhouse, C. M. Yip, *J. Am. Chem. Soc.*, 2002, **124**, 10648-10649.

[62]   D. Dobrev, D. Baur, R. Neumann, *Appl. Phys. A*, 2005, **80**, 451-456.

[63]   X. Liu, Y. Zhang, D. K. Goswami, J. S. Okasinski, K. Salaita, P. Sun, M. J. Bedzyk, C. A. Mirkin, *Science*, 2005, **307**, 1763-1766.

[64]   F. Jiang, H. Horber, J. Howard, D. J. Muller, *J. Struct. Biol.*, 2004, **148**, 268-278.

[65]   F. Jiang, K. Khairy, K. Poole, J. Howard, D. J. Muller, *Microsc. Res. Tech.*, 2004, **64**, 435-440.

[66]   K. Poole, K. Khairy, J. Friedrichs, C. Franz, D. A. Cisneros, J. Howard, D. J. Mueller, *J. Mol. Biol.*, 2005, **349**, 380-386.

[67]   D. A. Cisneros, C. Hung, C. M. Franz, D. J. Muller, *J. Struct. Biol.*, 2006, **154**, 232-245.

[68]   K. E. Kadler, D. F. Holmes, J. A. Trotter, J. A. Chapman, *Biochem. J.*, 1996, **316**, 1-11.

[69]   D. F. Holmes, J. A. Chapman, *Biochem. Biophys. Res. Commun.*, 1979, **87**, 993-999.

[70]   J. Parkinson, K. E. Kadler, A. Brass, *J. Mol. Biol.*, 1994, **247**, 823-831.

[71]   D. Czajkowsky, H. Iwamoto, Z. F. Shao, *J. Electron Microsc.*, 2000, **49**, 395-406.

[72]   M. Rief, M. Gautel, F. Oesterhelt, J. M. Fernandez, H. E. Gaub, *Science*, 1997, **276**, 1109-1112.

[73]   T. E. Fisher, P. E. Marszalek, J. M. Fernandez, *Nature Struct. Biol.*, 2000, **7**, 719-724.

[74]   D. J. Muller, C. A. Schoenenberger, G. Buldt, A. Engel, *Biophys. J.*, 1996, **70**, 1796-1802.

[75]   D. J. Muller, G. Buldt, A. Engel, *J. Mol. Biol.*, 1995, **249**, 239-243.

[76]   H. G. Hansma, J. Vesenka, C. Siegerist, G. Kelderman, H. Morrett, R. L. Sinsheimer, V. Elings, C. Bustamante, P. K. Hansma, *Science*, 1992, **256**, 1180-1184.

[77]   E. Henderson, *Nucleic Acids Res.*, 1992, **20**, 445-447.

[78]   M. Gale, M. S. Pollanen, P. Markiewicz, M. C. Goh, *Biophys. J.*, 1995, **68**, 2124-2128.

[79]   L. I. Fessler, N. P. Morris, J. H. Fessler, *Proc. Natl. Acad. Sci. USA*, 1975, **72**, 4905-4909.

[80]   K. E. Kadler, Y. Hojima, D. J. Prockop, *J. Biol. Chem.*, 1988, **263**, 10517-10523.

[81]   W. Traub, T. Arad, S. Weiner, *Matrix*, 1992, **12**, 251-255.

[82]   I. Jager, P. Fratzl, *Biophys. J.*, 2000, **79**, 1737-1746.

[83]   J. A. Trotter, J. A. Chapman, K. E. Kadler, D. F. Holmes, *J. Mol. Biol.*, 1998,

284, 1417-1424.

[84]   D. E. Birk, R. A. Hahn, C. Y. Linsenmayer, Z. I. Zycband, *Matrix Biol.*, 1996, **15**, 111-118.

[85]   D. Silver, J. Miller, R. Harrison, D. J. Prockop, *Proc. Natl. Acad. Sci. USA*, 1992, **89**, 9860-9864.

[86]   K. E. Kadler, Y. Hojima, D. J. Prockop, *J. Biol. Chem.*, 1987, **262**, 15696-15701.

[87]   A. Fertala, D. F. Holmes, K. E. Kadler, A. L. Sieron, D. J. Prockop, *J. Biol. Chem.* 1996, **271**, 14864-14869.

[88]   X. Liu, H. Wu, M. Byrne, S. Krane, R. Jaenisch, *Proc. Natl. Acad. Sci. USA*, 1997, **94**, 1852-1856.

[89]   K. G. Danielson, H. Baribault, D. F. Holmes, H. Graham, K. E. Kadler, R. V. Iozzo, *J. Cell Biol.*, 1997, **136**, 729-743.

[90]   D. F. Holmes, R. B. Watson, B. Steinman, K. E. Kadler, *J. Biol. Chem.*, 1993, **268**, 15758-15765.

[91]   J. Hao, B. Zou, K. Narayanan, A. George, *Bone*, 2004, **34**, 921-932.

[92]   K. Narayanan, A. Ramachandran, J. Hao, G. He, K. W. Park, M. Cho, A. George, *J. Biol. Chem.*, 2003, **278**, 17500-17508.

[93]   R. L. Trelstad, K. Hayashi, J. Gross, *Proc. Natl. Acad. Sci., USA*, 1976, **73**, 4027-4031.

[94]   A. J. Hodge, J. A. Petruska, *Recent studies with the electron microscope on ordered aggregates of the tropocollagen molecule*, in G. N. Ramachandran, (Ed.), *Aspects of Protein Chemistry*, **1963**, Academic Press, London.

[95]   J. Bradt, M. Mertig, A. Teresiak, W. Pompe, *Chem. Mater.*, 1999, **11**, 2694-2701.

[96]   D. J. S. Hulmes, A. Miller, S. W. White, B. Brodsky-Doyle, *J. Mol. Biol.*, 1977, **110**, 643-666.

[97]   E. P. Paschalis, O. Jacenko, B. Olsen, R. Mendelsohn, A. L. Boskey, *Bone*, 1996, **19**, 151-156.

[98]   A. L. Boskey, R. Mendelsohn, *Vib. Spectrosc.*, 2005, **38**, 107-114.

[99]   D. Baselt, J. Revel, J. Baldeschwieler, *Biophys. J.*, 1993, **65**, 2644-2655.

[100]   J. K. Rainey, C. K. Wen, M. C. Goh, *Matrix Biol.*, 2002, **21**, 647-660.

[101]   Y. Sun, Z. Luo, A. Fertala, and K. An, *Biochem. Biophys. Res. Commun.*, 2002, **295**, 382-386.

[102]   N. Ishida, T. Inoue, M. Miyahara, K. Higashitani, *Langmuir*, 2000, **16**, 6377-6380.

[103]   K. K. Berggren, A. Bard, J. L. Wilbur, J. D. Gillaspy, A. G. Helg, J. J. McClelland, S. L. Rolston, W. D. Phillips, M. Prentiss, G. M. Whitesides, *Science*, 2000, **260**, 1255-1257.

[104]   S. Hong, C. A. Mirkin, *Science*, 2000, **288**, 1808-1811.

[105]   J. D. Gerding, D. M. Willard, A. Van Orden, *J. Am. Chem. Soc.*, 2005, **127**, 1106-1107.

[106]   F. Cattaruzza, A. Cricenti, A. Flamini, M. Girasole, G. Longo, T. Prosperi, G. Andreano , L. Cellai, E. Chirivino, *Nucleic Acids Res.*, 2006, **34**, e32.

[107]   K. Beck, B. Brodsky, *J. Struct. Biol.*, 1998, **122**, 17-29.

[108]   http://users.easystreet.com/kxm/eng/collagen.htm

[109] N. Guven, *Zeitschrift fur Kristallographie*, 1971, **134**, 196-212.

[110] H. Takeda, M. Ross, *American Mineralogist*, 1995, **80**, 715-724.

[111] J.V. Smith, H. S. Yoder, *Mineralogical Magazine*, 1956, **31**, 209-235.

[112] D. F. Holmes, M. J. Capaldi, J. A. Chapman, *Int. J. Biol. Macromol.*, 1986, **8**, 161-166.

[113] D. J. Hulmes, *J. Struct. Biol.*, 2002, **137**, 2-10.

[114] V. Ottani, D. Martini, M. Franchi, A. Ruggeri, M. Raspanti, *Micron*, 2002, **33**, 587-596.

[115] L. Bozec, M. Horton, *Biophys. J.*, 2005, **88**, 4223-4231.

[116] A. K. Freund, A. Munkholm and S. Brennan, *Proc. SPIE*, 1996, **2856**, 68-79.

[117] X. Lu, H. Huang, N. Nemchuk, R. S. Ruoff, *Appl. Phys. Lett.*, 1999, **75**, 193-195.

[118] J. Y. Huang, *Acta. mater.*, 1999, **47**, 1801-1808.

[119] A. Tuffanelli, M. Sanchez del Rio, G. Pareschi, M. Gambaccini, A. Taibi, A. Fantini, M. Ohler, *Proc. SPIE*, 1999, **3773**, 192-198.

[120] S. Banerjee, M. Sardar, N. Gayathri, A. K. Tyagi, B. Raj, *Phys. Rev. B*, 2005, **72**, 075418-1-7.

[121] G. Mao, D. Chen, H. Handa, *Langmuir*, 2005, **21**, 578-585.

[122] G. Radu, U. Memmert, H. Zhang, G. Nicolay, F. Reinert, U. Hartmann, *J. Phys. Chem. B*, 2002, **106**, 10301-10305.

[123] E. Strauss, B. Thomas, S.T. Yau, *Langmuir*, 2004, **20**, 8768-8772.

[124] M. J. Capaldi, J. A. Chapman, *Biopolymers*, 1982, **21**, 2291-2313.

112

[125]   P. Nelson, *Biological Physics*, **2004**, W. H. Freeman and Co.: NY.

[126]   J. Gross, D. Kirk, *J. Biol. Chem.*, 1958, **233**, 355-360.

[127]   G. C. Wood, M. K. Keech, *Biochem. J.*, 1960, **75**, 588-598.

[128]   A. Miller, D. A. D. Parry, *J. Mol. Biol.*, 1973, **75**, 441-447.

[129]   R. A. Gelman, K. A. Piez, *J. Biol. Chem.*, 1980, **255**, 8098-8102.

[130]   F. H. Silver, K. H. Langley, and R. L. Trelstad, *Biopolymers*, 1979, **18**, 2523-2535.

[131]   F. H. Silver, *J. Biol. Chem.*, 1981, **256**, 4973-4977.

[132]   M. F. Paige, J. K. Rainey, M. C. Goh, *Biophys. J.*, 1998, **74**, 3211-3216.

[133]   T. Hayashi, Y. Nagai, *J. Biochem.*, 1972, **72**, 749-758.

[134]   D. J. S. Hulmes, A. Miller, D. A. D. Parry, K. A. Piez, J. Woodhead-Galloway, *J. Mol. Biol.*, 1973, **79**, 137-148.

113

Chapter 4
Patterned two dimensional collagen bundles created by a Top-Down method
----- the AFM tip as a molecular broom

4.1 *Introduction*

Characterizing the morphologies of polymers on different substrates and understanding mechanisms of the organization of polymers has been extensively approached by different means and theories.[1-7] Controlling the formation and the spatial organization of adsorbed polymers on substrates has also been under intense investigation.[8-13] As the most important biopolymers, extracellular matrix (ECM) proteins have been aroused researchers' interest because patterned ECM protein surfaces on substrates have lots of potential applications, such as the development of biosensors, bioreactors, immunoassays, and the biocompatible implants.[14-21] Different physical and chemical treatments focused on both ECM proteins and substrates were used to enhance the protein-coated surface properties since oriented topographical features (fibers, grooves) of the substrates' surface induce the orientation of the cells, a phenomenon known as "contact guidance" and important in cell adhesion, shape, motility and physiology.[15,22-30]

Among all of the proteins under investigation, collagens are so important because they are the major constituents of the connective tissues of multicellular animals.[14,31-33] As the most important extracellular matrix (ECM) proteins found in a wide range of

114

vertebrates and invertebrates, collagen fibrils are acting as both solid state regulators for cellular function and scaffolding of the tissue architecture, particularly in large vertebrates.[14,31-42] As the molecular unit of collagen fibrils, each collagen monomer consists of three polypeptide chains coiled around each other and thus forms a triple helix. In every single chain of a collagen monomer helix, every three amino acid residues there must be a glycine to induce the final triple-helical structure, and other amino acids present abundantly are most likely to be proline and hydroxyproline. Among more than 20 types of monomers, Type I collagen is distinguished by its abundance in mammalian organisms. The Type I collagen helical molecule is a heterotrimer comprising two identical α_1(I) chains and one α_2(I) chain. The α_1(I) and α_2(I) chains are very similar, but their primary structures are coded by separate genes. Each of the α-chains contain a little more than 1000 amino acid residues and have molecular weights of approximately 95,000 Da. In Type I collagen monomers, the triple-helix occurs throughout 95% of the length of the rod-like monomer. The other 5% comprise the 17 N-terminal residues and the 26 C-terminal residues, which do not have glycine as every third residue. These are called telopeptides and are assumed to provide information for self-assembly into fibrils of 67 nm axial periodicity (D-banding).[42-54]

It is reported that collagen directly mediates cell adhesion and is therefore frequently used for the coating of cell culture flasks and dishes,[36] and collagenous materials are applied in tissue engineering products which were recently developed for applications in dermatology, orthopedics, or oral surgery.[36,37,55] Although Nature accomplishes the construction of well organized extracellular matrix (ECM) through the

115

process of self-assembly, relying on noncovalent and covalent interactions between relatively small precursor molecules, such "bottom-up" approaches to supramolecular organization are not well understood and in most of the cases, are so tough to be applied. [56-60] For instance, during the established protocols for the coating of cell culture carriers that usually make use of Type I collagen monomers, the monomeric tropocollagen forms thin layers which do not resemble the naturally occurring functional matrices.[36,61,62] In view of the situation, practical but more efficient methods are required to control topographical features of the coating surface.

As a matter of fact, during the past years, new top-down methods like Microcontact printing and Nanolithography of Scanning Probe Microscopy (SPM) have emerged to control the patterned protein-coated surface on the nano-to-mesoscale.[63-65] Direct Microcontact printing of proteins on solid substrates can be done in a second by precisely transferring the proteins from stamp to substrate without loss of biological activities.[66-70] However, Nanolithography of Scanning Probe Microscopy (SPM) has been proven to be a more precise way to manipulate proteins or protein film on the substrates on the nano scale since such manipulation applications including surface scratching and patterning, localized surface oxidation, nanotube and particle manipulation, molecular manipulation, single molecule experiments and more. Since in 1990 IBM imaged and manipulated Xenon atoms with STM (Scanning Tunneling Microscopy), more comprehensive operations of the Scanning Probe Microscopy (SPM) family have been applied to precisely and flexibly manipulate the biological species. [15,23,28,71-75]

Among the SPM family, AFM has been widely applied more recently in many biological systems due to its advantages in surface patterning.[56,64,65,76] First, AFM has a really appropriate control on the sample since the force applied by the AFM tip can range from 10^{-11} N to 10^{-6} N. It is widely accepted that force should not exceed 10^{-11} N in order to not disturb most of the biological surfaces.[9,77] So, by applying different forces on the biological samples, one can both image and manipulate the biological species. Moreover, AFM can operate under physiological conditions, which means the biological species can always maintain their biological activities during the operation. And of course only small amounts of samples (microlitres of fluid or $<$ mm^2 of solid) are required for the sample handling. Since AFM can be used to touch the nanoworld so precisely and conveniently, many exciting experiments such as physical modulating a single protein's conformation, stretching and unfolding a individual DNA molecule, disrupting antibody-antigen bonds, planting nanopatterning of collagen by dip-pen nanolithography and brooming monoclonal IgM film on mica have been carried out with the AFM machine.[56,78-86]

In our experiments, we were trying to use the AFM tips as molecular brooms to pattern the Type I collagen coated Si wafer surface both in air and under water. We also applied the AC mode of the AFM to image the patterned surface under water. The mechanism for the formation of such pattern was also intensively explored.

4.2 *Experimental procedures*

Preparation of collagen samples on Si substrates

All the chemical reagents used were of analytical grade and prepared with

117

ultrapure water (18 MΩ Barnsted Nanopure). 3.0 mg/ml VITROGEN (purified) collagen

for cell culture and biochemistry (pH 2.0, dissolved in 0.012 M HCl) was purchased from

Cohesion (California, USA) and stored at 4 °C. VITROGEN (purified) collagen is 99.9

% pure collagen which is 95-98 % Type I collagen with the remainder being comprised

of type III collagen. For collagen solution preparation, the VITROGEN (purified)

collagen was always diluted with ultrapure water into a solution of the concentration of

30 μg/ml. As the substrate, a square fragment of Si wafer (1.5 cm × 1.5 cm) was used.

The substrate was dried by flushing with a gentle nitrogen flow for about 1 min after it

was washed by 1.0 mM NaOH solution first, then washed by 95% ethanol, and finally

rinsed by ultrapure water. After that, 30 μl of the 30 μg/ml collagen solution prepared

above was dropped by a pipettor onto the clean, dried Si substrate and left there for 30

min. Then ultrapure water was used to rinse the sample twice to remove loosely bound

molecules. Following the rinsing step, the sample was put into a laminar flow hood at

room temperature for at least one day before it was loaded on an AFM machine.

Imaging collagen samples on Si substrates by AFM

The AFM imaging experiments were carried out by the Molecular Force Puller,

MFP 3D (Asylum Research, Santa Barbara, CA, USA). Silicon cantilevers coated with

Cr and Au having a typical force constant of 0.1 N/m (CSC37/Cr-Au) were purchased

from MicroMasch (Estonia). The tips have a nominal force constant of around 0.1 N/m,

the radius of curvature less than 50 nm, a tip height around 15-20 μm, and full tip cone

angle less than 30°. All the samples were imaged in buffers at room temperature. The

patterned collagen surface was created and imaged by Contact Mode at different forces at

118
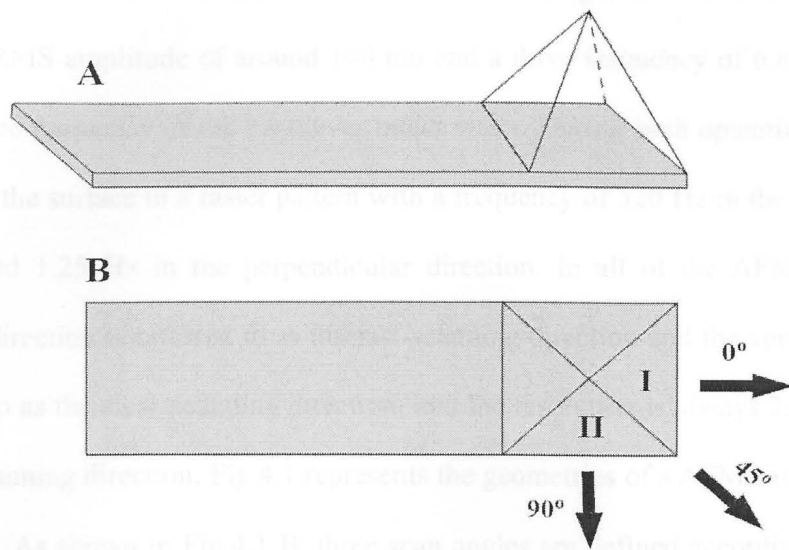
Figure 4.1   Schematic representation of the geometries of a AFM cantilever and the tip. A: a side view of the cantilever and the tip. The AFM cantilever is in a rectangle shape, and on the top of the cantilever, a pyramidal tip was attached in the right end, and was depicted as a transparent pyramid. B: a top view of the cantilever and tip. I and II represent two facets of the pyramidal tip. Black arrows represent three fast-scanning directions: a scan angle of 0° is defined by the fast-scanning direction parallel to the long axis of the cantilever; a scan angle of 90° is defined by the fast-scanning direction perpendicular to the long axis of the cantilever; and a scan angle of 45° is defined by the fast-scanning direction 45° to the long axis of the cantilever, and was at a scan angle of 45°, the projection of the edge between facet I and II on the cantilever is parallel to the fast-scanning direction.

room temperature both in air and under water. AFM images were also obtained in AC Mode at a RMS amplitude of around 100 nm and a drive frequency of 6.8 kHz close to the resonance frequency of the cantilever under water. During both operation modes, the AFM scans the surface in a raster pattern with a frequency of 320 Hz in the fast-scanning direction and 1.25 Hz in the perpendicular direction. In all of the AFM images, the horizontal direction is referred to as the fast-scanning direction and the vertical direction is referred to as the slow-scanning direction, and the resolution is always 256 lines along the slow-scanning direction. Fig.4.1 represents the geometries of a AFM cantilever with a tip attached. As shown in Fig.4.1 B, three scan angles are defined according to different fast-scanning directions: at a scan angle of 0° or 90°, the fast-scanning direction of the tip is parallel or perpendicular to the long axis of the cantilever, and the movement of one of the pyramidal facets (facet I or II) is parallel to the fast-scanning direction; while at a scan angle of 45°, the fast-scanning direction of the tip is 45° to the long axis of the cantilever, and the projection of the edge between two pyramidal facets (facets I and II) is parallel to the fast-scanning direction. In air, only Contact Mode was applied, but under water, both Contact Mode and AC Mode were switched frequently in the same spot to investigate the pattern formation on that area.

4.3 *Results and discussion*

As mentioned in the experimental procedures before, the dry sample which was put into a laminar flow hood at room temperature for one day was loaded on a AFM machine for scanning first at a scan angle of 0° and a force around 80 nN. In Fig.4.2 A, on

120

an area of 10 μm × 10 μm, the first scan showed a surface with lots of objects that are probably collagen aggregates lying randomly and intertwining with each other to some extent, but the roughness on the whole area is less than 1 nm. However, in Fig.4.2 B, on a spot with an area of 2.5 μm × 2.5 μm in the same large area of Fig.4.2 A, another scan with the same force and the same scan angle created a well-defined corrugation on the surface: compact collagen bundles were aligned with each other, and the orientation of the bundles was quite uniform and seemed perpendicular to the fast-scanning direction. In Fig.4.2 B some bundles are around 1.5 nm in height while others are around 3.0 nm in height, and the average width for those bundles are normally 50 nm. However, the length of the bundles ranges from 100 nanometers to several micrometers. Next, Fig.4.2 C shows the AFM image after one more scan with the same force on the same area of Fig.4.2 B. One can find the corrugation surface still consisted of compact collagen bundles and orientation of the bundles was indeed perpendicular to the fast-scanning direction. However, compared with Fig.4.2 B, objects in Fig.4.2 C are not exactly the same, which implies that such bundles are not really stable and a force around 80 nN applied on the AFM tip can easily reshape them. Most of the bundles in Fig.4.2 C are around 5 nm in height, but some bundles still remain 1.5 nm in height, and the average width for those bundles is around 80 nm.

From the results above, one can find that bundles in Fig.4.2 C are generally wider and higher than that in Fig.4.2 B. In the next procedure, a zoom-in scan with the same force and the same scan angle but a smaller area of 800 nm × 800 nm in the area of Fig.4.2 C created even bigger bundles in Fig.4.2 D. The space between the bundles in

121
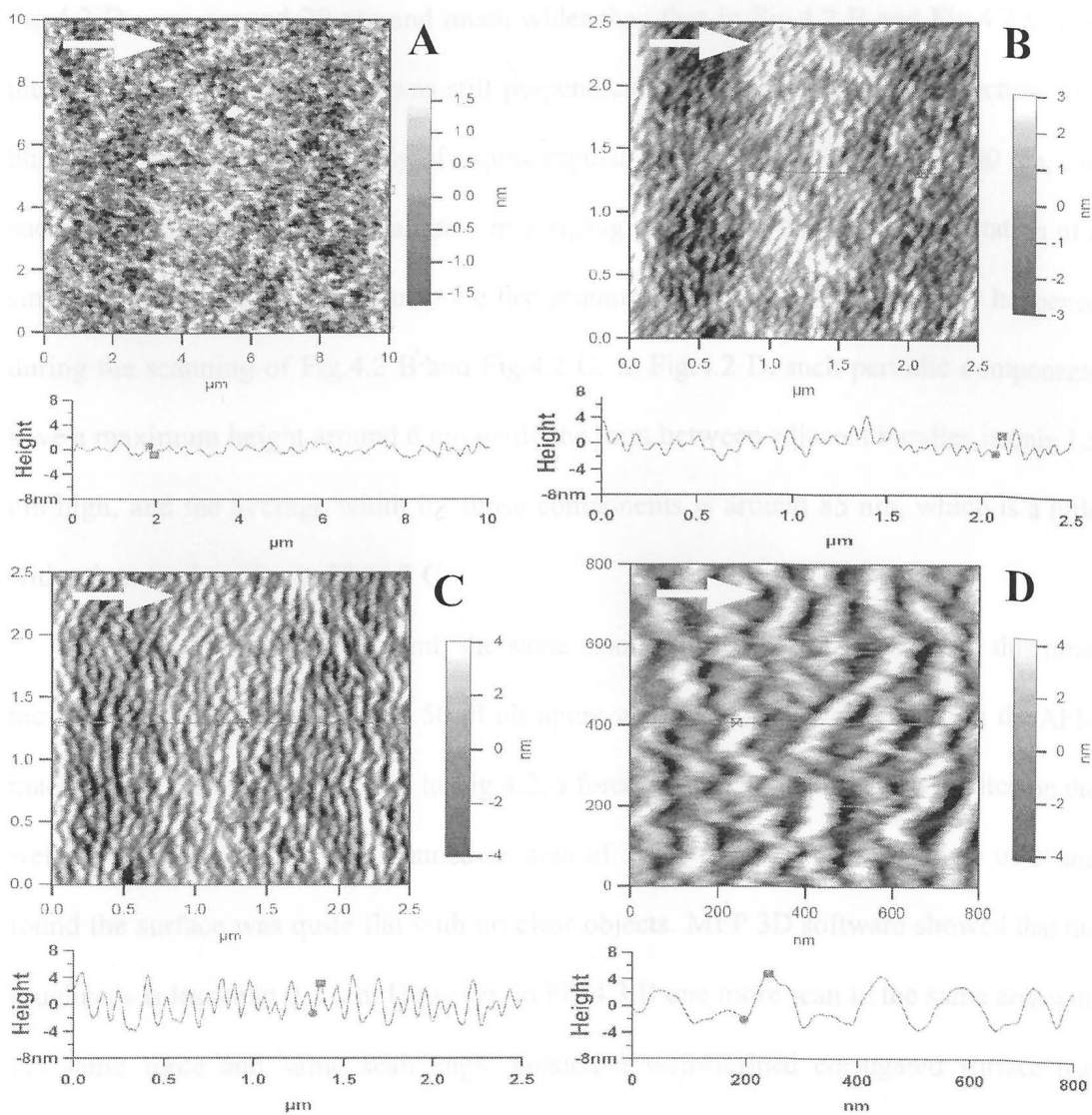
Figure 4.2 AFM topographic images (Contact Mode) of 30 μg/ml collagen coating

on Si wafer in air. A force of around 80 nN was used to create patterns at a scan

angle 0° (indicated by white arrows) on the coated surface from A to D. A: a scan

area of 10 μm × 10 μm; B: a zoom-in scan of A on an area of 2.5 μm × 2.5 μm; C: a

scan on the same area of in B; D: a zoom-in scan of C on an area of 800 nm × 800

nm. The line-scan height spectra are shown below.

122

Fig.4.2 D were around 20 nm and much wider than that in Fig.4.2 B and Fig.4.2 C, and the orientation of the bundles was still perpendicular to the fast-scanning direction. The bundles in Fig.4.2 D are actually of a quite regular lateral periodicity around 100 nm, and such periodic components are aligned in a zigzag pattern but the overall orientation of a single bundle was perpendicular to the fast-scanning direction, which probably happened during the scanning of Fig.4.2 B and Fig.4.2 C. In Fig.4.2 D, such periodic components have a maximum height around 6 nm while the joint between adjacent bundles is only 1.5 nm high, and the average width for those components is around 85 nm, which is a little wider than the bundles in Fig.4.2 C.

During the next experiment, the same sample in Fig.4.2 was used, but this time, the Si surface was covered with 50 μl ultrapure water and then was loaded on the AFM machine for scanning. As we did in Fig.4.2, a force around 80 nN was also applied on the wet sample. In Fig.4.3 A we scanned an area of 5 μm $\times$ 5 μm at a scan angle of 0° and found the surface was quite flat with no clear objects. MFP 3D software showed that the roughness is less than 0.2 nm. However, in Fig.4.3 B one more scan in the same area with the same force and same scan angle created a well-defined corrugated surface that resembled the one on the dry sample (shown in Fig.4.2): collagen bundles with a zigzag shape were aligned with each other, and the overall orientation of the bundles was quite uniform and perpendicular to the fast-scanning direction. The length of such bundles ranges from several hundred nanometers to several micrometers. But compared to the ones in Fig.4.2 B, bundles created by two scans under water are sparser and much bigger in size than those on the dry sample: the bundles are around 1.7 nm in height and 160 nm

123
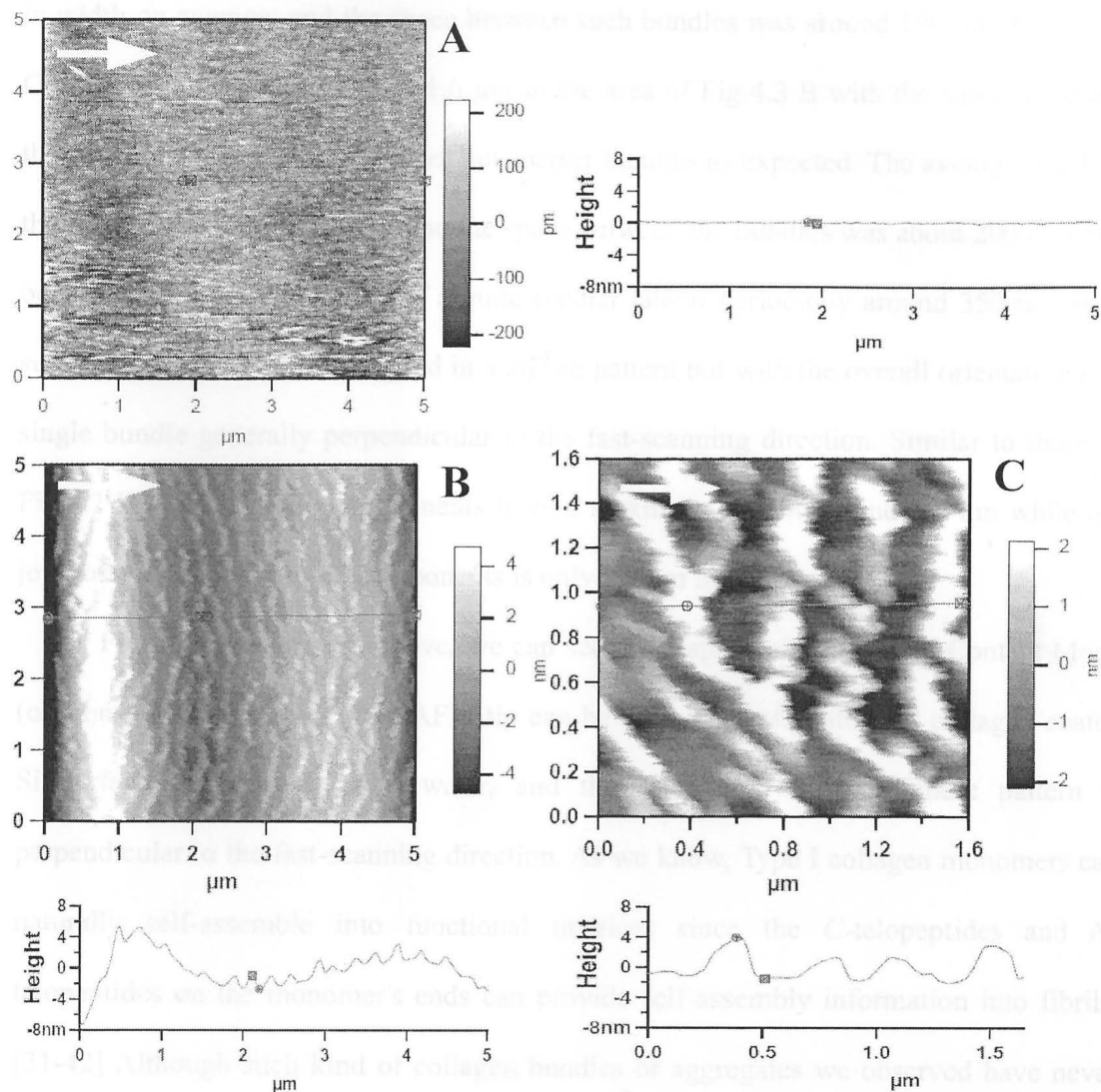
Figure 4.3 AFM topographic images (Contact Mode) of 30 μg/ml collagen coating

on Si wafer under water. A force of around 80 nN was used to create patterns on the

coated surface from A to C. A: a scan area of 5 μm × 5 μm; B : a scan on the same

area of in A; C: a zoom-in scan of B on an area of 1.6 μm × 1.6 μm. The scan angle

0° is indicated by white arrows, and the line-scan height spectrum is shown in the

right for A, but is shown below for B and C.

124

in width on average, and the space between such bundles was around 190 nm. In Fig.4.3 C, a zoom-in scan of 1.6 μm × 1.6 μm in the area of Fig.4.3 B with the same force and the same scan angle created bigger but sparser bundles as expected. The average width of the bundles was about 190 nm and the space between the bundles was about 200 nm. The bundles in Fig.4.3 C are also of a quite regular lateral periodicity around 350 nm, with such periodic components aligned in a zigzag pattern but with the overall orientation of a single bundle generally perpendicular to the fast-scanning direction. Similar to those in Fig.4.2 D, such periodic components have a maximum height around 5.0 nm while the joint between two periodic components is only 2.0 nm high.

From the experiment above, we can see at an appropriate force in Contact Mode (or Constant Force Mode), the AFM tip can be used to create patterned collagen-coated Si surface in air and under water, and the orientation of the bundle pattern is perpendicular to the fast-scanning direction. As we know, Type I collagen monomers can naturally self-assemble into functional matrices since the C-telopeptides and N-telopeptides on the monomer's ends can provide self-assembly information into fibrils. [31-42] Although such kind of collagen bundles or aggregates we observed have never been reported in any literature and do not resemble any collagen fibrils reported so far, how much are those bundles related to the bioactivities of collagen monomers? In 1989, Drake and coworkers used AFM to observe a biochemical process, thrombin-catalyzed polymerization of fibrinogen.[78] A few drops of fibrinogen dissolved into phosphate buffer were placed on a mica surface, and then AFM was used in Contact Mode at a force around 2 nN to image fibrinogen under buffer. However, they could not observe any

125

fibrinogen on mica and they blamed the weak attraction between fibrinogen molecules and the mica surface. But when they added the clotting enzyme, thrombin, to remove a set of peptides from fibrinogen molecules so as to unmask polymerization sites and produce fibrin monomers, a growing zigzag chain that was probably aggregates of fibrin monomers was detected by AFM consequently, and finally fibrin nets were formed on the whole imaging area of 450 nm × 450 nm by such parallel chains. They proposed that although small aggregates of fibrin monomers did move around, while such aggregates connected with each other to form a single chain, such fibrin chains could be imaged reproducibly due to less motion under buffer. But, one can still find in their work, the overall orientation of the zigzag 'chains' were quite uniform and was probably perpendicular to the fast-scanning direction. Moreover, in 1990, Lin and coworkers found that when they investigated a murine antifluorescyl monoclonal immunoglobulin G (4-4-20 IgG₂), a protein of some self-aggregating properties, in phosphate buffer saline (PBS) on mica surface with AFM under a force of 1 nN in Contact Mode, a corrugation surface with a layer of zigzag aggregate 'ridges' was formed gradually on a scan area of 450 nm × 450 nm, and finally a second layer began to deposit.[79] Also, one can find in both layers, the overall orientation of such zigzag 'ridges' was quite uniform and probably perpendicular to the fast-scanning direction.

From the experiments with collagen, fibrinogen and immunoglobulin G, it seems that such corrugation surface of biopolymers coating depends much on the bioactivities of the biopolymer monomers. However, such phenomenon is not that unique as we expected when we looked into more samples with and without bioactivities and might

126

have nothing with any self-aggregating properties of the involved polymers.

Also in 1989, Drake and coworkers found that polyalanine, an amino acid polymer, dissolved in organic solvent (85% chloroform and 15% trifluoroacetic acid) could coat a washed microscope slide and turn out a corrugated surface structure that was imaged by AFM in Contact Mode with a force around 2 nN at a very small scale (3.4 nm × 3.4 nm) on glass dry or covered with water.[78] However, they did not claim any polymer aggregates. It seems that in their work such surface was just coated with a monolayer of polymers and any single polymer chain could be resolved by AFM. But one can still find that the orientation of those zigzag 'chains' was quite uniform and likely perpendicular to the fast-scanning direction. And they did mention that the polymer chains appeared to pack closer together without water.

Although few researchers at that time were interested in the orientation of the aggregates on such corrugation surfaces of proteins, this puzzle was finally solved by Lea and coworkers in 1992.[80] They tried to imitate Drake's AFM work with fibrinogen [78] on mica. During their experiment, they did not add any thrombin to unmask polymerization sites from fibrinogen molecules. Instead, fibrinogen in pH 8.0 PBS was allowed to adsorb onto the mica in the fluid AFM cell for 5 min, then the protein solution was then exchanged for buffer. A force of 30 nN was applied on the AFM tip to scan an area of 2 μm × 2 μm, and beautiful corrugation surface was also formed only on the scan area. To investigate the mechanism behind the corrugation surface, they also imitated Lin's work[79], but with another protein IgM, a mouse monoclonal antifluorescyl antibody (clone 18-2-3), in PBS on mica. This protein is not fibrous, but globular.

However, they also found that very beautiful corrugation surface with zigzag 'strands' was created with appropriate force and the spacing between the strands must increase when the applied force increases. Something more interesting is that: when the AFM tip was scanning at a scan angle of 0°, the overall orientation of the 'strands' was perpendicular to the fast-scanning direction; however, when the AFM tip was scanning at a scan angle of 45°, the overall orientation of the 'strands' was 45° to the fast-scanning direction.

In view of their experimental results, Lea and coworkers proposed the 'molecular broom' mechanism. Fig.4.4 represents the protein manipulation on a surface by a AFM tip in Contact Mode. In Fig.4.4, the AFM tip behaves as a "molecular broom" that sweeps individual proteins or small protein aggregates into larger piles in the fast-scanning direction. The individual proteins and protein aggregates exert a force, which can be broken down into horizontal and vertical components, on the sweeping tip, and the vertical components can definitely cause the cantilever bend. As we know, during the AFM scanning process in Contact Mode, the vertical force on the sample or the vertical bend of the cantilever is always maintained constant at a detectable level by a feedback loop and a vertical (Z-) piezoelectric actuator, which are used to adjust the vertical separation between the AFM tip and the sample by moving the AFM cantilever or the sample (in Lea's experiment, the Z-piezoelectric actuator was controlling the sample, but in our experiments, the Z-piezoelectric actuator was controlling the AFM cantilever). When the protein pile gets too large and its interaction with the surface increases above a critical value, the bend of the cantilever increases to a detectable level and the piezoelectric actuator will retract the sample (the AFM cantilever in our experiments), to

128
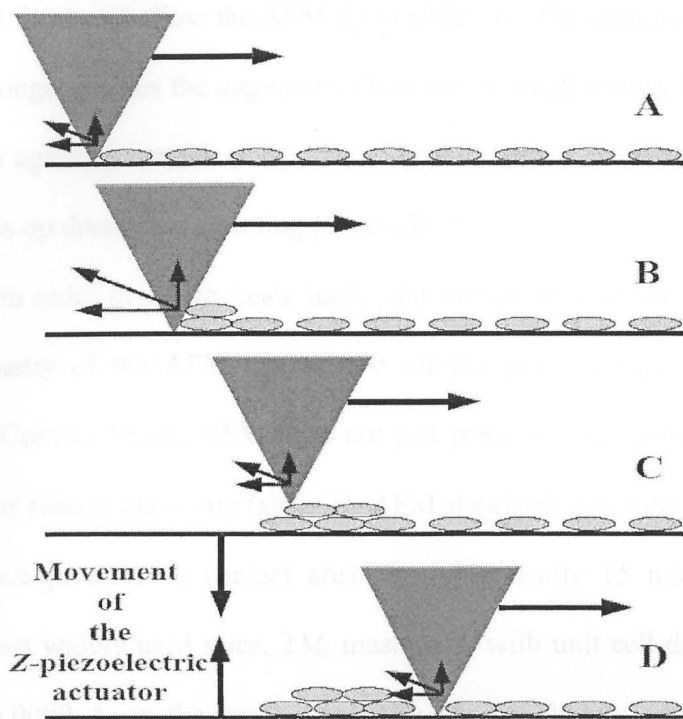
Figure 4.4   Schematic representation of protein manipulation on a surface by a

AFM tip in Contact Mode. A: the AFM tip moving in the fast-scanning direction

indicated by a horizontal arrow begins sweeping the proteins across the surface,

provided the vertical force exerted on the tip by the protein is small. B: while the

proteins begin to pile up, the interaction of the aggregates with the surface

increases, producing a larger vertical force exerted on the cantilever. C: when the

vertical force becomes sufficiently large to cause the cantilever bend, the feedback

system retracts the piezoelectric crystal, as indicated by the downward arrow, to

maintain constant force. D: the piezoelectric crystal advances, as indicated by the

upward arrow, when the vertical force is diminished and the sweeping process

begins again.[80]

129

maintain constant force and allow the AFM tip to slide over the aggregates. At this point, the AFM tip no longer pushes the aggregate. Once past the aggregates, the tip begins the sweeping process again. From this perspective, the AFM tip is working like a broom to pile small proteins up during the scanning process.[80]

However, in order to polish Lea's 'molecular broom' mechanism, we have to take the contact geometry of the AFM tip and the sample into account here first. It was reported that, in Contact Mode, AFM does not just possess single-atom resolution.[87] For a 20 nm radius silicon nitride tip (sharp by AFM standards) exerting a 1 nN load on a clean mica surface produces a contact area involving nearly 15 mica unit cells[87] (assuming the most widely used mica, $2M_1$ muscovite, with unit cell dimensions of $a = 5.2906$ Å, $b = 9.0080$ Å on the basal plane[88]). And including adhesion makes the contact area even larger,[87] which could up to 12 nm² (0.9 nm × 0.9 nm × 15). For a sphere-plane contact geometry, like the contact geometry of the AFM tip and the sample, the contact area A is given by

$$A = K \times (R \times L)^{2/3},$$

where K can be taken as a constant for a simplified calculation, R is the radius of the sphere (the radius of the AFM tip curvature here), and L is the applied load.[87]

In Lea's work, a vapor-deposited silicon nitride tip of radius about 60 nm was used. When they were working with IgM, a 4 nN of force was applied for a 0° scan in Contact Mode on an area around 3.0 μm × 3.0 μm. From the reference contact area (0.9 nm × 0.9 nm × 15 by the tip of a 20 nm radius exerting a 1 nN load) and the equation above, we can simply guess that in Lea's work with IgM, the 60 nm radius tip exerting a 4

130

nN load on sample's surface could create a contact area around 8.0 nm × 8.0 nm. Let's assume that the AFM scanned 256 lines in the slow-scanning direction as a normal AFM image resolution and thus for a 3.0 μm × 3.0 μm scan area, the step size in the slow-scanning direction was around 12 nm (3000/256 nm). So, for such a specific Contact Mode scan, the contact area on two continual scan lines should not have much overlap, which was somewhat reflected in the discontiguous aggregates in Contact Mode images under that force. However, in Lea's work with fibrinogen, a force of 30 nN was applied on a 2.0 μm × 2.0 μm scan area. In this case, from our assumption, the contact area between the tip and the sample was around 15.6 nm × 15.6 nm while the step size in the slow-scanning direction was only about 7.8 nm. So, when they worked with fibrinogen the overlapping of the contact area on two continual scan lines was huge, and they created a really beautiful corrugation surface.[80]

As we discussed before, in Lea's work, they pointed out the exact orientation of the protein aggregates will depend on the orientation of the facets of the cantilever tip relative to the fast-scanning direction. As shown in Fig.4.1 B, one can find that while at a scan angle of 0° or 90°, one facet of the AFM tip (facet I or II) is sweeping proteins or aggregates toward the fast-scanning direction, which probably resulted in the zigzag 'strands' with the overall orientation perpendicular to the fast-scanning direction in Lea's work. However, a really interesting issue about scanning at an angle of 45° is that the turnout orientation of the 'strands' was also 45° to the fast-scanning direction. As shown in Fig.4.1 B, at a scan angle of 45°, two facets of the AFM tip (facets I and II) are sweeping proteins or aggregates in two perpendicular directions (±45° to the fast-

scanning direction). Nevertheless, the results were quite reasonable if we look into the experimental details. In Lea's work with IgM, an 8 nN of force was applied on a 1.7 μm × 1.7 μm scan area when the fast-scanning direction was 45°. Based on our assumption, the contact area between the tip and the sample was around 10 nm × 10 nm. As a matter of fact, this time the AFM was working in Constant Height Mode. They mentioned that protein perturbation would be greater for Constant Height Mode scanning than for Contact Mode scanning because the feedback loop was not so sensitive as in Contact Mode. So, in this case, the random forces exerted by the AFM tip on the sample could be frequently much bigger than 8 nN, which could definitely cause the contact area even bigger. In addition, for a scan size of 1.7 μm × 1.7 μm, the step size in the slow-scanning direction was only about 6.6 nm. Although during the scanning at an angle of 45°, two facets of the AFM tip were sweeping proteins or aggregates in perpendicular directions, the overlap was huge for two continuous line scans along the slow-scanning direction, and proteins in half of the previously scanned area would be corrected to a perpendicular direction during the next line scan. So, the final protein morphology was probably just due to one facet's contribution. Indeed, long 'strands' orientated 45° to the fast-scanning direction in Lea's work were in micrometer length, which was probably demonstrating the huge overlap during the scanning.

Thus, the protein adsorption images obtained by AFM with Contact Mode present a dynamical picture composed from the spatially and temporally distinct interactions between the tip, protein, and surface. So far, Lea and coworkers explained the relationship between overall orientation of the IgM 'strands' on mica and the scan angle

132

very well.

Following their idea, the zigzag shape of the IgM 'strands' is also possible to explain. For example, at a scan angle of $0°$, the AFM tip is pushing proteins or aggregates toward the fast-scanning direction that is arbitrarily defined as the x axis. For just one line scan, the AFM tip lays the first protein pile at a position along the x axis before the Z-piezoelectric actuator retracts the sample (the AFM cantilever in our experiments), to let the tip pass the protein pile and start piling again. After the one line scan is finished, the AFM tip has laid many protein piles on that line and begins to scan the next line. If the contact area between the tip and the sample is small and the scanning step size between the two lines (i.e. along the slow-scanning direction) is big, there will not be any contact area overlapping between the two continual scans. So, for the second line scan, the first protein pile might not be laid by the AFM tip at the same position along the x axis as the first protein pile created during the previous line scan due to the local surface difference such as the protein density and the anisotropic substrate surface, and so do the other protein piles created later. In this case, only discrete small protein aggregates are expected on the two scanned lines. However, if the contact area between the tip and the sample is huge while the scanning step size along the slow-scanning direction is not so big, there could be overlapping between the two continual scans. Under these circumstances, the newly created protein piles in the second line scan will experience some additional frictions where it is touching the existing protein piles on the previous line although the newly created protein piles are reluctant to align themselves with the protein piles on the previous scan line along the x axis due to the local surface difference like the protein

133

coverage density as we discussed above. So, at the scan angle of 0°, the final turnout after many overlapping scans is a corrugated surface comprising many zigzag 'strands' and the overall orientation of such 'strands' is perpendicular to the fast-scanning direction.

In the following years after Lea's work, when scientists were investigating the surface morphology of many different polymers without any bioactivities with AFM, they found the same phenomenon as the IgM 'strands' on mica observed by Lea and coworkers. In 1994, Yano and coworkers used AFM to investigate the morphology of poly (N-methylpyrrole), a conducting polymer, on highly oriented pyrolytic graphite (HOPG) immediately after electropolymerization.[8] They found under a force ranging from 5 nN to 30 nN, the AFM tip could easily pile the polymer up and form a 'lined pattern', and they noticed that when a stronger force was applied, the AFM tip moved more polymers together, and the 'lined pattern' became sparser, but the 'lines' turned out thicker. They claimed the weak adhesion between the polymer and HOPG was advantageous to modify the polymerized surface.

Also in 1994, Goh and coworkers investigated the surface morphology of another polymer, polystyrene, on mica with AFM.[9] They used diluted polystyrene in benzene to deposit a thin film of polymer on mica. As soon as the solvent evaporated, a force around 100 nN was applied on the AFM tip to scan the polymer film on mica. They found in a scan area of 2 μm × 2 μm, the first scan showed a homogeneous and smooth surface with a roughness within 1 nm. However, in the same area, when they kept scanning for 2 min, distinct oriented bundles appeared with a width about 50 nm and the whole area became corrugated. As the tip was allowed to scan for a longer time, they observed that the

134

aggregation process continued and that the bundles grew in size. They also studied polystyrene with different molecular weight and found no obvious changes in the dimensions and patterns of these bundles. They also reported the periodic sequence of such bundles and that the long axis of the bundles was perpendicular to the fast-scanning direction. Although they did not refer to the 'molecular broom' mechanism, they did conclude that the balance between tip-surface molecule forces versus surface molecule-surface molecule forces, and particularly the plastic deformation of surface molecules, are necessary to form such patterned surface. As a matter of fact, what they observed with polystyrene on mica was quite coincident with our AFM experiment with collagen dry samples on Si, and both the aggregation processes and the bundles size were quite similar, although the two species, collagen and polystyrene, are so different in chemical properties.

In the same year, Nick and coworkers found that a spin-coated film of poly (styrene-block-methyl methacrylate) copolymers on mica could also be modified into oriented bundles that were perpendicular to the fast-scanning direction only if the polymer coating procedure omitted the solvent removal steps so that the polymer film stayed in a soft and plastic state.[10] This experiment confirmed that reasonable balance of the forces between the AFM tip and polymers and the forces among polymer molecules, and plastic deformation of polymer molecules are necessary to form such orientated bundles.

In our work presented above, the AFM tip was used to create patterned collagen-coated Si surface both in air and under water. The molecular broom mechanism of the

135

AFM tip could be a perfect explanation to our experimental results. First, in our experiment, the AFM tip of a radius up to 50 nm exerted an 80 nN of force on a 2.5 μm × 2.5 μm scan area of the dry sample and on a 5 μm × 5 μm scan area of the wet sample while the fast-scanning direction was 0°. Based on our assumption, the contact area between the tip and the sample was around 20 nm × 20 nm. And all the AFM images taken in this experiment had a resolution of 256 scan lines along the slow-scanning direction, which makes the step size in the slow-scanning direction only 9.8 nm for the dry sample and 19.5 nm for the wet sample. From our calculation, even for the wet sample on such a large scan area, there was overlapping between the two continual line scans. For the dry sample on the small area, the overlapping between the two continual line scans was really huge. Indeed, at a scan angle of 0°, collagen bundles were formed on both dry and wet samples' surfaces, and overall orientation of the collagen bundles was perpendicular to the fast-scanning direction. Moreover, although such collagen bundles give a overall uniform orientation, every single bundle turns out a zigzag shape that is obviously a tip piling effect. More interestingly, one can find that, with the same scanning procedures, collagen bundles on the wet sample's surface were normally bigger in size but much less compact compared to the surface morphology of the dry sample. As we discussed, in Drake's work with polyalanine washed microscope slide, the polymer 'chains' (could be polymer aggregates) appeared to pack closer together on dry glass compared with water covered.[78] And Nick and coworkers also reported in their experiment solvent had to remain to get orientated bundles created by the AFM tip.[10] As Goh pointed out, the AFM scanning process was actually dominated by the forces

between the AFM tip and sample molecules (proteins or polymers), the forces between sample molecules and substrates' surface, and forces between sample molecules.[9] For the bundle creating experiment, one can find all the materials chosen were polymers or biopolymers like proteins. We might conclude that as long as we choose such soft, plastic materials to coat a substrate, the AFM tip could be used to create similar corrugation surface morphologies despite their different chemical properties. From this perspective, we might ignore the forces between sample molecules as long as the sample molecules are in a soft and plastic state when we are considering the AFM scanning process. So, in order to create a corrugation surface with a polymer or biopolymer coated substrate, reasonable force balance of the interaction between the AFM tip and sample molecules (proteins or polymers) and the interaction between sample molecules and substrates' surface is especially important. In our experiment, with a drop of water covered on the collagen coated Si surface, the friction (or adhesive force) on the interface between collagen molecules and Si surface was probably reduced, and compared to the dry sample, the same force applied on the AFM tip could more easily push collagen molecules away. So, finally, collagen bundles on the wet sample's surface were normally bigger in size but much much sparser compared to the surface morphology of the dry sample. Even for the 'dry' sample (the sample was left in a laminar flow hood at room temperature for one day), there was likely still a fair number of water molecules around the collagen monomers. From all the observations, we might conclude that solvent choice is really important to reduce the friction on the interface between proteins (or polymers) and the substrates, and solvents might also be important to keep proteins (or polymers) in

137

a soft, plastic state.
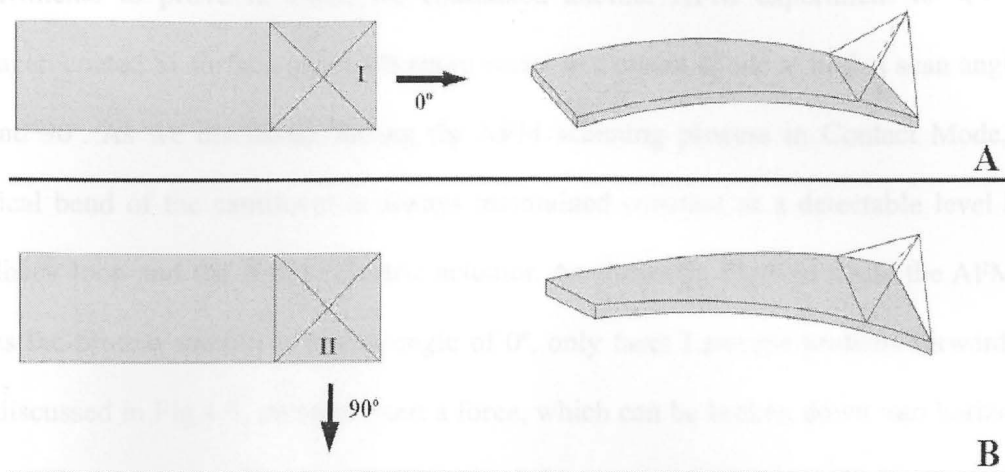
Figure 4.5   Schematic representation of the response of an AFM cantilever to different scan angles in Contact Mode at the same force applied on the tip. When the tip is scanning a sample, the objects the tip is touching exert a force, which can be broken down into horizontal and vertical components on the sweeping tip, and the vertical components can cause the cantilever bend. A: when the tip is scanning a sample at a scan angle $0°$, only facet I sweeps objects along the fast-scanning direction, the vertical force components from the objects on the facet I can only cause the cantilever a vertical bend. B: when the tip is scanning the sample at the same force but at a scan angle $90°$, only facet II sweeps objects along the fast-scanning direction, and the same vertical force components from the objects on the facet II can actually cause the cantilever both a vertical bend and a lateral twist because of the geometrical asymmetry of facet II to the AFM cantilever.

In order to confirm the molecular broom mechanism of the AFM tip, we did more experiments to prove it. First, we conducted another AFM experiment to scan the collagen coated Si surface under ultrapure water in Contact Mode at both a scan angle of $0°$ and $90°$. As we discussed, during the AFM scanning process in Contact Mode, the vertical bend of the cantilever is always maintained constant at a detectable level by a feedback loop and the Z-piezoelectric actuator. As shown in Fig.4.5, while the AFM tip scans the protein sample at a scan angle of $0°$, only facet I sweeps proteins forward. As we discussed in Fig.4.4, proteins exert a force, which can be broken down into horizontal and vertical components, on the facet I of the sweeping tip, and the vertical force components can absolutely cause a vertical bend of the cantilever. However, while the AFM tip scans protein sample at the same force at a scan angle of $90°$, only facet Π sweeps proteins along the fast-scanning direction and the same vertical force components will be exerted on the facet Π of the sweeping tip. However, because of the geometrical asymmetry of facet Π to the AFM cantilever, the vertical force components on the facet Π actually cause both a vertical bend and a lateral twist of the cantilever. However, the feedback loop only responds to the vertical bend of the AFM cantilever. So, from this point of view, the AFM feedback loop is not of the same sensitivity to the force between the AFM tip and sample molecules while the AFM tip is scanning at different fast-scanning directions. When comparing these two fast-scanning directions at the same force, one would expect that protein perturbation would be greater for the scan angle of $90°$ than at a scan angle of $0°$.

In this experiment, a new sample was made as mentioned in the experimental

139

procedures before and was then put into a laminar flow hood at room temperature for one day. The Si wafer surface was covered with 50 μl ultrapure water before scanning with AFM. We scanned an area of 5 μm $\times$ 5 μm first with Contact Mode at a force around 80 nN and a scan angle of 0° twice and Fig.4.6 A shows the final topographic image. Then we aimed the AFM in a new area of 5 μm $\times$ 5 μm and also scanned with Contact Mode at
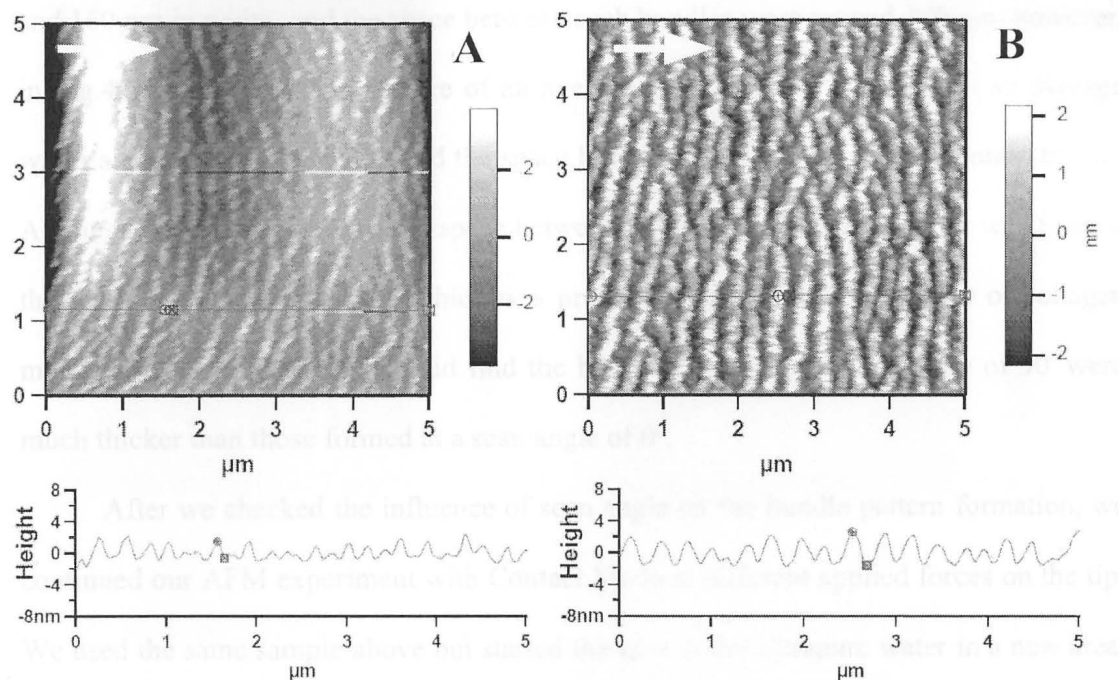
Figure 4.6   AFM topographic images (Contact Mode) of patterned collagen bundles created on Si wafer coated with 30 μg/ml collagen under water. A force of around 80 nN was used to create patterns on the coated surface in two different areas both of 5 μm $\times$ 5 μm. The patterned collagen bundles were created by two continuous scans. A: the bundles were created at a scan angle of 0°; B: the bundles were created at a scan angle of 90°. The fast-scanning directions are indicated by white arrows and the line-scan height spectra are shown below.

140

a force around 80 nN twice but at a scan angle of 90°. Fig.4.6 B shows the AFM topographic image of the second scan. It is not hard to find that in both AFM images, the surfaces turned out a corrugation morphology consisting of collagen bundles, that such bundles were of a zigzag shape with a uniform overall orientation perpendicular to the fast-scanning direction. In Fig.4.6 A, on average, the bundles are around 2.0 nm in height and 160 nm in width, and the space between such bundles were around 180 nm; however, in Fig.4.6 B, collagen bundles are of an average height around 3.0 nm and an average width about 280 nm in width, and the space between such bundles were around 180 nm. Although we did not observe the space between bundles become wider after we changed the scan angle from 0° to 90°, which was probably due to the local density of collagen molecules on the Si wafer, we did find the bundles formed at a scan angle of 90° were much thicker than those formed at a scan angle of 0°.

After we checked the influence of scan angle on the bundle pattern formation, we continued our AFM experiment with Contact Mode at different applied forces on the tip. We used the same sample above but started the scan under ultrapure water in a new area. Our results were shown in Fig.4.7. First, we scanned an area of 5 μm × 5 μm (area I shown in Fig.4.7 A) twice at a force around 80 nN and a scan angle of 0° to create a bundle pattern. Then we focused on a smaller area of 2.5 μm × 2.5 μm within area I (area II shown in Fig.4.7 A) and scanned just once at a force around 800 nN and also a scan angle of 0°. After that, we aimed the AFM on an adjacent new area of 5 μm × 5 μm (area III shown in Fig.4.7 A) at a force around 80 nN but at a scan angle of 90° and scanned twice to create a new bundle pattern. Then, a smaller middle area of 2.5 μm × 2.5 μm in

141

area III (area IV shown in Fig.4.7 A) was scanned just once at a force around 150 nN and a scan angle of 90°. Finally, we scanned a larger area of around 15 μm × 15 μm including all scanned area before, with Contact Mode at only a force around 30 nN and a scan angle of 90° just once to get the whole image. In Fig.4.7 A, one can see, in area I, there are some
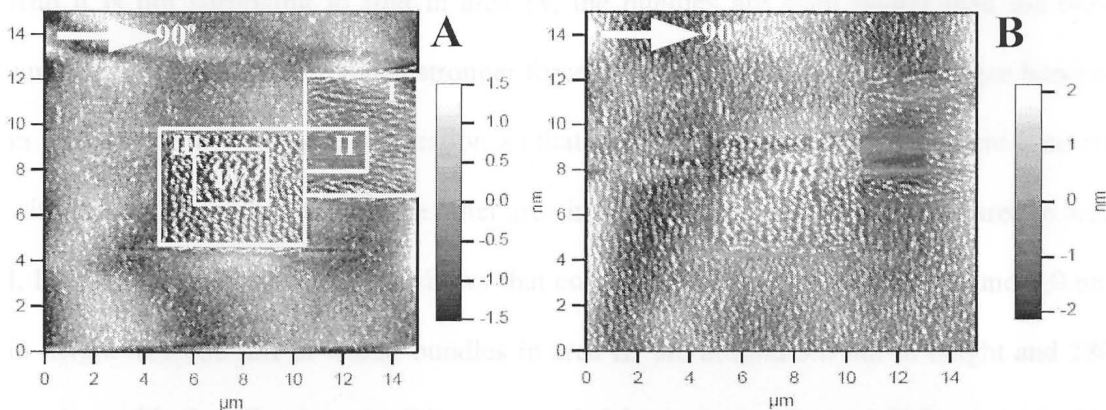
Figure 4.7   AFM topographic images (Contact Mode) of patterned collagen bundles created on Si wafer coated with 30 μg/ml collagen under water. A: a force of around 80 nN was used to scan area I twice at a scan angle of 0° to create patterned collagen bundles. After that, a force of around 800 nN was used to scan area II just once at a scan angle 0°. Then, a force of around 80 nN was applied to scan area III twice at a scan angle of 90° to create patterned collagen bundles in another direction. And then, a force of around 150 nN was used to scan area IV just once at a scan angle of 90°. Finally, the image A was taken at a force around 30 nN and a scan angle of 90° in a large area including area I, II, III, and IV. The same area was scanned for 30 min at the same force and the same scan angle, B was the last image taken. The scan angle 90° is indicated by the white arrows.

142

patterned bundles that are perpendicular to the scan angle 0°. However, in area II, bundles were totally erased and the bare Si surface was exposed. In area III, one can find collagen bundles were perpendicularly aligned with the ones in area I because of a perpendicular scan angle. It seems that collagen bundles in area III are bigger in size than that in area I. And it is not surprising to find in area IV, the bundles are even bigger than the ones surrounding them because much stronger force was applied on that area. collagen bundles in area IV are of the same orientation as that in area III since both areas were scanned with the same scan angle. And the other area in Fig.4.7 A is much flatter compared to area I, II, III, and IV. Image analysis shows that collagen bundles in area I are around 2.0 nm in height and 160 nm in width; bundles in area III are around 3.0 nm in height and 280 nm in width; bundles in area IV are around 6.0 nm in height and 300 nm in width; however, in the other area, the roughness is less than 1 nm. In the following experiment, we kept scanning the larger area of around 15 μm × 15 μm including area I, II, III, and IV, with Contact Mode at the same force around 30 nN and the same scan angle of 90° for 30 min. Fig.4.7 B is the image taken by the last scan. One can find in Fig.4.7 B, area I, II, III, and IV remain with similar morphologies, but in the outer area, patterned collagen bundles were formed finally and the orientation of the bundles are perpendicular to the scan angle 90°. The bundles in the outer area are of an average size about 1.5 nm in height and 270 nm in width; but bundles in area I, II, III, and IV maintain the same size as that in Fig.4.7 A, which might imply that a force around 30 nN is strong enough to create new bundles, but that force is not so strong to reshape the existing bundles.

From the experiment above, we found that with different forces applied by the

AFM tip, we created patterned collagen bundles with different sizes with designed orientation and we could even erase the created bundles with large force. In the following experiment, we tried to switch operation modes between Contact Mode and AC Mode to investigate how much force was required to reshape created bundles. We did that because in AC Mode, the AFM tip can cause little damage to the proteins on the scanned area if the driving amplitude is kept as small as possible. So, compared to Contact Mode images, AC Mode images are better to compare the similarity of the shaped and reshaped corrugated surfaces. A new sample was made as mentioned in the experimental procedures before. The collagen coated Si wafer surface was covered with 50 μl ultrapure water before scanning.

First, an area of 5 μm × 5 μm was scanned twice in Contact Mode at a force around 80 nN with a scan angle of 90° to create the patterned bundles shown in Fig.4.8 A. Such bundles are around 3.0 nm in height and 270 nm in width. Then another image shown in Fig.4.8 B was taken in AC Mode in the same area as soon as the bundles were formed. One can find images in Fig.4.8 A and B are quite similar if we move objects in Fig.4.8 B 1 μm upward, which was probably due to the Si wafer's slight shifting when the AFM was relocating the same imaging area on the Si surface. The size of the bundles in Fig.4.8 B are a little bigger in size: the average height is around 3.5 nm and average width is around 300 nm, which is quite reasonable because in AC Mode, the bundles were measured in a more gentle way. After taking the AC Mode image, we applied a force of 80 nN in Contact Mode again on the same area but at a scan angle of 0° to reshape the existing patterned bundles. As soon as one scan was finished, we took

144
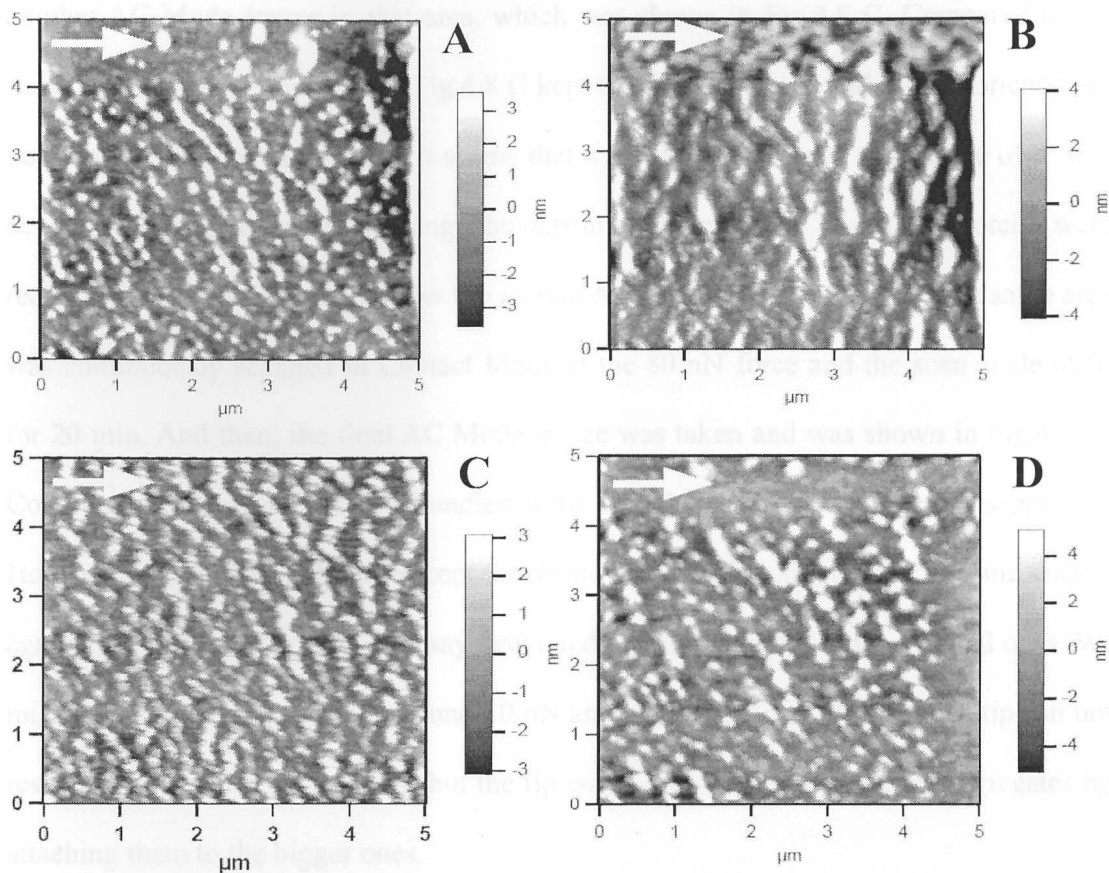
Figure 4.8   AFM topographic images of patterned collagen bundles created on Si wafer coated with 30 μg/ml collagen under water. A: Contact Mode image of the second scan at a force around 80 nN and a scan angle of 90°. B: AC Mode image of the same area of A after the second Contact Mode scan in A. C: AC Mode image after another Contact Mode scan at a force around 80 nN but a scan angle of 0° on the same area following the operation in B. D: AC Mode image after 20 min Contact Mode scan at a force around 80 nN and a scan angle of 0° on the same area following the operation in C. The scan angle 90° is indicated by the white arrows.

another AC Mode image in that area, which was shown in Fig.4.8 C. Compared to the bundles in Fig.4.8 B, bundles in Fig.4.8 C kept the original shape and overall orientation, but they became much slimmer. It seems that a force of 80 nN at a scan angle of 0° was not strong enough to severely change the existing bundles' shape, but some proteins were really picked away by the tip. After the second AC Mode image was taken, the same area was continuously scanned in Contact Mode at the 80 nN force and the scan angle of 0° for 20 min. And then, the final AC Mode image was taken and was shown in Fig.4.8 D. Compared to Fig.4.8 B, some bundles were still there while the others disappeared. However, the remaining bundles kept the shape and orientation, but they became thicker again. So far, we did not observe any new bundles perpendicular to the original ones. We might conclude that at a force around 80 nN and a scan angle of 0°, the AFM tip can not reshape the existing big bundles, but the tip could redistribute the smaller aggregates by attaching them to the bigger ones.

We also tried to enhance the applied force to continue our investigation on the reshaping experiment. We started our experiment with the same sample used above at a new area. This time, a force of 200 nN was always applied in Contact Mode on the AFM tip. Fig.4.9 shows the results of the reshaping experiment. In Fig.4.9 A, on an area of 5 μm × 5 μm, patterned bundles were created in Contact Mode at a force of 200 nN and a scan angle of 90° by scanning the area twice. Fig.4.9 B is the AC Mode image of the newly created bundles on that area. Then the same force of 200 nN was applied on the tip in Contact Mode again on the same area but at a scan angle of 0° to reshape the existing patterned bundles. Fig.4.9 C is the AC Mode image after the first 0° angle Contact Mode

146
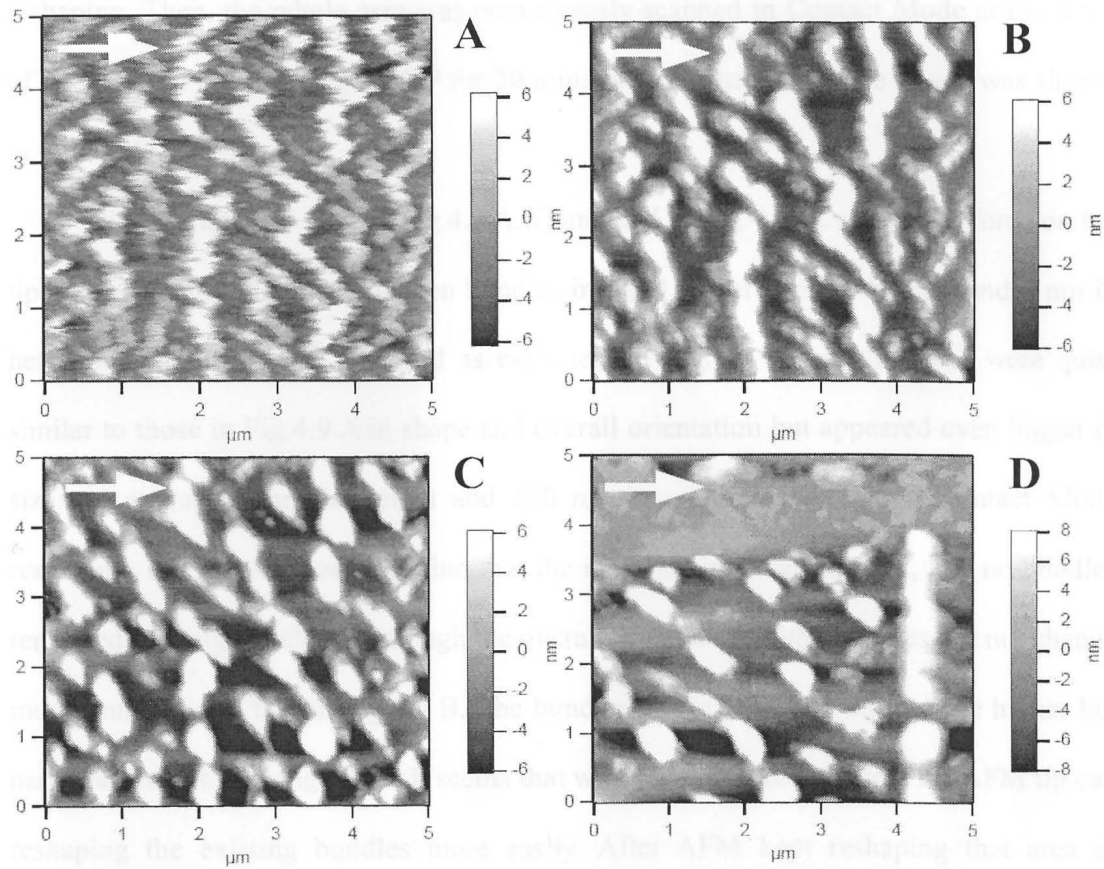
Figure 4.9 AFM topographic images of patterned collagen bundles created on

Si wafer coated with 30 μg/ml collagen under water. A: Contact Mode image

of the second scan at a force around 200 nN and a scan angle 90°. B: AC Mode

image of the same area of A after the second Contact Mode scan in A. C: AC

Mode image after another Contact Mode scan at a force around 200 nN but a

scan angle of 0° in the same area following the operation in B. D: AC Mode

image after 20 min Contact Mode scan at a force around 200 nN and a scan

angle of 0° on the same area following the operation in C. The scan angle 90°

is defined by the white arrows.

147

reshaping. Then, the whole area was continuously scanned in Contact Mode at the force of 200 nN and the scan angle of $0°$ for 20 min, and the final AC Mode image was shown in Fig.4.9 D.

First, let's take a look at Fig.4.9 A. Compared to Fig.4.8 A, a stronger force on the tip created bigger bundles: collagen bundles in Fig.4.9 A are on average around 7 nm in height and 450 nm in width. And as expected, in Fig.4.9 B, such bundles were quite similar to those in Fig.4.9 A in shape and overall orientation but appeared even bigger in size: on average 9 nm in height and 550 nm in width. After one $0°$ Contact Mode reshaping, in Fig.4.9 C, one can find that the morphology changed a lot, and no bundles remained the original shape although the overall orientation of the bundles did not change much compared to that in Fig.4.9 B. The bundles in Fig.4.9 C are on average higher but narrower than that in Fig.4.9 B. It seems that with a larger force applied, the AFM tip can reshaping the existing bundles more easily. After AFM kept reshaping that area in Contact Mode at the force of 200 nN and the scan angle of $0°$ for 20 min, in Fig.4.9 D, one can find that the original created bundles were totally erased, and that the newly created bundles tend to be aligned perpendicularly with the ones in Fig.4.9 A. In view of our results with a larger force applied, we might draw the conclusion that the AFM tip can easily reshape the existing big bundles at a force around 200 nN.

4.4 *Conclusion*

In sum, in our experiments we successfully applied and tested the 'Molecular Broom' mechanism of the AFM tip to create patterned collagen bundles on a collagen

coated Si wafer. In order to create patterned collagen bundles, AFM Contact Mode was applied on both the dry samples and the samples covered with water. But for the samples covered with water, both Contact Mode and AC Mode were switched frequently in the same spot to investigate the pattern formation on that area. Our experimental results demonstrated that in AFM Contact Mode at an appropriate force ranging from 30 nN to 200 nN at a scan angle of 0° or 90°, created bundles are of zigzag shape, but the overall orientation of the bundles was perpendicular to the fast-scanning direction. A stronger force applied on the AFM tip can definitely create bigger bundles in size; while with water covering the coated Si surface, bigger patterned bundles were created at the same force compared to the dry collagen coated surface. Under water, a force no weaker than 200 nN could easily reshape the existing bundles and a force around 800 nN just erased all collagen aggregates on the scanned area. Since our method was based on the precise control of the force on the AFM tip to shape collagen monomers or collagen aggregates on the collagen coated Si surface, we may call this method a 'top down' method for creating collagen coated corrugation surface. Since we can use the AFM tip to precisely manipulate collagen molecules into desired morphologies, we believe this 'top down' method for shaping collagen coated surface is of huge potential application for the cell adhesion studies, for the coating of cell culture flasks and dishes, and for tissue engineering products.

4.5 Bibliography and References

[1]   K. Büscher, R. Berger, W. Brünger, K. Graf, *Microelectr. Engineer.*, 2006, **83**, 819-822.

[2]   T. Mauser, C. Dejugnat, H. Mohwald, G. B. Sukhorukov, *Langmuir*, 2006, **22**, 5888-5893.

[3]   X. Ye, X. Yu, Z. Sun, L. An, *J. Phys. Chem.*, 2006, **110**, 12042-12046.

[4]   P. F. Green, T. M. Christensen, T. P. Russel, R. Jerome, *Macromolecules*, 1989, **22**, 2189-2194.

[5]   T. P. Russel, G. Coulon, V. R. Deline, D. C. Miller, *Macromolecules*, 1989, **22**, 4600-4606.

[6]   K. R. Shull, *Macromolecules*, 1992, **25**, 2122-2133.

[7]   Z. H. Cai, K. Huang, P. A. Monato, T. P. Russel, J. M. Bai, G. W. Zajac, *J. Chem. Phys.*, 1993, **98**, 2376-2386.

[8]   T. Yano, L. A. Nagahara, K. Hashimoto, A. Fujishima, *J. Vac. Sci. Technol. B*, 1994, **12**, 1596-1599.

[9]   O. M. Leung, M. C. Goh, *Science*, 1994, **255**, 64-66.

[10]   L. Nick, A. Kindermann, J. Fuhrmann, *Colloid Poly. Sci.*, 1994, **272**, 367-371.

[11]   V. V. Ginzburg, K. Myers, S. Malowinski, R. Cieslinski, M. Elwell, M. Bernius, *Macromolecules*, 2006, **39**, 3901-3906.

[12]   J. I. Paredes, S. Villar-Rodil, K. Tamargo-Martinez, A. Martinez-Alonso, J. M. D. Tascon, *Langmuir*, 2006, **22**, 4728-4733.

[13]   C. O. Kim, D. H. Kim, J. S. Kim, J. W. Park, *Langmuir*, 2006, **22**, 4131-4135.

[14]   E. Hohenester, J. Engel, *Matrix Biol.*, 2002, **21**, 115-128.

[15]   Y. F. Dufrene, T. G. Marchal, P. G. Rouxhet, *Langmuir*, 1999, **15**, 2871-2878.

[16]   C. M. Kielty, S. P. Whittaker, M. E. Grant, C. A. Shuttleworth, *J. Cell Sci.*, 1992, **103**, 445-451.

[17]   C. Baldock, A. J. Koster, U. Ziese, M. J. Rock, M. J. Sherratt, K. E. Kadler, C. A. Shuttleworth, C. M. Kielty, *J. Cell Biol.*, 2001, **152**, 1045-1056.

[18]   G. Yang, K. A. Woodhouse, C. M. Yip, *J. Am. Chem. Soc.*, 2002, **124**, 10648-10649.

[19]   C. M. Kielty, M. J. Sherratt, C. A. Shuttleworth, *J. Cell Sci.*, 2002, **115**, 2817-2828.

[20]   C. Baldock, M. J. Sherratt, C. A. Shuttleworth, C. M. Kielty, *J. Mol. Biol.*, 2003, **330**, 297-307.

[21]   M. J. Sherratt, D. F. Holmes, C. A. Shuttleworth, C. M. Kieltyy, *Biophys. J.*, 2004, **86,** 3211-3222.

[22]   R. Rounsevell, J. R. Forman, J. Clarke, *Methods*, 2004, **34**, 100-111.

[23]   Ch. C. Dupont-Gillain and P. G. Rouxhet, *Langmuir,* 2001, **17**, 7261-7266.

[24]   F. A. Denis, P. Hanarp, D. S. Sutherland, J. Gold, C. Mustin, P. G. Rouxhet, Y. F. Dufrene, *Langmuir*, 2002, **18**, 819-828.

[25]   V. M. De Cupere, J. F. Gohy, R. Jérome, P. G. Rouxhet, *J. Colloid Interface Sci.*, 2004, **271**, 60-68.

[26]   E. Pamuła, V. De Cupere, Y. F. Dufrêne, P. G. Rouxhet, *J. Colloid Interface Sci.*,

151

2004, **271**, 80-91.

[27]   I. Jacquemart, E. Pamuła, V. M. De Cupere, P. G. Rouxhet, Ch. C. Dupont-Gillain, *J. Colloid Interface Sci.*, 2004, **278**, 63-70.

[28]   C. C. Dupont-Gillain, J. A. Alaerts, J. L. Dewez, P. G. Rouxhet, *Bio-Med. Mater. Engineer.*, 2004, **14**, 281-291.

[29]   Ch. C. Dupont-Gillain, E. Pamuła, F. A. Denis, V. M. De Cupere, Y. F. Dufrêne, P. G. Rouxhet, *J. Mater. sci.: Materials In Medicine*, 2004, **12**, 347-353.

[30]   S. E. Woodcock, W. C. Johnson, Z. Chen, *J. Colloid Interface Sci.*, 2005, **292**, 99-107.

[31]   S. K. Akiyama, K. Nagata, , K. M. Yamada, *Biochim. Biophys. Acta*, 1990, **1031**, 91-110.

[32]   F. Grinnell, *Trends Cell Biol.*, 2003, **13**, 26426-26429.

[33]   F. Jiang, H. Horber, J. Howard, D. J. Muller, *J. Struct. Biol.*, 2004, **148**, 268-278.

[34]   H. A. Goldberg, K. J. Warner, M. C. Li, G. K. Hunter, *Connect Tissue Res.*, 2001, **42**, 25-37.

[35]   R. Fleischmajer, E. D. MacDonald, J. S. Perlish, R. E. Burgeson, L. W. Fisher, *J. Struct. Biol.*, 1990, **105**, 162-169.

[36]   K. Salchert, U. Streller, T. Pompe, N. Herold, M. Grimmer, C. Werner, *Biomacromolecules*, 2004, **5**, 1340-1350.

[37]   P. B. van Wachem, J. A. Plantinga, M. J. B. Wissink, R. Beernink, A. A. Poot, G. H. M. Engbers, T. Beugeling, W. G. van Aken, J. Feijen, M. J. A.van Luyn, *J. Biomed. Mater. Res.*, 2001, **55**, 368-378.

[38]   S. N. Park, H. J. Lee, H. L. Kwang, H. Suh, *Biomaterials*, 2003, **24**, 1631-1641.

[39]   G. A. Di Lullo, S. M. Sweeney, J. Korkko, L. Ala-Kokko, J. D. San Antonio, *J. Biol. Chem.*, 2002, **277**, 4223-4231.

[40]   M. Kuberka, I. Heschel, B. Glasmacher, G. Rau, *Biomed. Technol.*, 2002, **47**, 485-487.

[41]   G. He, A. George, *J. Biol. Chem.*, 2004, **279**, 11649-11656.

[42]   K. E. Kadler, D. F. Holmes, J. A. Trotter, J. A. Chapman, *Biochem. J.*, 1996, **316**, 1-11.

[43]   J. H. Highberger, J. Gross, F. O. Schmitt, *Proc. Natl. Acad. Sci. USA*, 1951, **37**, 286-291.

[44]   J. A. Chapman, M. Tzaphlidou, K. M. Meek, K. E. Kadler, *Electron Microsc. Rev.*, 1990, **3**, 143-182.

[45]   D. J. Prockop, K. I. Kivirikko, *Annu. Rev. Biochem.*, 1995, **64**, 403-433.

[46]   J. K. Rainey, M. C. Goh, *Bioinformatics*, 2004, **20**, 2458-2459.

[47]   J. K. Rainey, M. C. Goh, *Protein Science*, 2002, **11**, 2748-2754.

[48]   K. E. Kadler, *Protein Profile*, 1995, **2**, 491-619.

[49]   M. F. Paige, J. K. Rainey, M. C. Goh, *Biophys. J.*, 1998, **74**, 3211-3216.

[50]   L. I. Fessler, N. P. Morris, J. H. Fessler, *Proc. Natl. Acad. Sci. USA*, 1975, **72**, 4905-4909.

[51]   K. E. Kadler, Y. Hojima, D. J. Prockop, *J. Biol. Chem.*, 1988, **263**, 10517-10523.

[52]   D. E. Birk, R. L. Trelstad, *J. Cell Biol.*, 1986, **103**, 231-240.

[53]   R. Z. Wang, F. Z. Cui, H. B. Lu, H. B. Wen, C. L. Ma, H. D. Li, *J. Mater. Sci.*

Lett., 1995, **14**, 490-492.

[54] J. H. Bradt, M. Mertig, A. Teresiak, W. Pompe, *Chem. Mater.*, 1999, **11**, 2694-2701.

[55] M. J. B. Wissink, R. Beernink, A. A. Poot, G. H. M. Engbers, T. Beugeling, W. G. van Aken, J. Feijen, *J. Controlled Release*, 2000, **64**, 103-114.

[56] D. L. Wilson, R. Martin, S. Hong, M. Cronin-Golomb, C. A. Mirkin, D. L. Kaplan, *Proc. Natl. Acad. Sci. USA*, 2001, **98**, 13660-13664.

[57] C. R. Lowe, *Curr. Opin. Struct. Biol.*, 2000, **10**, 428-434.

[58] J. S. Burmeister, J. D. Vrany, W. M. Reichert, G. A. Truskey, *J. Biomed. Mater. Res.*, 1996, **30**, 13-22.

[59] D. J. Iuliano, S. S. Saavedra, G. A. Truskey, *J. Biomed. Mater. Res.*, 1993, **27**, 1103-1113.

[60] Y. Ito, *Biomaterials*, 1999, **20**, 2333-2342.

[61] U. Geissler, U. Hempel, C. Wolf, D. Scharnweber, H. Worch, K. W. Wenzel, *J. Biomed. Mater. Res.*, 2000, **51**, 752-760.

[62] A. Abbott, *Nature*, 2003, **424**, 870-872.

[63] K. K. Berggren, A. Bard, J. L. Wilbur, J. D. Gillaspy, A. G. Helg, J. J. McClelland, S. L. Rolston, W. D. Phillips, M. Prentiss, G. M. Whitesides, *Science*, 2000, **260**, 1255-1257.

[64] R. D. Piner, J. Zhu, F. Xu, S. Hong, C. A. Mirkin, *Science*, 1999, **283**, 661-663.

[65] S. Hong, C. A. Mirkin, *Science*, 2000, **288**, 1808-1811.

[66] A. D. Stroock, G. M. Whitesides, *Acc. Chem. Res.*, 2003, **36**, 597-604.

154

[67]   R. J. Jackman, J. L. Wilbur, G. M. Whitesides, *Science*, 1995, **269**, 664-666.

[68]   L. Yan, X. M Zhao, G. M. Whitesides, *J. Am. Chem. Soc.*, 1998, **120**, 6179-6180.

[69]   R. S. Kane, S. Takayama, E. Ostuni, D. E. Ingber, G. M. Whitesides, *Biomaterials*, 1999, **20**, 2363-2376.

[70]   F. Sato, H. Okui, U. Akiba, K. Suga, M. Fujihira, *Ultramicroscopy*, 2003, **97**, 303-314.

[71]   G.Y. Liu, X. Song, Y. Qian, *Acc. Chem. Res.*, 2000, **33**, 457-466.

[72]   N. A. Amro, X. Song, G. Y. Liu, *Langmuir*, 2000, **16**, 3006-3009.

[73]   R. E. Marchant, I. Kang, P. S. Sit, Y. Zhou, B. A. Todd, S. J. Eppell, I. Lee, *Current Protein and Peptide Science*, 2002, **3**, 249-274.

[74]   M. E. Greene, C. R. Kinser, D. E. Kramer, L. S. C. Pingree, M. C. Hersam, *Micros. Res. Tech.*, 2004, **64**, 415-434.

[75]   B. D. Sattin, M. C. Goh, *Biophys. J.*, 2004, **87**, 3430-3436.

[76]   D. Czajkowsky, H. Iwamoto, Z. F. Shao, *J. Electron Microsc.*, 2000, **49**, 395-406.

[77]   A. L. Weisenhorn, P. K. Hansma, T. R. Albrecht, C. F. Quate, *Appl. Phys. Lett.*, 1989, **54**, 2651-2653.

[78]   B. Drake, C. B. Prater, A. L. Weisenhorn, S. A. C. Gould, T. R. Albrecht, C. F. Quate, D. S. Cannell, H. G. Hansma, P. K. Hansma, *Science*, 1989, **243**, 1586-1589.

[79]   J. N. Lin, B. Drake, A. S. Lea, P. K. Hansma, J. D. Andrade, *Langmuir*, 1990, **6**, 509-511.

[80]   A. S. Lea, A. Pungor,V. Hlady, J. D. Andrade, J. N. Herron,E. W. Voss Jr, *Langmuir*, 1992, **8**, 68-13.

[81]   M. Rief, M. Gautel, F. Oesterhelt, J. M. Fernandez, H. E. Gaub, *Science*, 1997, **276**, 1109-1112.

[82]   T. E. Fisher, P. E. Marszalek, J. M. Fernandez, *Nature Struct. Biol.*, 2000, **7**, 719-724.

[83]   D. J. Muller, C. A. Schoenenberger, G. Buldt, A. Engel, *Biophys. J.*, 1996, **70**, 1796-1802.

[84]   S. Hong, C. A. Mirkin, *Science*, 2000, **288**, 1808-1811.

[85]   J. D. Gerding, D. M. Willard, A. Van Orden, *J. Am. Chem. Soc.*, 2005, **127**, 1106-1107.

[86]   F. Cattaruzza, A. Cricenti, A. Flamini, M. Girasole, G. Longo, T. Prosperi, G. Andreano , L. Cellai, E. Chirivino, *Nucleic Acids Res.*, 2006, **34**, e32.

[87]   R. W. Carpick, M. Salmeron, *Chem. Rev.*, 1997, **97**, 1163-1194.

[88]   N. Guven, *Zeitschrift fur Kristallographie*, 1971, **134**, 196-212.

Appendix

----- *Light Scattering Methods*

A.1 *Introduction*

Light scattering measurements allow us to detect structures in solution, complementing the surface-bound measurements of AFM. In light scattering experiment a beam of laser light impinges on a sample and is scattered into all directions (see
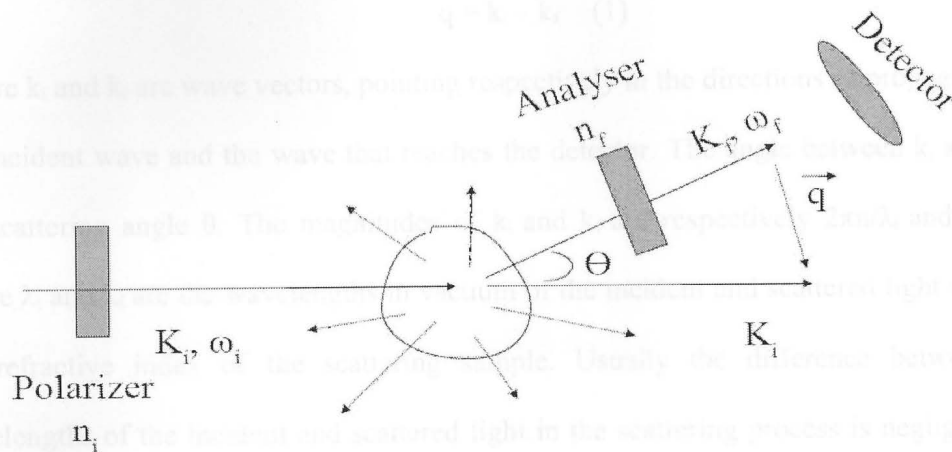
$$|\vec{q}|^2 \approx (K_i - K_f)^2 = 2|K_i|^2 - 2|K_i|^2 \cos\Theta = 4|K_i|^2 \sin^2\frac{\theta}{2}$$

Figure A.1   Light of polarization n_i and wave vector k_i is scattered in all

directions. Only scattered light of wave vector k_f and polarization n_f arrives at the

detector. The scattering vector $q = k_i - k_f$ is defined by the geometry. Since the

scattered wave has essentially the same wavelength as the incident wave, $k_f \approx k_i =$

$(2\pi n/\lambda_i)$, it follows from the law of cosines that $q = 2k_i \sin(\theta/2)$.

157

Fig.A.1). A detector is aligned toward the geometrical center of sample cell and has an angle θ with the laser beam. We can rotate the detector to carry out our scattering experiments at different angles. Or we can move the laser source. In our experiment, we use a stepper motor and a self-written LabVIEW program to control the laser precisely to the right angle and to collect and analyze the scattering data.

We can define scattering vector q (we have to use it later) according to the scattering geometry as shown in Fig.A.1:[1,2]

$$q = k_i - k_f \quad (1)$$

Where k_i and k_f are wave vectors, pointing respectively in the directions of propagation of the incident wave and the wave that reaches the detector. The angle between k_i and k_f is the scattering angle θ. The magnitudes of k_i and k_f are respectively $2\pi n/\lambda_i$ and $2\pi n/\lambda_f$, where λ_i and λ_f are the wavelengths in vacuum of the incident and scattered light and n is the refractive index of the scattering sample. Usually the difference between the wavelengths of the incident and scattered light in the scattering process is negligible. so we can assume:

$$|k_i| \approx |k_f|$$

And, according to cosines law,

$$q^2 = |k_f - k_i|^2 = 4k_i^2\sin^2(\theta/2) \quad \text{or} \quad q = (4\pi n/\lambda_i)\sin(\theta/2) \quad (2)$$

When light impinges on a macromolecule in the solution, light is scattered by its interaction with the electrons of the macromolecule.[3] The oscillating electric field of the light causes a vibration on the electrons and turns them into oscillating dipoles. Then these dipoles reemit radiation. As the electrons in the macromolecule are moving sources

158

of radiation due to their Brownian motion in the solution, the intensity and frequency of

the radiation are shifted lower or higher depending on its velocity and direction relative to

the detector (see Fig.A.2).
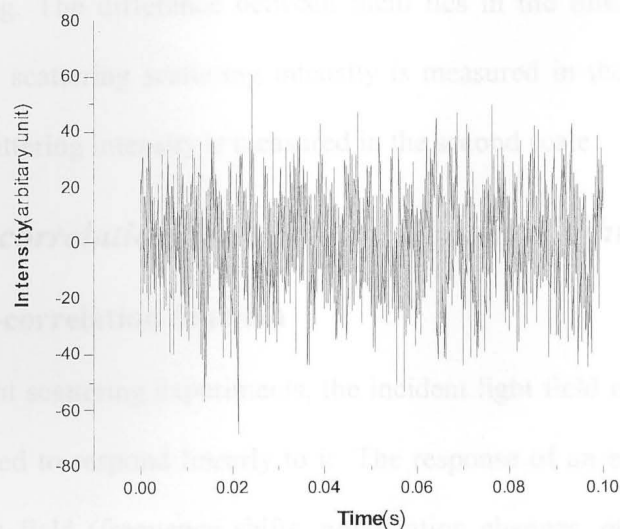
Figure A.2   Light scattering intensity fluctuations from a small detection volume in

a time range of 0.1 s.

For macromolecules or large particles, the polarizability is enormous by

comparison to that of solvent molecules and they move much more slowly than solvent

molecules. So, a macromolecule or large particle will contribute a slowly fluctuating

field, which is separable from the solvent motion. Usually, the Brownian motion induced

scattered light intensity fluctuations of macromolecules or large particles are in the

microsecond time range (in our calibration experiment, we used spherical particles with

diameter range from 100 nm to 2 μm). Moreover, for large molecules or particles,

159

intramolecular interference is huge and the scattered light will probably contain information about molecular shape.

Generally, light scattering can be divided into static light scattering and dynamic light scattering. The difference between them lies in the time range domain. Usually, dynamic light scattering scattering intensity is measured in the microsecond scale; but, static light scattering intensity is measured in the second scale.

A.2 *Time-correlation function and Dynamic light scattering*

A.2.1 Time-correlation function

In light scattering experiments, the incident light field is so weak that the system can be assumed to respond linearly to it. The response of an equilibrium system to this weak incident field (frequency shifts, polarization changes, etc.) due to its interaction with the system can be worked out in terms of time correlation functions of dynamical variables.[4]

Time correlation functions have been familiar for a long time in the theory of noise and stochastic processes.[5] In recent years they have become very useful in many areas of statistical physics and spectroscopy.[6-8] Time correlation functions provide a concise method for describing how a dynamical property is correlated over a period of time.

We can assume that a property A in a system depends on the positions and momenta of all the particles in the system. Because of their thermal motions the particles' positions and momenta are always changing, and so is the property of A. Although the

particles are always moving according to Newton's laws, their very number makes their

motion appear to be somewhat random. The property A(t) will look like a noise signal as

shown in Fig.A.3.
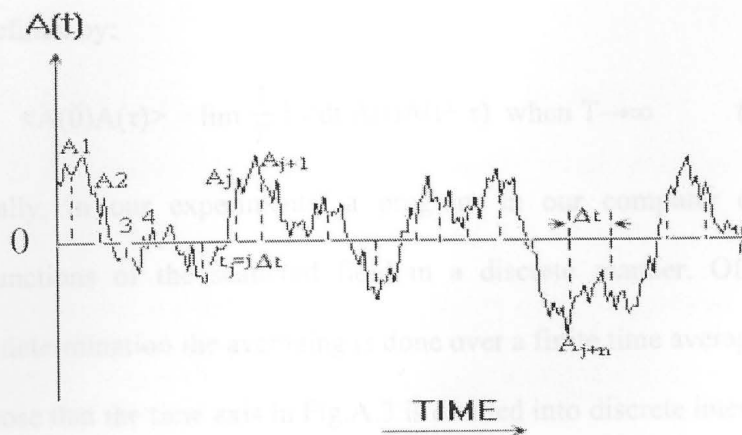
Figure A.3   The property of A(t) fluctuates in time as the molecules move around in

the fluid. The time axis is divided into discrete intervals, Δt, and the time average

$<A>$ is assumed to be zero for convenience.[1]

However, the infinite time average of $<A>$ should be reliable and independent of

the initial measuring time.

$$<A> = \lim \frac{1}{T} \int dt \, A(t) \quad \text{when } T \to \infty \qquad (3)$$

where T is the time over which A(t) is averaged.

The noise signal A(t) in Fig.A.3 displays the following features: the property A

at two times, t and $t + \tau$, can in general have different values so that $A(t+\tau) \neq A(t)$.

Nevertheless when τ is very small compared to times typifying the fluctuations in A, A

$(t+\tau)$ will be very close to A(t). As τ increases the deviation of $A(t+\tau)$ from A(t) is more

obvious. Thus in some sense we can say that value $A(t+\tau)$ is correlated with $A(t)$ when τ is small but that this correlation is lost as τ becomes large compared with the period of fluctuations. A measure of this correlation is the autocorrelation function of the property A, which is defined by:

$$<A(0)A(\tau)> = \lim \frac{1}{T} \int_0^T dt\ A(t)A(t+\tau) \text{ when } T\to\infty \qquad (4)$$

Actually, in our experiments, a program in our computer computes time-correlation functions of the scattered field in a discrete manner. Of course in any experimental determination the averaging is done over a finite time average.

Suppose that the time axis in Fig.A.3 is divided into discrete intervals Δt, and the property A varies very little over the time interval Δt, such that $t = j\ \Delta t$; $\tau = n\Delta t$; $T = N\Delta t$ and $t+\tau=(j+n)\Delta t$. From the definition of the integral Eq.3 and Eq.4 can be approximated by

$$<A> \approx \lim \frac{1}{T} \sum A_j \quad T\to\infty \qquad (5)$$

$$<A(0)A(\tau)> \approx \lim \frac{1}{T} \sum A_j\ A_{j+n} \quad T\to\infty \qquad (6)$$

where A_j is the value of the property at the beginning of jth interval.

Now consider the case $<A(0)A(\tau)>$ varies according to different τ, To Eq.6, if $\tau=0$, $A_j^2 \geq 0$ and all terms in the sum Eq.6 are nonnegative. However, in Fig.A.3 we can see the noise signal $A(t)$ fluctuates to be positive or negative from time to time. If $\tau > 0$, many of the terms in the sum Eq.6 are negative; Consequently, this sum will involve some cancellation between positive and negative terms. So, we can conclude

162

$$\langle A(0)^2 \rangle \geq \langle A(0)A(\tau) \rangle \quad \text{or} \quad \sum A_j^2 \geq A_j A_{j+n} \qquad (7)$$

Thus the autocorrelation function of A would decays from its initial value, which is a maximum, if A is not independent of all times τ, in which case A is a constant of motion.

However, for times τ large compared to the characteristic time typifying the fluctuation of A, A(t) and A(t+τ) are expected to become totally uncorrelated; thus

$$\lim \langle A(0)A(\tau) \rangle = \langle A(0) \rangle \langle A(\tau) \rangle = \langle A \rangle^2 \quad \text{when } T \rightarrow \infty \qquad (8)$$

So we can see the time-correlation function of a nonperiodic property decays from $\langle A^2 \rangle$ to $\langle A \rangle^2$ eventually. And in many applications the autocorrelation function
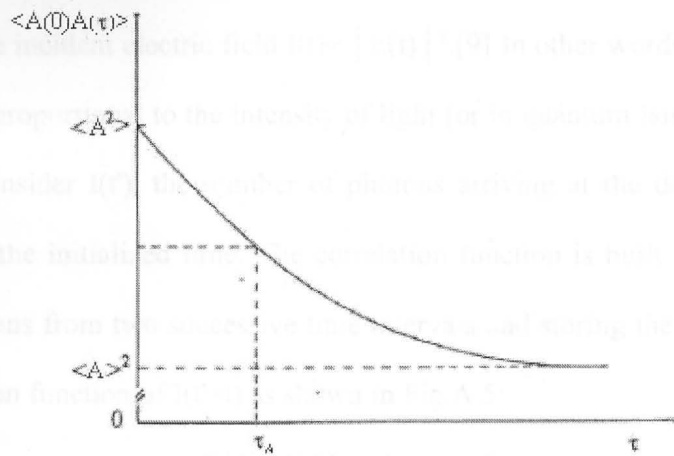

Figure A.4   The time correlation function $\langle A(0)A(\tau) \rangle$. Initially this function is

$\langle A^2 \rangle$. For the time very long compared to the correlation time, τ_A, the correlation

function decays to $\langle A \rangle^2$.

decays like a single exponential as shown in Fig.A.4. We can describe the exponential

163

function:

$$<A(0)A(\tau)> = \{<A^2> - <A>^2\} \exp(-\tau/\tau_A) + <A>^2 \quad (9)$$

So, the autocorrelation function is a measure of the similarity between two signals $A(t)$ and $A(t+\tau)$. When $\tau = 0$, the two signals are completely in phase with each other and $<A(0)A(\tau)>$ is the largest; as τ increases, $A(t)$ and $A(t+\tau)$ get out of phase with each other and the autocorrelation function $<A(0)A(\tau)>$ becomes to decay.

A.2.2 Dynamic Light scattering

In light scattering experiments, the detector usually is a phototube. As we know, a phototube is a squared law detector, its instantaneous current output is proportional to the square of the incident electric field $I(t) \propto |E(t)|^2$.[9] In other words, the square of the electric field is proportional to the intensity of light (or in quantum language, the number of photons). Consider $I(t')$, the number of photons arriving at the detector at the time interval t' from the initialized time. The correlation function is built by multiplying the number of photons from two successive time intervals and storing the result. So, we can get the correlation function of $I(t'+t)$ as shown in Fig.A.5:

$$G(t)=<I(t')I(t'+t)> \quad (10)$$

At the limits mentioned in time-correlation function section,

$$\lim G(t)=<I(t')^2> \quad (t\rightarrow 0)$$
$$\lim G(t)=<I(t)>^2 \quad (t\rightarrow\infty)$$

Finally, we can get the eqution:

$$G(t)=(<I(t)^2> - <I(t)>^2) \, \text{Exp}(-t/\tau) + <I(t)>^2 \quad (11)$$

164
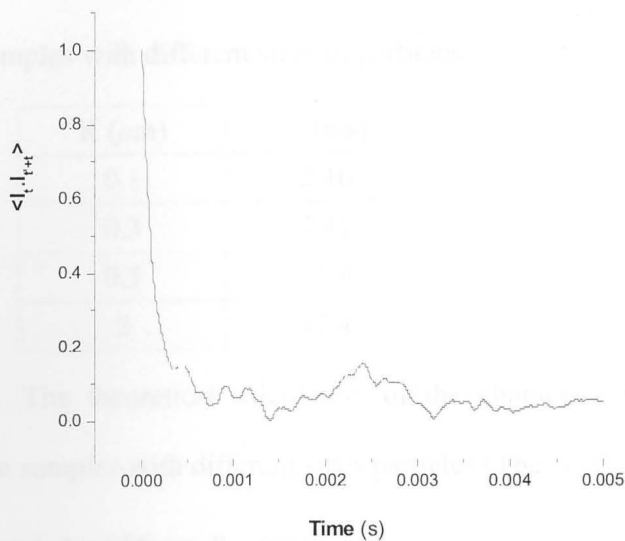
Figure A.5 An autocorrelation function for small monodispersed particles.

The characteristic decay time τ can be used to determine the particle's translational diffusion coefficient, D_T, which in turn is related to the size of the particle. [1,3]

$$\tau = (q^2 D_T)^{-1} \quad (12)$$

As mentioned above, the scattering vector q can be determined by the scattering geometry:

$$q = 4\pi\, n_0 \sin(\theta/2)/\lambda$$

while D_T is related to the hydrodynamic radius (R_h) by the Stokes-Einstein relationship [10,11]:

$$D_T = k_B\, T/(6\pi\eta R_h) \quad (13)$$

where k_B is the Boltzman constant and η is the solvent viscosity.

165

In Table A.1 are listed the data about the characteristic decay time τ of monodisperse samples with different sizes of particles.

R (μm)	τ (ms)
0.1	2.16
0.3	7.11
0.5	11.9
2	47.4

Table A.1   The theoretical calculation of the characteristic decay time τ for monodisperse samples with different sizes particles (The conditions: T = 295 K; η = 0.001 $Pa.s$; n_o =1; λ= 635 nm; θ = 90°).

What we discussed about the dynamic light scattering and time-correlation function is somewhat simplified and more details are omitted. For example, Eq.13 can be be directly used to determined the size of monodisperse samples. For the polydisperse samples, we can only obtain the average size of the particles. However, combining certain mathematical programs, we can carry out multi-exponential fit to obtain the size distribution of the particles for bimodal or multimodal samples. In order to get the shape of the non-sphere particles, we can combine the static light scattering method to detect the geometries of the particles.

A.3 *Static Light Scattering*

For polymers, light scattering intensity integrated over a period of time of seconds or more varies with the measurement angle and concentration[12] according to

$$K.c/R_\theta = 1/(MP_\theta) + 2A_2c \qquad (14)$$

where,

$$K = \{ 4\pi^2 n_0^2 (dn/dc)^2 \}/(N_A \lambda^4) \qquad (15)$$

$$R_0 = d^2/\sin^2\theta_z \, (I_s/I_0) \qquad (16)$$

c represents concentration, I_0 is the intensity of the incident light. I_s is the scattered light intensity; θ_z is the measurement angle relative to vertical axis; d is the sample-detector distance; n_0 is the refractive index of solvent; n is the refractive index of the solution; and dn/dc is the change in refractive index of solution as a function of solute concentration, and can be taken as a constant for specific solute and solvent; A_2 is the second viral coefficient accounting for interparticle interaction; M is the molecular weight, and

$$P_\theta = I_{s,\theta}/I_{s,\theta=0} \qquad (17)$$

is the intra-particle structure factor.

P_θ can be evaluated by[13]

$$P_\theta \approx 1- \{(16 \pi^2 n_0^2 R_g^2)/(3\lambda^2)\} \sin^2(\theta/2) \qquad (18)$$

where R_g is the radius of gyration.

Since the concentration dependence is negligible ($A_2 \approx 0$), by subtitution Eq.18 in, Eq. 15 can be simplified to:

$$1/I_s = A/M_w + \{16A\pi^2 n_0^2 R_g^2 \sin^2(\theta/2)\}/(3M_w\lambda^2) \qquad (19)$$

where A is a constant. Plotting $1/I_s$ against $\sin^2(\theta/2)$, a linear relationship is expected. Dividing the slope by the intercept, R_g can be calculated:

$$\text{Slope/Intercept} = (16\pi^2 n_0^2 R_g^2)/(3\lambda^2) \qquad (20)$$

So we can get the gyration radius of the particle R_g. This argument can be extended to spherical non-polymer particles of radius R_g.

167

Another important parameter we can get from static light scattering is the structure factor P_θ. In order to get gyration radius R_g, we used the approximation Eq.18. However, here we can get our experimental results directly from

$$P_\theta = I_{s,\theta}/I_{s,\theta=0}$$

First, plot $1/I_s$ versus $\sin^2(\theta/2)$ and fit it. Then $I_{s,\theta=0}$ can be obtained by extrapolating to $\theta=0$. So, we can eventually get a series of experimental results of $I_{s,\theta}/I_{s,\theta=0}$ at different angles.

The theoretical expectations for P according to several model geometries are listed below for a sphere(radius R), infinitely thin rod (length, L), and Gaussian coil, respectively:[14,15]

$$Pq(q.R) = \{3/(q.R^3)[\sin(q.R)-q.R.\cos(q.R)]\}^2 \quad (21)$$

$$Pq(q.L) = \{2/(q.L)\}\int_0^{q.L}(\sin\theta_Z/\theta_Z)d\theta_Z -[(2/q.L)\sin(q.L/2)]^2 \quad (22)$$

$$Pq(q.R_g) = \{2/(q.R_g)^4[\exp(-q^2.R_g^2)+(q.R)^2 -1] \quad (23)$$

So we can plot the theoretical P versus q.R (or q.L or $q.R_g$) for different model geometries first (see Fig.A.6). Then the experimental results of P can also be plotted along for comparing. So far, we can tell the particles' geometry from the similarity to the theoretical curves.

168
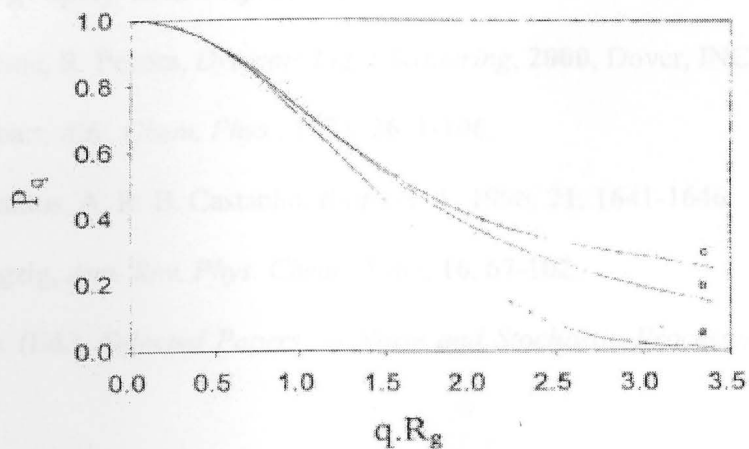
Figure A.6   The theoretical *P*, for different geometries (a, Sphere; b, coil; c, rod).

A.4 *Bibliography and References*

[1]   B. J. Berne, R. Pecora, *Dynamic Light Scattering*, 2000, Dover, INC, NY

[2]   W. Gobush et al, *J. Chem. Phys.* 1972, 26, 1116

[3]   N. C. Ves, A. C. B. Castanho, *J. Chem. Phys.* 1999, 21, 1641-1646

[4]   B. Zengin, *J. Res. Phys. Chem. Phys.*, 16, 67-78

[5]   N. Wax (Ed.), *Selected Papers on Noise and Stochastic Processes*, 1954, Dover, INC, NY,

[6]   A. Sato, *Chem. Eng. J.*, 2004, 69, e067 01-01-04,

[7]   D. H. Sanders et al, *Phys. Rev. E*, 2004, 69, e046121-01-08

[8]   A. M. Howe, R. I. Cook, N. L. Thompson, *Biophys. J.*, 2003, 85, 3299-3307

[9]   H. Z. Cummins, E. R. Pike, (eds.), *photon correlation and light beating spectroscopy*, 1974, Plenum, NY

[10]   A. Einstein, *Investigations on the theory of Brownian movement*, 1956, Dover, NY,

[11]   A. Einstein, *Ann. Phys.*, 1905, 17, 549-560

[12]   B. H. Zimm, *J. Chem. Phys.*, 1948, 16, 1099-1048

[13]   P. Debye, *J. Phys. Colloid Chem.*, 1947, 51, 18-33

[14]   K. S. Schmitz, *An introduction to dynamic light scattering by macromolecules*, 1990, Academic Press, San Diego

[15]   E. F. Casassa, *Particle Scattering Factors in Rayleigh Scattering*, in *Polymer Handbook*, J. Brandup, E. H. Immergut (eds.), John Wiley Sons, NY, 1989, pp. 485-491

A.4 *Bibliography and References*

[1]   B. J. Berne, R. Pecora, *Dynamic Light Scattering*, **2000**, Dover, INC, NY.

[2]   W. Gelbart, *Adv. Chem. Phys.*, 1974, **26**, 1-106.

[3]   N. C. Santos, A. R. B. Castanho, *Biophys. J.*, 1996, **71**, 1641-1646.

[4]   R. Zwagzig, *Ann. Rev. Phys. Chem.*, 1965, **16**, 67-102.

[5]   N. Wax (Ed.), *Selected Papers on Noise and Stochastic Processes*, **1954,** Dover, INC, NY.

[6]   A. Sato, *Phys. Rev. E*, 2004, **69**, e047101-01-04.

[7]   D. B. Saakian, C. K. Hu, *Phys. Rev. E*, 2004, **69**, e046121-01-08.

[8]   A. M. Lieto, R. C. Cush, N. L. Thompson, *Biophys. J.*, 2003, **85**, 3294-3302.

[9]   H. Z. Cummins, E. R. Pike, (eds.), *photon correlation and light beating spectroscopy*, **1974**, Plenum, NY.

[10]   A. Einstein, *Investigations on the theory of brownian movement*, **1956,** Dover, NY.

[11]   A. Einstein, *Ann. Phys.*, 1905, **17**, 549-560.

[12]   B. H. Zimm, *J. Chem. Phys.*, 1948, **16**, 1099-1948.

[13]   P. Debye, *J. Phys. Colloid Chem.*, 1947, **51**, 18-23.

[14]   K. S. Schmitz, *An introduction to dynamic light scattering by macromolecules*, **1990**, Academic Press, San Diego.

[15]   E. F. Casassa, *Particle scattering factors in Rayleigh scattering*, in *Polymer Handbook*, J. Bandup, E. H. Immngut (eds.), John Wiley&Sons, NY, **1989**, pp. 485-491.